Power Generation and Blade Flow Measurements of a Full Scale Wind Turbine

by

Brian Gaunt

A thesis
presented to the University of Waterloo
in fulfillment of the
thesis requirement for the degree of
Master of Applied Science
in
Mechanical Engineering

Waterloo, Ontario, Canada, 2009

I hereby declare that I am the sole author of this thesis. This is a true copy of the thesis, including any required final revisions, as accepted by my examiners.

I understand that my thesis may be made electronically available to the public.

Abstract

Experimental research has been completed using a custom designed and built 4m diameter wind turbine in a university operated wind facility. The primary goals of turbine testing were to determine the power production of the turbine and to apply the particle image velocimetry (PIV) technique to produce flow visualization images and velocity vector maps near the tip of a blade. These tests were completed over a wide range of wind speeds and turbine blade rotational speeds. This testing was also designed to be a preliminary study of the potential for future research using the turbine apparatus and to outline it's limitations. The goals and results of other large scale turbine tests are also briefly discussed with a comparison outlining the unique aspects of the experiment outlined in this thesis.

Power production tests were completed covering a range of mean wind speeds, 6.4 m/s to 11.1 m/s nominal, and rotational rates, 40 rpm to 220 rpm. This testing allowed the total power produced by the blades to be determined as a function of input wind speed, as traditionally found in power curves for commercial turbines. The coefficient of power, C_P, was determined as a function of the tip speed ratio which gave insight into the peak power production of the experimental turbine. It was found, as expected, that the largest power production occurred at the highest input wind speed, 11.1 m/s, and reached a mean value of 3080 W at a rotational rate of 220 rpm. Peak C_P was also found, as a function of the tip speed ratio, to approach 0.4 at the maximum measurable tip speed ratio of 8.

Blade element momentum (BEM) theory was also implemented as an aerodynamic power and force prediction tool for the given turbine apparatus. Comparisons between the predictions and experimental results were made with a focus on the C_P power curve to verify the accuracy of the initial model. Although the initial predictions, based on lift and drag curves found in Abbot and Von Doenhoff [1], were similar to experimental results at high tip speed ratios an extrapolation of the data given by Hoffman et al. [2] was found to more closely match the experimental results over the full range of tip speed ratios.

Finally PIV was used to produce flow visualization images and corresponding velocity maps of the chord-wise air flow over an area at a radius ratio of 0.9, near the tip of a blade. This technique provided insight into the flow over a blade at three different tip speed ratios, 4, 6 and 8, over a range of wind speeds and rotational rates. A discussion of the unique aspects and challenges encountered using the PIV technique is presented including: measuring an unbounded external flow on a rotating object and the turbulence in the free stream affecting the uniform seeding and stability of the flow.

Acknowledgments

Many people have helped me with the content that has gone into this thesis or during the writing phase. From design work to time in the machine shop; troubleshooting experiments to grunt work moving bricks, everyone in the research group had a hand in this project and I appreciate all of their help.

I would first like to thank my supervisor Dr. David Johnson who's guidance throughout my degree has been instrumental in getting me to this point. Whether it was related to my degree or not he was there to provide words of encouragement and excellent advice.

To everybody in the research group you have all helped to make this possible in numerous ways. First to Ammar Altaf and Zeyad Almutairi who made me feel so welcome when I first arrived at the University. Ammar also helped me immensely to learn how to operate the PIV equipment. Stephen Orlando, Erik Skensved and Curtis Knischewsky for putting in a lot of time and effort in the design and construction of various components of the turbine rig and with it's installation. Kobra Gharali for her in-depth knowledge of PIV image processing. Adam Bale, Drew Gertz and Vivian Lam for their additional help through the testing phase of this project. Adam McPhee as someone to bounce ideas off of throughout my degree. Finally to Michael McWilliam for designing the turbine apparatus and tower and putting in many hours in the machine shop to make parts.

To my friends Neil Norris and Andrew Berg for letting me crash on their couch in the final weeks of my experiments (note to others: finish your experiments before giving your landlord 60 days notice).

The support staff and technicians in the department that have helped to make this project come together. I would specifically like to thank Gord Hitchman for his help at the wind facility while running the experiments and Andy Barber and Jim Merli for their electrical support. Also Ed Spike for his help in getting the necessary equipment to run the electrical side of the experiments. John Potzold was also very helpful in teaching me to use the equipment in the machine shop.

Composotech Structures Inc. for completing the turbine blades and for walking me through the manufacturing process on-site and Chris Wraith for his follow-up correspondence.

Most of all, I would like to give a special thanks to my mom who has been very supportive of me throughout my undergraduate and graduate degrees and most recently during the writing of my thesis. Pushing me forward when I needed a bit of a nudge and knowing when I needed to clear my head. I don't know how I would have completed this without your support.

Dedication

I would like to dedicate this thesis to the memory of my dad, David George Gaunt. He was instrumental in guiding me towards a career in engineering and I likely wouldn't be here without his support and encouragement which helped push me to succeed. I know how proud you would be to see this accomplishment.

Contents

List of Tables **xi**

List of Figures **xv**

Nomenclature **xviii**

1 Introduction **1**

1.1 Wind Energy 1

1.2 Goals and Objectives 2

2 Background and Theory **4**

2.1 Previous Large Scale Wind Turbine Tests 4

2.1.1 NREL 4

2.1.2 MEXICO 9

2.2 BEM Theory and Implementation 13

2.2.1 Overview 13

2.2.2 Assumptions 13

2.2.3 Procedure Overview 13

2.2.4 BEM Implementation 14

2.2.5 Force and Power Determination 16

2.3 Particle Image Velocimetry 18

2.3.1 PIV Theory 18

2.3.2 Application of PIV to rotating objects 19

3 Experimental Equipment **21**

3.1 Equipment overview 21

3.2 Wind Facility 21

3.2.1 Wind Velocity Characteristics 23

3.2.2 Fan Frequency to Velocity Correlation 23

3.2.3 Turbulence Intensity 24

3.3 Turbine Assembly 24

3.3.1 Modifications 25

3.4 Turbine Blades 30

3.5 Blade Geometry 31

3.5.1 Chord and Twist Measurements 31

3.5.2 Airfoil Distribution 32

3.6 Airfoil Aerodynamic Properties 34

3.6.1 Lift and Drag Extrapolation 36

3.6.2 Lift and Drag Data sets 37

3.7 PIV Equipment 41

3.7.1 Control 41

3.7.2 Camera 42

3.7.3 Laser 42

3.7.4 Seeding 43

3.8 Power Supply and Loading of the Motor/Generator 44

3.8.1 Overview 44

3.8.2 Motor Power Supply 45

3.8.3 Generator Loading 46

3.8.4 Wiring Box 46

3.9 Instrumentation 48

3.9.1 Data Acquisition Hardware 48

3.9.2 Tunnel Velocity Measurements 48

3.9.3 Rotational Speed 48

3.9.4 Voltage, Current and Power 49

3.9.5 Labview [45] 50

4 Experimental Procedure **52**

4.1 Performance Measurements 52

4.1.1 Drivetrain Loss Estimation 52

4.1.2 Power Production 53

4.2 Experimental PIV Procedure 55

4.2.1 Area of Interest 55

4.2.2 Focus and Alignment 56

4.2.3 Seeding 57

4.2.4 Trigger Timing 57

4.2.5 Interframe Rate 60

4.2.6 Image Correlation 60

4.3 PIV Post-Processing Technique 62

4.3.1 Concept 62

4.3.2 Image Shift Program Verification 65

4.3.3 Experimental Image Processing 65

4.4 Test Case Selection 66

4.4.1 Performance Testing 70

4.4.2 PIV Testing 70

5 Results **71**

5.1 Experimental Performance 71

5.1.1 Outliers 71

5.1.2 Power Losses 72

5.1.3 Power Generation 75

5.1.4 C_P vs TSR 75

5.2 BEM Results 77

5.2.1 Effect of the number of elements 78

5.2.2 Axial Induction Convergence Study 78

5.2.3 Effects of Tip losses 79

5.2.4 Program Output 80

5.2.5 Experimental and BEM C_P Comparison 85

5.2.6 Summary of Experimental Power Production and BEM Modeling 86

5.3 PIV Results . . . 87
5.3.1 Averaged Flow Results . . . 87
5.3.2 Variance in Averaged PIV Results . . . 88
5.3.3 Relative Frame of Reference . . . 93
5.3.4 Repeatability . . . 94
5.3.5 Summary of PIV Results . . . 99

6 Conclusions **101**
6.1 Wind Turbine Power Production . . . 101
6.2 BEM Predictions . . . 101
6.3 PIV . . . 102
6.4 Equipment Improvements . . . 102
6.4.1 Turbine and Blade Assembly . . . 103
6.4.2 Wind Facility . . . 103
6.4.3 Instrumentation . . . 104
6.4.4 PIV Equipment . . . 104
6.5 Recommendations for Future Research Projects . . . 105
6.5.1 Power Production Studies . . . 105
6.5.2 BEM Model Studies . . . 105
6.5.3 PIV Studies . . . 106

References **107**

Appendices **111**

A BEM **111**
A.1 Betz Limit Derivation . . . 111
A.2 BEM Matlab Code . . . 113

B Error Analysis **116**
B.1 Velocity Error . . . 116
B.2 Error in power calculations . . . 117
B.3 Error in coefficient of power calculations . . . 119

C Installation and Decommissioning of the Wind Turbine **121**

D Turbine Blade Fabrication **124**

D.1 Mould and Material Preparation 124

D.2 Process 126

D.3 Fibreglass Lamination Schedule 127

D.4 Skin Layer 129

D.4.1 Second Lamination - triax 129

D.4.2 Third and Fourth Lamination - triax 129

D.4.3 Fifth to Seventh Lamination - UD 130

D.4.4 Texture mat 130

D.5 Spar 132

D.6 Mating Moulds 132

E PIV Smoke Injection Methods **134**

F Post Processing Code **137**

F.1 Image Shift Determination 137

F.2 PIV results Shift 138

F.3 Image Shifting 139

List of Tables

2.1 Turbine and tunnel conditions varied during NREL testing [5] . . . 5

2.2 Turbine and tunnel conditions varied during MEXICO testing [6] . 10

3.1 Turbulence intensity over a range of fan settings 25

3.2 Aerodynamic property data sets used for BEM calculations with original data parameters and the method used for data extrapolation . 35

4.1 Signal Generator settings for PIV 59

4.2 Theoretical and experimental interframe rates 60

4.3 Comparison of manual shift determination and Matlab [17] image shift program 66

4.4 Five test cases used in PIV experimentation 70

5.1 Power loss data based on curve fits on the raw data 74

5.2 Effect of increasing the number of elements 78

5.3 Convergence study 79

B.1 Accuracy error in the Keithley 2700 multimeter [42] 118

List of Figures

1.1 Example of a modern turbine with major components labeled . . . 2

2.1 NREL UAE turbine in the NASA Ames wind tunnel [8] 6
2.2 Sample surface pressure distribution from a point 30% from the blade root on the UAE turbine as presented by Schepers and Rooji [9] . . 7
2.3 MEXICO turbine in the German-Dutch wind tunnel [6] 10
2.4 Sample of the induction measurements based on the MEXICO PIV data [15] 12
2.5 Velocity triangle for a rotating airfoil 14
2.6 Blade force geometry 17
2.7 Schematic of PIV experimental setup and processing [24] 19

3.1 Overall experimental setup: plan view 22
3.2 Fan exit looking from downstream 22
3.3 Sample velocity data at a fan setting of 60 Hz measured using the sonic anemometer, with single sample error shown, mean velocity of 11 m/s 23
3.4 Relationship between fan frequency and streamwise velocity 24
3.5 Turbine assembly CAD model: profile view [28] 26
3.6 Turbine assembly photo: Angled view with load bank, camera and laser system in place 27
3.7 Turbine assembly photo: Profile view of nacelle 27
3.8 Exploded view of mounting plates 28
3.9 Brake system schematic 29
3.10 Brake system photo: Air cylinder and master brake cylinder 29
3.11 Brake system photo: Calipers and disc mounted on the low speed shaft 30
3.12 Measured chord distribution of the manufactured turbine blades . . 31

3.13 Twist distribution of the manufactured turbine blades 32
3.14 Mould casings in place along a finished blade at the root, mid-section and tip 33
3.15 Tip mould casing removed from blade and cut at midpoint 33
3.16 Measured blade coordinates compared with NACA profiles: a) the tip, b) middle and c) root 34
3.17 Coefficient of drag as a function of the coefficient of lift [1] 37
3.18 Lift coefficient as a function of α [1, 2, 34, 35] 39
3.19 Drag coefficient as a function of α [1, 2, 34, 35] 40
3.20 Lift coefficient comparison between raw data and the Viterna extrapolation [34] 40
3.21 Drag coefficient comparison between raw data and the AirfoilPrep extrapolations [34] 41
3.22 Final seeding method smoke generator and condensate collector . . 43
3.23 Final seeding method 44
3.24 Electrical system wiring schematic 45
3.25 Load bank schematic 47
3.26 Sonic anemometer placed in tunnel air flow 49
3.27 Power generation schematic 50
3.28 Motoring schematic 51

4.1 Raw power curve for data collected at U_∞ =3.5 m/s (above) and $U_\infty = 6.4$ m/s, demonstrating high levels of variability at low velocities 54
4.2 Calibration image, with a ruler in the frame, used to focus the camera and determine image scale 56
4.3 Pulse schematic 58
4.4 Signal Generator settings for PIV 59
4.5 Sample correlation surface plot 61
4.6 Master image used to determine the shift vector for each raw image pair 62
4.7 Shift vector concept 63
4.8 Common area found after determining the shift vector for all images within a test case 64
4.9 Shifted image, before (left) and after (right) 64
4.10 Raw images used in PIV analysis with the well seeded image shown above, TSR 3.8, $\Omega = 198$RPM, $U_\infty = 11.8$m/s 67

4.11 Contour plots showing accepted vectors in blue for each of the raw image correlations, TSR 3.8, Ω = 198 RPM, U_∞ = 11.8m/s (well seeded above) 68

4.12 Vector plots from individual image pairs, TSR 3.8, Ω = 198 RPM, U_∞ = 11.8m/s (well seeded above) 69

5.1 Overall power loss data 73

5.2 Difference between power measured with and without the blades attached as a function of the rotational speed 74

5.3 Power generated by the blades 76

5.4 Power at the blades with varying wind speed, Ω= 220 rpm 76

5.5 Raw experimental C_P results 77

5.6 The effect of the number of elements used in the BEM analysis on the C_P 79

5.7 Convergence criteria effect on the C_P 80

5.8 Tip loss factor along the length of the blade 81

5.9 Effect of tip losses on the elemental power produced 81

5.10 Effect of TSR on the AOA over a blade at a wind speed of 11 m/s . 82

5.11 Effect of the input β distribution on the AOA output 83

5.12 Effect of TSR on the axial induction factor, a 84

5.13 Effect of TSR on the tangential induction factor, a' 84

5.14 Effect of the *Flat* or *Viterna* extrapolation on the calculated C_P with the experimental results also shown 85

5.15 Two BEM results compared to experimental C_P results found during testing 86

5.16 Absolute average vector map from unshifted PIV data, TSR 3.8, Ω = 198 RPM, U_∞ = 11.8m/s 88

5.17 Absolute average vector map from shifted PIV data, TSR 3.8, Ω = 198 RPM, U_∞ = 11.8m/s 89

5.18 Variability of the data in the unshifted PIV data set with σ_{vel} represented by contours, TSR 3.8, Ω = 198 RPM, U_∞ = 11.8m/s . . . 90

5.19 Variability of the data in the shifted PIV data set with σ_{vel} represented by contours, TSR 3.8, Ω = 198 RPM, U_∞ = 11.8m/s 91

5.20 Contour plot representing the number of vectors that comprised each averaged vector, TSR 3.8, Ω = 198 RPM, U_∞ = 11.8m/s 92

5.21 Relative reference frame from shifted PIV data, TSR 3.7, Ω = 195 RPM, U_∞ = 11m/s 93

5.22 Contour plot representing AOA with streamlines representing the flow over a blade, TSR 3.8, $\Omega = 198$ RPM, $U_\infty = 11.8$m/s 95

5.23 Contour plot representing AOA with streamlines representing the flow over blade, TSR 3.7, $\Omega = 111$ RPM, $U_\infty = 6.8$m/s 96

5.24 Contour plot representing AOA with streamlines representing the flow over a blade, TSR 7.4, $\Omega = 220$ RPM, $U_\infty = 6.8$m/s 97

5.25 Comparison of two tests under the same conditions on separate days at a nominal TSR of 3.8, $\Omega = 198$ RPM, $U_\infty = 11.8$m/s 98

5.26 Comparison of a common data set with different sample sizes, TSR 3.8, $\Omega = 198$ RPM, $U_\infty = 11.8$ m/s 99

A.1 Rotor model used in the BEM analysis [16] 112

B.1 Free stream velocity with both single measurement and mean error shown for comparison 117

C.1 Raising of the nacelle to the mounting point on top of the tower (Side view) 122

C.2 Raising of the nacelle to the mounting point on top of the tower (Front view) 123

D.1 Two piece mould prior to material lay-up, bottom half is on the right 125

D.2 Lamination schedule drawing with key positions labeled 125

D.3 Gel coat being applied to the lower mould 126

D.4 Areas of the mould which required putty to fill small radius areas . 127

D.5 Bubbles under the skin layer at the edge of the blade mould cavity . 128

D.6 Cutaway view of the blade structure 128

D.7 Skin layer cuts made to avoid wrinkles in bottom half of the mould 129

D.8 Triax trimmed to be 1 cm from the mould edge at the tip 130

D.9 Mould with the fourth lamination applied 131

D.10 UD layer application 131

D.11 Textured mat application 132

E.1 Failed smoke method with smoke generator placed on the conditioning grid 135

E.2 Failed smoke method using a manifold with flow straightening tubes to aid in mixing and smoke stream quality 136

Nomenclature

Roman Symbols

a	Axial induction factor (-)
a'	Tangential induction factor (-)
AR	Aspect ratio of the turbine blade (-)
C	Chord length of the airfoil (m)
C_D	Coefficient of drag (-)
C_{Dflat}	Coefficient of drag based on flat plate theory (-)
C_{Dmax}	Maximum coefficient of drag (-)
C_L	Coefficient of lift (-)
C_P	Coefficient of power (-)
C_T	Coefficient of Thrust (-)
dA	Differential blade area (m^2)
dD	Differential blade drag (N)
dF_N	Differential normal blade force (N)
dF_T	Differential tangential blade force (N)
dL	Differential blade lift force (N)
dP	Differential blade power (W)
dR	Differential blade radius (m)
dT	Differential torque (Nm)
F	Tip loss factor (-)
f_{fan}	Fan frequency (Hz)

G	Gain in shunt resistor (A/V)
I_{arm}	Current at the armature (A)
I	Current (A)
I_S	Shunt current (A)
I_T	Free stream turbulence intensity (-)
N	Number of blades (-)
N_S	Number of Samples (-)
P_{Aero}	Power loss due to aerodynamic drag (W)
P_{Blade}	Power generated by blades (W)
P_{Drive}	Power loss due to the drive train (W)
P_{GEN}	Power in or out of generator (W)
P_{Grid}	Power input at the motor (W)
P_{Load}	Power input at the load bank (W)
R	Resistance (Ω)
r	Radial location along blade (m)
R_T	Tip radius (m)
t_{max}	Maximum theoretical interframe rate (s)
T_{motor}	Torque output by motor (Nm)
t_S	T-value from two tailed Student's t-distribution (-)
U_∞	Freestream velocity (m/s)
$\overline{U_\infty}$	Mean of the streamwise velocity (m/s)
V_{abs}	Absolute velocity (m/s)
V_{arm}	Voltage at the armature (V)
V_S	Shunt Voltage (V)
V	Voltage (V)
V_y	Velocity tangential (y-direction) to the blades rotation (m/s)
W	Relative velocity (m/s)

X Number of interrogation areas in the x-direction (-)

Y Number of interrogation areas in the y-direction (-)

Greek Symbols

α Angle of attack (deg)

α_{ref} Maximum angle of attack within a data set (deg)

β Blade set angle (deg)

ΔG Error in gain value (A/V)

ΔI Error in current measurement (A)

ΔP Error in measured power (W)

ΔV Error in the voltage measurement (V)

λ_T Tip speed ratio (-)

λ_r Local speed ratio (-)

Ω Blade rotational speed (rpm)

ω_{motor} Rotational speed of the motor (rad/s)

ϕ Inflow angle (deg)

Φ Magnetic flux generated by field windings (Wb)

ρ Density (kg/m^3)

σ Chord solidity (-)

σ_S Standard deviation of a data set (-)

σ_U Standard deviation of U velocity vector (m/s)

σ_{U_∞} Standard deviation of the streamwise velocity (m/s)

σ_V Standard deviation of V velocity vector (m/s)

σ_{vel} Standard deviation of PIV velocity vectors (m/s)

"Such experiments are frequently configured like icebergs: Only about 10% of the effort shows as output data; the other 90% which establishes the validity of the 10%, is unseen - relegated to the logbook."

Robert J. Moffat, *Describing the Uncertainties in Experimental Results*

Chapter 1

Introduction

1.1 Wind Energy

With a current social and economic drive to develop alternative energy sources the extraction of power, using wind turbines, from renewable wind resources around the world represents an alternative to current non-renewable power sources. Worldwide, wind turbine power capacity was increased by 26% in 2007 over the capacity in 2006. This increased capacity represented a nameplate power increase of approximately 13 GW [3]. Canadian 2008 energy statistics [4] indicated that Canadian wind turbines produce 1.7 TWh of energy which represents 0.29% of the total Canadian utility energy production. In contrast, Denmark has 1.7 times the installed wind turbine capacity of Canada but the energy these turbines produce accounts for 19.9% of their energy production [3]. Although this comparison does not account for the respective populations of the countries it does represent the level at which wind energy can become a part of a country's energy mix.

Despite the continuing growth of the wind energy industry improvements to the design and operation of turbines are always possible. Experimental studies of wind turbine aerodynamics have the potential to improve the operation and efficiency of turbines and the initial prediction of their output. These improvements can ultimately aid in the adoption of these products and help to increase their part in the world's energy mix.

Modern grid connected wind turbines are predominately three-bladed horizontal-axis machines. While the internal design varies between manufacturers a basic turbine consists of four major parts: the blades, hub, nacelle and tower. The blades are typically made of a fibreglass composite structure and range in length depending on the designed power rating of the turbine. The blades are the component which extracts the energy from the wind and transfers it into rotational motion. The hub is the component which connects the blades to the nacelle and, depending on the design, can incorporate active blade pitch control. The nacelle contains all of the mechanical components which, depending on the design, can include: a gear

box, generator, braking system and yaw control. Finally, the tower is the structure which supports the nacelle, hub and blades and is typically mounted on a reinforced concrete base. A typical modern turbine is shown below in figure 1.1 with the major components labeled and a person standing approximately 50 m from the base for reference.

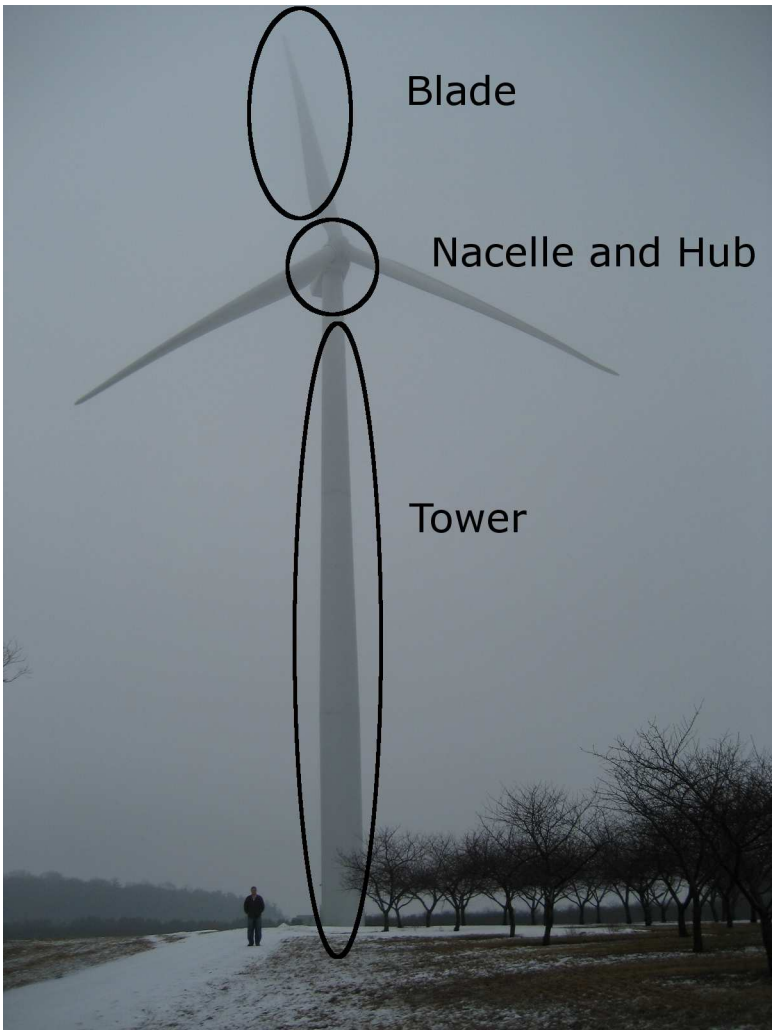

Figure 1.1: Example of a modern turbine with major components labeled

1.2 Goals and Objectives

The goal of this project was to gain a better understanding of the unique characteristics of wind turbine aerodynamics through experimentation. Specifically this experimentation was completed on a rotating large scale 4.3 m diameter wind turbine in a University operated wind facility. This project was broken up into three distinct, but related, areas of study: i) the completion of an experimental study which determined the power generation of a wind turbine over a range of rotational

rates and wind speeds; ii) the development of a numerical, momentum based, model which was used to predict turbine blade loading and power generation; and iii) proof of concept experimental flow measurements around a turbine blade using a laser based velocity measurement technique. For organizational purposes each area of study is presented in separate sections within each relevant chapter. In addition to the major areas of study, a discussion of improvements which can be made to the wind turbine apparatus and wind facility and recommendations for further studies was made.

For the experimental portions of this project a wind turbine apparatus, designed to test various turbine blade configurations, was commissioned for use in a University operated wind facility. The commissioning process involved final assembly of various components of the apparatus as well as it's instrumentation. Ultimately one set of turbine blades was tested on this apparatus and the power they produced at varying wind speeds and rotational rates was quantified. The flow close to the tip of a rotating blade was also visualized and quantified using a laser based technique.

Chapter 2

Background and Theory

This chapter will present a brief background and discuss the theory related to the work completed for this thesis. The first topic includes a discussion of previous large scale wind turbine experimentation which includes an outline of: the experimental equipment used, the results of the testing and the contribution the testing made to further wind turbine research. Secondly, there is a discussion of the momentum based model which was used to predict the output of the wind turbine tested in this experiment. Finally, there is an introduction to the laser based method used to quantify the blade flow near the tip and a discussion of the unique aspects of it's application in this experiment.

2.1 Previous Large Scale Wind Turbine Tests

Due to the scale of commercial wind turbines, with rotor diameters on the order of 100 m, testing of scale models under controlled conditions, like those found in a wind tunnel, has been limited to a very small number of experiments. Two major projects that have been completed will be discussed in this section: the first completed by the National Renewable Energy Laboratory (NREL) in the National Full-Scale Aerodynamics Complex at NASA's Ames research facility [5]; and the second project, MEXICO, was coordinated by the Energy Research Center of the Netherlands (ECN) with tests completed at the large scale low speed wind tunnel (LLF) which is part of the German-Dutch Wind tunnel (DNW) network [6]. While the goals and objectives of these two tests were not identical they represent the foremost large scale wind tunnel testing of wind turbines to date.

2.1.1 NREL

Based on testing by NREL in the NASA Ames wind tunnel the research community was provided with experimental data which covered blade pressure measurements

Table 2.1: Turbine and tunnel conditions varied during NREL testing [5]

Test Variable	Range of Values
Wind Speed	5 to 39.3 m/s
Rotational Rate	0, 72, 90 rpm
Blade Pitch	3 to 79 degrees
Yaw Angle	-180 to 180 degrees
Cone Angle	0, 3.4, 18 degrees

and power production data with which to compare predictive models. The wind facility used and the turbine tested are briefly described below.

Research that has been completed based on the results of this testing are also discussed with a focus on three dimensional flow effects and the improvement of numerical models used to predict turbine power and loading. These two topics were relevant to the research completed for this thesis due to the power prediction that was completed and the effect that the three dimensional effects could have on the PIV measurements.

Overall 30 different tests were completed utilizing different turbine configurations which varied: the wind input speeds, yaw angle, blade tip design, upwind or downwind rotor, three rotational rates, pitch angle, teetering or rigid hub and finally coning of the rotor. A brief summary of the turbine and tunnel conditions used during the NREL testing outlined in table 2.1.

2.1.1.1 Turbine and Tunnel overview

Completed in 2000, testing of the NREL unsteady aerodynamics experiment (UAE) wind turbine, in NASA's 24.4 m by 36.6 m wind tunnel, provided the wind turbine research community with information on the flow and power characteristics of a wind turbine under controlled wind conditions. Prior to this testing information on UAE turbine performance had been gathered in outdoor conditions where wind direction, wind speed and turbulence could not be controlled. The turbine tested was a two bladed constant rotational rate, primarily 72 rpm, stall regulated design with a 10 m rotor diameter and a rated power of 20 kW. The turbine blades used the S809 airfoil along the entire span with the airfoil designed and tested by Somers [7] for NREL. The majority of physical parameters of the turbine and wind tunnel and test conditions relevant to the NREL testing are contained in a report produced by Hand et al. [5]. Figure 2.1 depicts the NREL UAE wind turbine installed in the wind tunnel.

2.1.1.2 Instrumentation

In addition to instrumentation monitoring wind tunnel conditions, such as atmospheric pressure and wind speed, the turbine was instrumented to measure blade

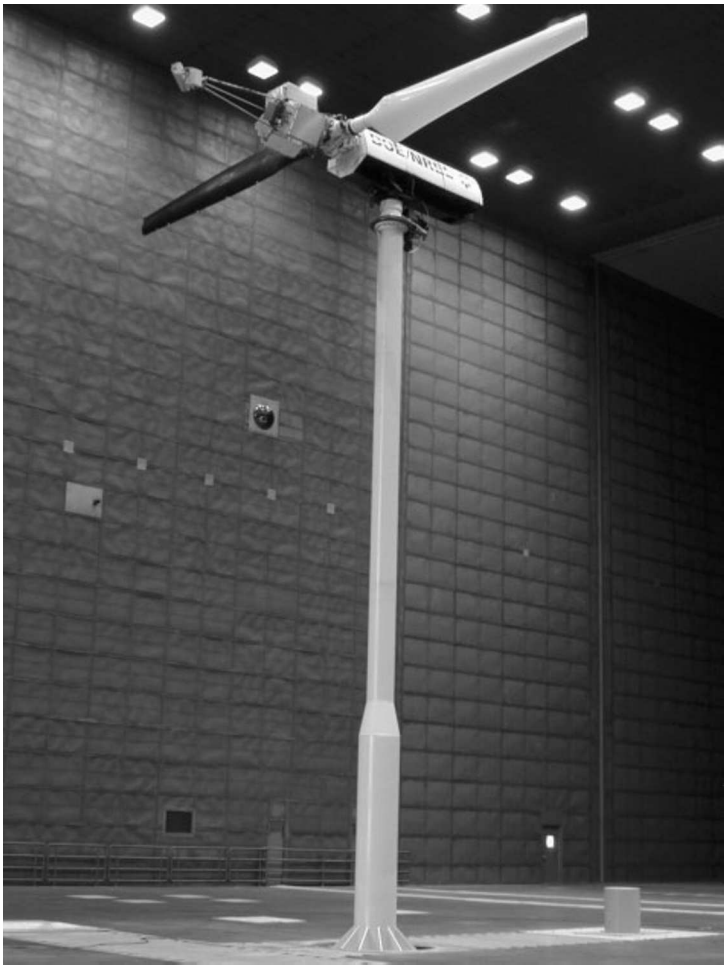

Figure 2.1: NREL UAE turbine in the NASA Ames wind tunnel [8]

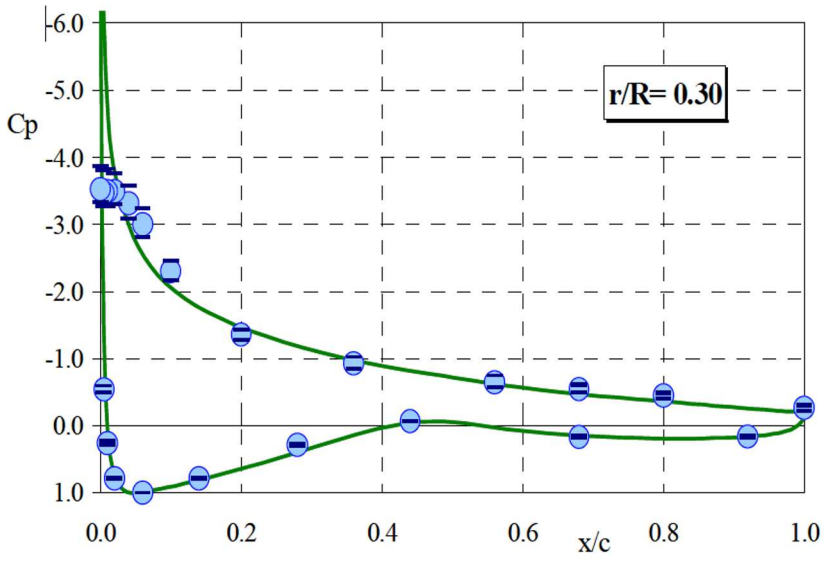

Figure 2.2: Sample surface pressure distribution from a point 30% from the blade root on the UAE turbine as presented by Schepers and Rooji [9]

flow characteristics as well as turbine loading and power production as described by Hand et al. [5]. Specifically a blade was outfitted with surface mounted pressure taps, aligned chord-wise, at five radial locations, along the blade. These surface mounted taps would provide pressure distribution data, and thus loading, along the blade. A sample pressure distribution, shown in figure 2.2 was presented by Schepers and Rooji [9] in a comparison to CFD output and was produced using the surface pressure measurements.

Five hole probes were also mounted to a blade which could measure pressure ahead of the leading edge to provide information on the dynamic pressure and inflow angles at five radial locations. Strain gauges were also mounted to each blade root in order to measure bending moments on the blades. Finally, the tower was mounted to a load balance to measure the forces and moments applied to the entire apparatus. It should be noted that the instrumentation implemented in the NREL testing could not quantify the velocity field around the blades.

2.1.1.3 Three Dimensional Flow and Performance Prediction

A common use of the NREL test results were for the comparison and validation of numerical models which attempted to quantify three dimensional effects on a rotating turbine blade. These comparisons were typically used to gain a better understanding of the complex flow over a wind turbine blade which can ultimately improve power and load prediction for design purposes. Based on past and current work it was found that models still have difficulty consistently predicting power output and blade loading on turbines and as such cannot be the only tool used for design purposes.

One of NREL's goals was to determine the efficacy of models in predicting the power output of the the UAE turbine when the researchers had no prior knowledge of the UAE experimental results. This was called the aerodynamics code blind comparison, discussed by Simms et al. [10], and involved many researchers with 19 models ultimately implemented in an attempt to predict turbine loading and output. Researchers were given the same set of input data such as two dimensional aerodynamic airfoil properties and tunnel conditions at 20 operating points but all experimental output results were unknown to researchers. The goal of this project was to determine not only the prediction uncertainty but also the affect that the assumptions made by the researchers had on the accuracy of their model. Ultimately model predictions resulted in a wide range of results which never consistently matched experimental results. It was also found that some models could predict gross blade loading or power output at some test conditions but the spanwise power or loading distributions did not match experimental results.

After the blind comparison study was complete, Coton et al. [11] attempted, among other goals, to determine the affect of aerodynamic property inputs on the accuracy of model predictions against the NREL UAE data. It was found that the results did vary with different input aerodynamic properties which were the result of two dimensional wind tunnel testing of the same S809 airfoil but under different Reynolds numbers or in different facilities. As only one model was used in their study it was not possible to state with confidence that inconsistent predictions were the results of the model itself or of the input data but it was clear that three dimensional effects needed further study.

Breton et al. [12], using the same model implemented by Coton et al. [11], attempted to determine the effect of various models used to correct two dimensional aerodynamic airfoil data for three dimensional stall delay. It was found for these models that corrections produced a wide range of predicted blade loading. It was suggested that overprediction of lift near the tip was a dominant factor in poor prediction of experimental results as tip forces, due to their increased moment arm, have a larger power production potential.

In an attempt to rule out the effect of aerodynamic properties of the airfoil on the accuracy of a model Laino et al. [13], as part of their study, determined lift and drag properties based on measured inflow angles and forces on the blades during the NREL tests. While this should provide the most accurate aerodynamic properties for the prediction of blade loading the model did not accurately predict the angle of attack that was measured by the probes mounted on a blade. As the angle of attack was not accurately predicted, the accuracy of the blade load prediction was not improved using this method. Further work was done to modify the aerodynamic properties for the model input to match the calculated experimental force coefficients. While this modified property input improved the accuracy of the model in both yawed and unyawed cases it ultimately required knowledge of the experimental data to do so. However, three dimensional stall effects, in the yawed flow comparison, still affected the accuracy of the model which indicates that modeling these events still required improvements independent of the aerodynamic

properties.

In order to quantify three dimensional flow fields present around wind turbine blades Schreck et al. [14] used a numerical model tool to predict boundary layer separation and impingement points and identify areas of the blade which experience radial flow. Surface pressure data from the NREL tests was used to determine the normal force coefficient during rotating and non-rotating cases at various wind speed inputs. This pressure data was also used to determine boundary layer separation and impingement for verification of the numerical model. The resulting numerical study provided the flow field around the blade, concentrating on the suction side in the results. At lower wind speeds much of the blade continued to experience two dimensional chordwise flow with radial flow confined primarily to the root end of the blade. The flow field results determined that increases in wind speed resulted in more of the blade experiencing radial flow. As suggested by the numerical results the experimental force data confirmed that rotational effects increased the normal force on the blades at higher wind speeds where the radial flow was present along the blade. As the paper only used data from one rotational speed it was only possible to determine the rotational flow field effects due to wind speed.

2.1.2 MEXICO

Completed in late 2006, with planning started in 2001, the Model EXperiments In COntrolled conditions (MEXICO) project was a wind turbine test conducted in a large scale European wind tunnel. Few results have been released to date but preliminary data has been presented by Schepers and Snel [6] and by Snel et al. [15]. The goals and objectives for this research concentrated on improving the uncertainty of the design stage estimates of power production and turbine loading by providing well documented and controlled experimental results. As this project was completed after the NREL testing the MEXICO experimental plan was designed to build on the previous work. Using the apparatus, outlined below, approximately 950 different test runs were completed to measure blade pressure distributions and loading by varying: wind speed, rotational rate, blade pitch and yaw angle. Additionally, some tests dynamically changed the pitch or rotational rate to determine the transient effects of these variables on the measured properties [15]. An overview of test conditions used for the MEXICO project can be found in table 2.2. Additionally, PIV tests were completed which gathered 100 image pair data sets in each of approximately 700 test runs. Figure 2.3 depicts the MEXICO wind turbine installed in the wind tunnel.

2.1.2.1 Turbine and Tunnel Overview

Testing on the MEXICO turbine was completed in the large scale low speed wind tunnel (LLF) at the German-Dutch wind tunnel (DNW) in the Netherlands. The tunnel measured 9.5 m by 9.5 m and was capable of wind speeds between 0 to 62 m/s although testing was only completed up to 30 m/s.

Table 2.2: Turbine and tunnel conditions varied during MEXICO testing [6]

Test Variable	Range of Values
Wind Speed	5.5 to 30 m/s
Rotational Rate	0, 324.5, 424.5 rpm
Blade Pitch	-5.3 to 90 degrees
Yaw Angle	-30, 15, 30, 45

Figure 2.3: MEXICO turbine in the German-Dutch wind tunnel [6]

The wind turbine used for the MEXICO project was designed specifically for their experiment and utilized a 4.5 m diameter three bladed rotor which was very similar in scale to the turbine apparatus used in the experimentation for this thesis. Although the rotational rate was not fixed testing was only completed at three states: 424.5 rpm, 324.5 rpm and parked. Additionally, the adjustable pitch blades were milled from aluminum to provide rigidity and repeatability between the blades. The profile of the blades varied along the radius and as such was a blend of three separate airfoils [6].

2.1.2.2 Instrumentation

In order to expand on data gathered during the NREL tests pressure sensors were placed chordwise at five radial locations. In all 148 sensors were used and due to space constraints, within the blades, the sensors were spread amongst all three blades with two blades measuring at two radial locations and the other blade at one radial location, although a small number of sensors were placed in at identical points along each blade to ensure repeatability. Loads and bending moments were calculated at the blades, using strain gauges, and at the base of the tower, using a load balance built into the wind tunnel.

The significant difference from the NREL testing came from the MEXICO projects PIV implementation. A three dimensional two camera PIV system was used to measure flow: around the rotor plane, upstream and downstream of the rotor plane, and near the blade tip to measure vortex structures. The PIV apparatus was able to move 10 m in the streamwise direction and 1.2 m radially along the blade. The area which could be measured by the PIV apparatus measured 337 mm by 394 mm. The laser sheet used for these measurements was projected horizontally, in a plane parallel to the ground, from a point 270 degrees from vertical, in the clockwise direction.

2.1.2.3 Preliminary MEXICO Results

Current data from the MEXICO project is limited to preliminary results released by Snel et al. [15] and by Schepers and Snel [6]. The results presented by Snel et al. concentrate on the PIV results, likely due to the unique nature of these results. Results based on the pressure measurements are also given but are limited, in the Snel et al. paper [15], to blade pressure distributions at various angular positions in yawed flow to demonstrate dynamic stall effects.

The PIV results concentrated on induction, rotor plane velocity, tip vortices, and the wake region but do not provide a great deal of comparison or analysis due to the preliminary nature of the paper. The decrease in the free stream velocity, due to induction, when approaching the rotor plane was presented and found to be measurable using the PIV technique. A sample of the free stream velocity data

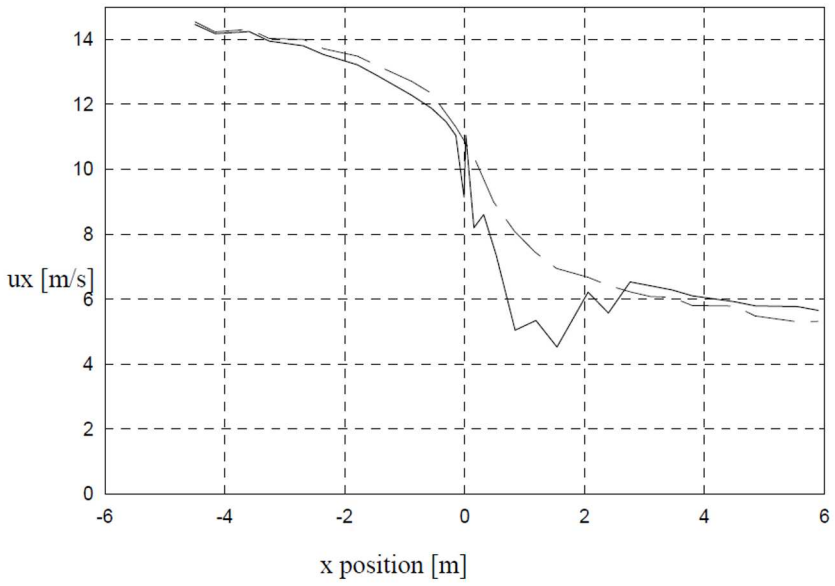

Figure 2.4: Sample of the induction measurements based on the MEXICO PIV data [15]

collected at two radial locations can be found in figure 2.4 which was produced by Snel et al. [15].

The velocity immediately upstream and downstream of the rotor plane was also measured, using PIV, to determine the effect of the blade passing through the free stream flow. It was also found that the PIV technique could be used to capture tip vortex structures and determine the path they travel in the streamwise direction. Circulation calculations on a vortex, from PIV measurements, were also made and compared to pressure distribution based circulation measurements from the blade with reasonable success for one test case.

It should be noted that the current results, presented in Snel et al. [15] and Schepers and Snel [6], do not measure the relative flow immediately surrounding the blades, with the blades in the imaging plane. Measurements of the flow over the blades would have been challenging with the MEXICO PIV apparatus which did not utilize a chord-wise laser sheet. Due to the orientation of the laser sheet the entire blade surface at a given radial location was not illuminated and therefore could not be measured. This presents a unique opportunity to be the first known experiment to measure the relative flow over a rotating wind turbine blade in a large scale wind facility.

In general the MEXICO results, while preliminary, do indicate that the PIV technique can be successfully applied to a wind turbine flow and yield results which can help to understand the unique aspects of wind turbine aerodynamics. With the knowledge that the MEXICO experiment could produce useful PIV data on a scale wind turbine there was motivation to attempt using the PIV technique on the University wind turbine within the Universities wind facility. Additionally,

the opportunity to gather velocity data at a radial location along a wind turbine blade was seen as a unique application of the PIV technique when compared to the MEXICO project.

2.2 BEM Theory and Implementation

2.2.1 Overview

Blade Element Momentum (BEM) theory is a tool used to estimate the aerodynamic forces on a turbine blade and, from this, estimate overall turbine loading and power production. This technique can be employed in order to estimate the forces that blades could exert on a support structure prior to the blades being tested experimentally.

2.2.2 Assumptions

The BEM theory implemented in this analysis utilized a basic model which relied on a few basic assumptions, typical for a basic BEM implementation [16], to simplify the problem to a suitable level for initial turbine analysis. The first assumption was that there is no flow radially along the blade between elements. This assumption implies that adjacent elements have no effect on each other. It also implies that the force on each element is based on the lift and drag from a 2D airfoil under conditions with identical relative velocity and angle of attack. While this assumption ignores the radial flow which is likely present under certain experimental flow conditions, as discussed in section 2.1.1.3, it was necessary in order to simplify the model; however, the error this assumption may introduce should be considered when analyzing the output of the model.

The other main assumption, in this model, was that the incoming wind speed did not vary based on the position of a blade in it's rotation. This effectively assumes that there is no wind shear or yawed flow present. Based on the tunnel design, section 3.2, the wind shear assumption was considered valid due to the speed control of the six fans and thus the wind distribution. The yawed flow condition was directly controlled by orienting the rotor plane to be perpendicular to the incoming wind from the fans which results in zero yaw. Since the yaw results directly from the physical orientation of the wind turbine apparatus in the wind facility and the zero yaw assumption was valid.

2.2.3 Procedure Overview

The BEM procedure first divides the blade into a user specified number of elements which do not aerodynamically interact with each other. The incoming wind speed

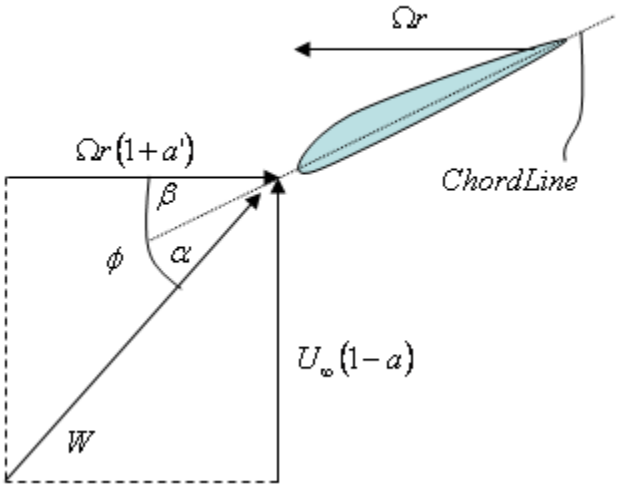

Figure 2.5: Velocity triangle for a rotating airfoil

and relative angle of attack were then determined using an iterative process. Based on the incoming velocity the coefficient of lift and drag were calculated for each element and then, based on the air density and element area, the lift and drag forces were found. These forces were translated into two components: one that was in the rotor plane, tangential, and the other perpendicular to the rotor, normal. This translation was done to calculate the torque and power produced; as the only forces that provide rotational work were those in the tangential direction. The normal forces were absorbed by the rig and were estimated to ensure that the design forces and moments on the tower and base were not exceeded.

2.2.4 BEM Implementation

Each step of the BEM process was completed using Matlab [17] which allowed for the handling of large arrays and simplified the iterative process required to solve the various equations for each element. The Matlab [17] code was designed to allow for flexibility in the inputs such as: the lift and drag characteristics of the blade; the number of blades; tip radius; incoming wind speed; and the number of elements. This was done so that the code was not specific to any one test case or blade design. A sample of the main section of the code can be found in appendix A.

For this procedure values such as: radius; density; airfoil lift and drag data; and chord and twist distribution were all kept constant. Figure 2.5 shows the velocity triangle used in the analysis and the relevant angles used in the equations outlined below. β, α, and ϕ represent the blade set angle, relative angle of attack and the relative inflow angle respectively.

The first step was to find the local speed ratio, λ_r, found using equation 2.1,

with the tip speed ratio and as a function of the radius ratio of a given element.

$$\lambda_r = \lambda_T \frac{r}{R_T} \tag{2.1}$$

$$\lambda_T = \frac{\omega R_T}{U_\infty} \tag{2.2}$$

The next part of the code determined initial values for all parameters in each blade element using an optimum rotor as outlined by Burton et al. [16]. These values were used as a first guess and then iterated using the procedure outlined below to find the actual values. The optimum axial induction factor, a, was found by maximizing the coefficient of power which is derived in appendix A.1. This analysis resulted in the axial induction factor initially set to 1/3 which theoretically results in the maximum coefficient of power of 59.3% which is called the Betz limit [16]. The induction factor, as shown in figure 2.5, effectively represents a reduction of the incoming wind speed due to the presence of a blade.

Due to rotation in the wake of the rotor plane a tangential induction factor, a', was used which effectively adds to the incoming tangential velocity due to the rotation of the blades. Equation 2.3, given by Burton et al. [16], can be used to calculate a' as an initial value for an optimal rotor; however, for simplicity the initial value was set to zero.

$$a' = \frac{a\,(1-a)}{\lambda_r^2} \tag{2.3}$$

The inflow angle, ϕ, was then found, using equation 2.4 which is based on the velocity triangle geometry. Finally the relative angle of attack for each blade section can be calculated, shown in equation 2.5, using the blade set angle and inflow angle; with the blade set angle known by measuring the actual blade geometry. Since these values depend on the velocity triangle geometry the derived equations are not dependent on an optimum rotor assumption, as such they are applicable at all levels of this analysis.

$$\phi = \tan^{-1}\left[\frac{1-a}{\lambda_r\,(1+a')}\right] \tag{2.4}$$

$$\alpha = \phi - \beta \tag{2.5}$$

With the initial values set, the following equations were placed in an iterative loop until convergence, based on the induction factor value, was reached. The convergence criteria was selected as a change of less than 0.01% in the axial induction factor based on a convergence study using the axial induction factor, with results in section 5.2.2. Although the chord and blade set angle distributions were set by the blade geometry the inflow angle could still change based on induction

factor values and the introduction of the tip loss factor. The tip loss factor is introduced to attempt to mimic the losses that exist at the tip of the blade. Equations 2.6 through 2.10, below, were calculated for each blade element, with the code shown in appendix A, and the relevant values were placed in an array in order to be used in force and power calculations. The equations outlined in this section were summarized by Martinez et al. [18] which is based on work by Glauert [19] and Prandtl, given by Shen et al. [20]. The tip loss factor approaches zero at the tip, as outlined in section 5.2.3, which can cause error in the code. This error can be avoided by setting the tip loss factor at the tip to the calculated value from the previous element.

$$a = \frac{1}{1 + \frac{4*F*\sin^2(\phi)}{\sigma[C_L\cos(\phi)+C_D\sin(\phi)]}} \tag{2.6}$$

$$a' = \frac{1}{\frac{4*F*\sin(\phi)\cos(\phi)}{\sigma[C_L\sin(\phi)-C_D\cos(\phi)]} - 1} \tag{2.7}$$

$$F = \frac{2}{\pi}\cos^{-1}\left[exp\left(-1*f\right)\right] \tag{2.8}$$

$$f = \frac{N}{2}\left(1 - \frac{r}{R_T}\right)\sqrt{1+\lambda_T^2} \tag{2.9}$$

$$\sigma = \frac{NC}{2\pi r} \tag{2.10}$$

2.2.5 Force and Power Determination

In order to determine the power produced by the rotor and the resulting power coefficient, C_P, found using equation 2.11, various assumptions must be made. The first is that the lift and drag, generated at the halfway point between element stations, acts across the whole width of the element. This assumption becomes increasingly valid as the area of the discrete element is reduced. Lastly, the inner portion of each blade was assumed to be effectively non-aerodynamic and thus does not detract or contribute to the overall power of the rotor.

$$C_P = \frac{P_{Blade}}{\frac{1}{2}\pi\rho U_\infty^3 R_T^2} \tag{2.11}$$

The first step to calculate the power produced was to find the relative velocity over the blade which was then used to find lift and drag forces, represented by the lift and drag coefficients, C_L and C_D defined by equations 2.13 and 2.14, on each blade element. The forces were then translated into the tangential and normal directions, geometry shown in figure 2.6, with the tangential force used to calculate torque and

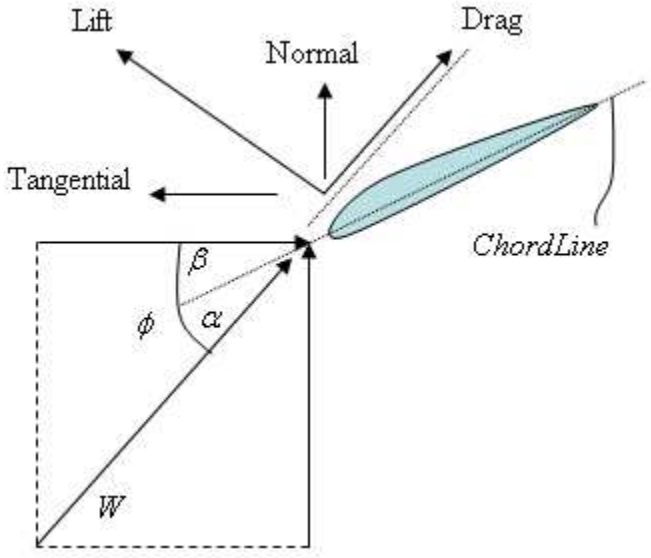

Figure 2.6: Blade force geometry

power. These values were then integrated along the whole blade and multiplied by the number of blades on the turbine to find the total power produced. These calculations are found in equations 2.15 through 2.21 which were, where relevant, based on the blade and velocity triangle geometry.

$$dA = CdR \tag{2.12}$$

$$C_L = \frac{Lift}{\frac{1}{2}\rho U_\infty^2 dA} \tag{2.13}$$

$$C_D = \frac{Drag}{\frac{1}{2}\rho U_\infty^2 dA} \tag{2.14}$$

$$W = \frac{U_\infty (1-a)}{\sin(\phi)} \tag{2.15}$$

$$dL = \frac{1}{2} C_L \rho W^2 dA \tag{2.16}$$

$$dD = \frac{1}{2} C_D \rho W^2 dA \tag{2.17}$$

$$dF_T = dL \sin(\phi) - dD \cos(\phi) \tag{2.18}$$

$$dF_N = dL \cos(\phi) + dD \sin(\phi) \tag{2.19}$$

$$dT = r \times dF_T \tag{2.20}$$

$$dP = \frac{\lambda_T U_\infty}{R_T} \times dT \tag{2.21}$$

The final step taken in the process was to complete the entire BEM procedure for a range of tip speed ratios. This allows the ideal rotational speed for a given wind speed to be found which maximizes C_P and thus the power output of the turbine.

2.3 Particle Image Velocimetry

In this section basic particle image velocimetry (PIV) theory is outlined to acquaint the reader with the technique utilized in this experiment with additional information on the technique found in the FlowMap user's guide produced by Dantec Dynamics Inc. [21]. PIV is typically used in bounded flow conditions, provided by wind tunnel walls or the object being tested, and with the object being tested typically in a stationary position; however, in this experiment PIV was used to visualize and quantify the flow over a rotating turbine blade which was inherently unbounded, external and three-dimensional flow. This experiment represents a unique application of the PIV technique and as such a focus on PIV techniques for measuring the flow on a rotating object is also presented below.

2.3.1 PIV Theory

Particle image velocimetry (PIV) was developed to measure the velocity field of a fluid flow without directly probing the flow with instrumentation. A basic PIV experimental setup requires a high intensity two dimensional light sheet, a camera and seeding particles in the flow. The technique captures two images, or frames, of the flow in short succession and divides each image into a user specified number of "interrogation areas". Through numerical cross-correlation, between the two captured frames, a representative particle displacement in each interrogation area is estimated. If the particles are assumed to travel in a linear motion, the particle displacement divided by the time that elapsed between the captured images will determine the most probable velocity for each interrogation area. As the motion of the particles within the flow is being estimated, as opposed to the flow itself, this technique also assumes that the particle motion matches that of the flow. Ideally through careful selection of seeding particles and the method used to introduce the particles into the flow, as outlined by Melling [22], the error introduced by this effect can be mitigated. Finally, when the velocity vectors for all interrogation areas are calculated an instantaneous velocity vector map is produced.

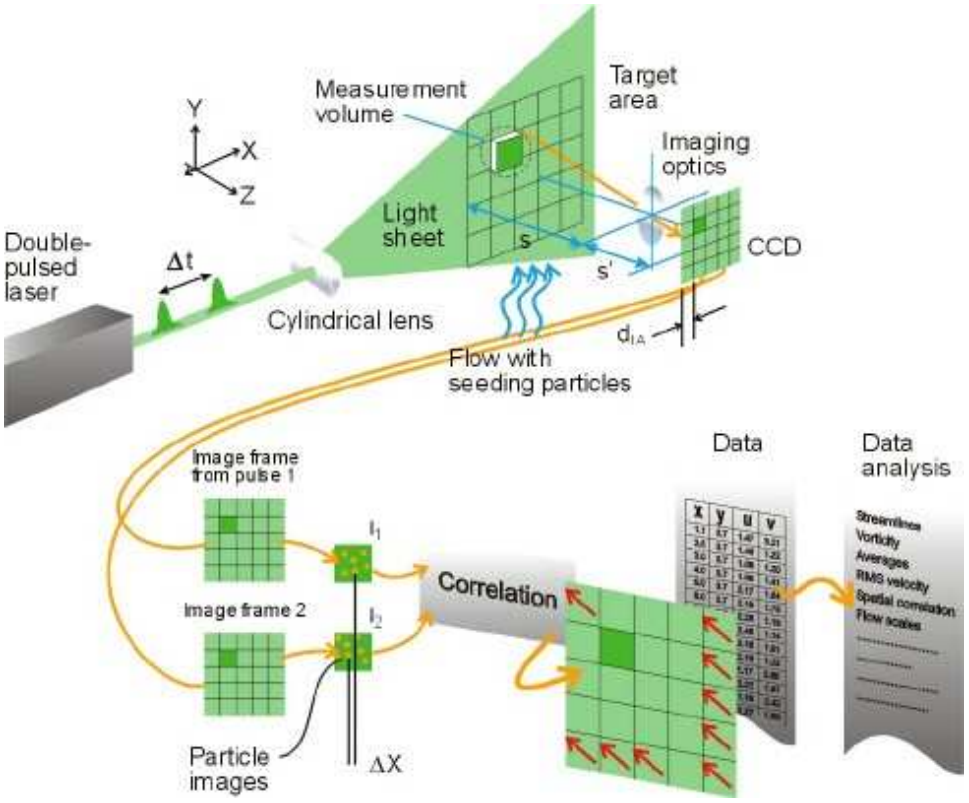

Figure 2.7: Schematic of PIV experimental setup and processing [24]

In order to limit the displacement of particles between frames and to mitigate the effects of acceleration, the time between frames, or interframe rate, is kept short, for this experiment under 100 μs. Additionally, to prevent blurring of the particles the exposure time of each frame is short, on the order of 3 to 5 ns [23]. Both of these limitations require a camera capable of capturing two images in short succession and a high intensity laser sheet to provide an adequate level of light to properly expose the frames. A schematic of the basic PIV concept is shown in figure 2.7 [24] with the laser light sheet parallel to the flow direction and the imaging sensor perpendicular to the flow. Also shown in this image are the interrogation areas which divide the image.

2.3.2 Application of PIV to rotating objects

The basic PIV technique outlined above assumes that the flow will be two dimensional and thus the particles will remain within the projected light sheet. Bounding the flow in a small cross-section closed loop wind tunnel typically aids in the even distribution of seeding particles which should yield more accurate results. An extension of this bounded flow can exist for rotating objects as found in the MASc thesis by Altaf [25] which studied impeller flow with seeded water as the working fluid or Sante et al. [26] which studied rotating channels with a smoke injected air-

flow. Both of these studies bound the flow within rotating channels which helps to contain the seeding particles for an even distribution. Bounded flow also provides an increased knowledge of the expected flow which can help predict flow patterns and validation of the results. Typically in rotating flows a triggering mechanism is used to allow images to be captured at specific points in the objects rotation.

Unbounded external flow measurements using PIV presents unique seeding and validation issues. Unlike bounded flow the seeding particles are not constrained or forced to travel within the imaging area. This can produce PIV images which have limited seeding particles with which to produce velocity data. Validation of the results is also challenging as the flow is not confined to a set path since the flow around the blades is inherently complex as previously discussed in section 2.1.1.3. Two experiments involving rotating objects with external flow using PIV will be discussed: the first on a rotating airfoil within a small wind facility and the second on a large scale rotating wind turbine blade.

Work by Ferreira et al. [27] on a vertical axis wind turbine (VAWT) model in a small scale wind tunnel produced PIV results on a rotating airfoil. This work was able to yield flow measurements at various azimuth angles and estimates of parameters such as vorticity. This paper also discusses the uncertainty present when phase averaging the flow which is a technique also used in this experiment to build an average velocity map from numerous PIV data sets. While their results concentrated on vorticity, it was found, as expected, that phase averaging can remove or reduce the apparent effect of small flow structures that are present in complex time dependent flows. This effect will also be present in the experimentation completed for this project and should therefore be considered when analyzing the significance of any PIV results from a complex flow.

As previously discussed, the MEXICO project [6, 15] was able to produce PIV results on a rotating wind turbine which had a similar scale to the turbine used in this experiment. Although only preliminary results have been released it was found that it was possible to quantify values such as induction from PIV results as well as identifying tip vortex structures using a three dimensional PIV apparatus. While this turbine and the wind tunnel used for the MEXICO project were more advanced than available for this experiment it served as a basis for the types of research that can be performed using the PIV technique on a wind turbine blade.

With no previous research concentrating on the chordwise flow over a large scale rotating blade there was a unique opportunity to contribute a unique data set to the research community.

Chapter 3

Experimental Equipment

3.1 Equipment overview

The experimental setup within the wind facility was comprised of numerous components that are discussed in detail within this chapter. The six areas of interest were: the wind facility, turbine assembly, turbine blades, PIV equipment, instrumentation and electrical components. For reference an overall schematic of the outlined equipment can be found in figure 3.1, with the solid model of the nacelle and tower produced by McWilliam [28]. Each of these areas of interest are outlined in proceeding sections within this chapter.

3.2 Wind Facility

The wind facility which was used in all experiments is an open-looped tunnel with six identical fans driving the flow [29]. The six fans were capable of being operated independently with variable frequency drives. This capability allowed for wind shear to be introduced into the flow; however, this was not utilized in any of the testing completed for this experiment. The fan exit plane is rectangular with a 8.0 m width and 5.9 m height with a photo of the fan exit area shown in figure 3.2. Within the control room adjacent to the test area a fan control panel allowed for the precise control of the fan speeds through a variable frequency drive connected to each fan motor.

This facility was capable of producing nominal wind speeds between 0 and 11 m/s but with relatively large turbulence intensities ranging from 10% to 15%. As this facility was open to the atmosphere environmental conditions could also affect the wind speed as found by an increase in the mean wind speed during some of the PIV testing. A discussion of the characterization of this facility for this testing is found below in section 3.2.1.

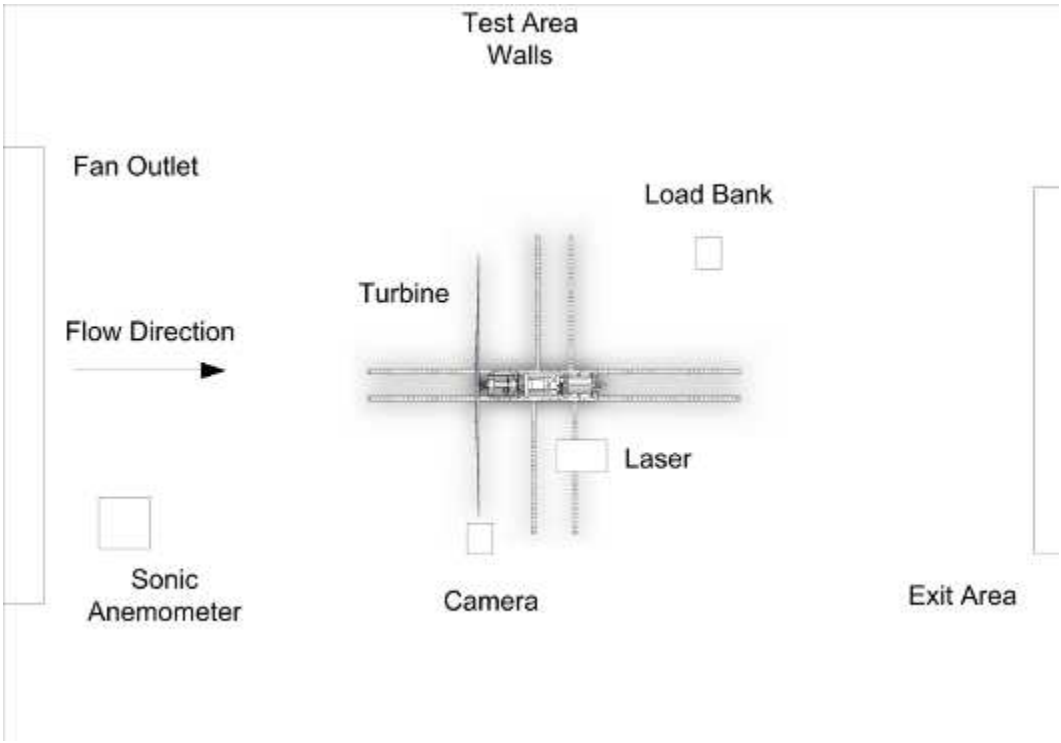

Figure 3.1: Overall experimental setup: plan view

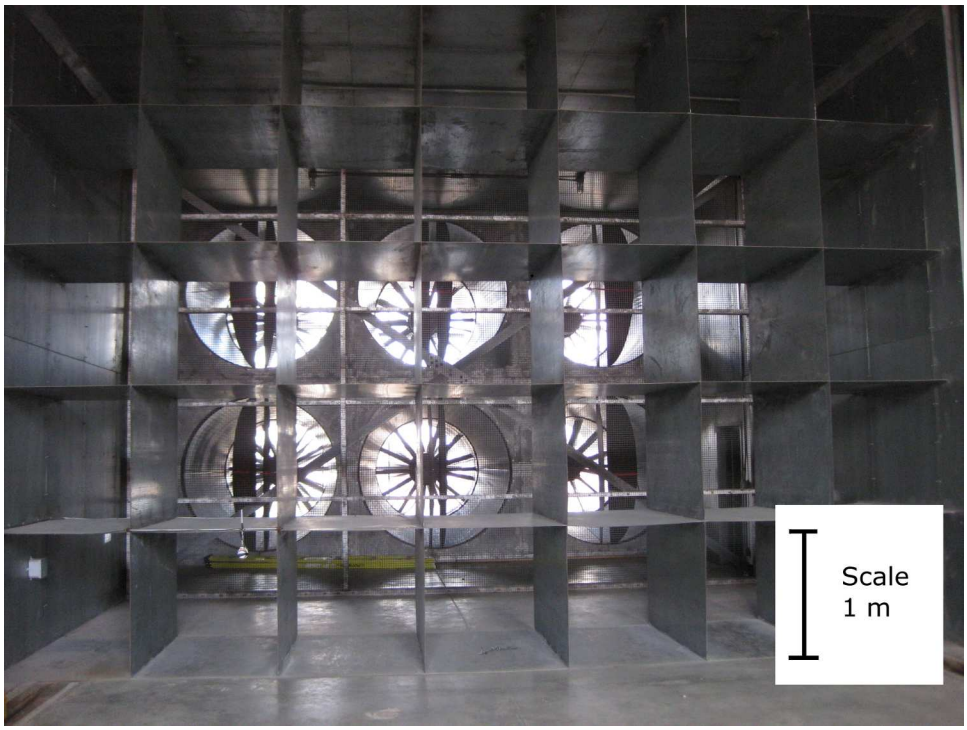

Figure 3.2: Fan exit looking from downstream

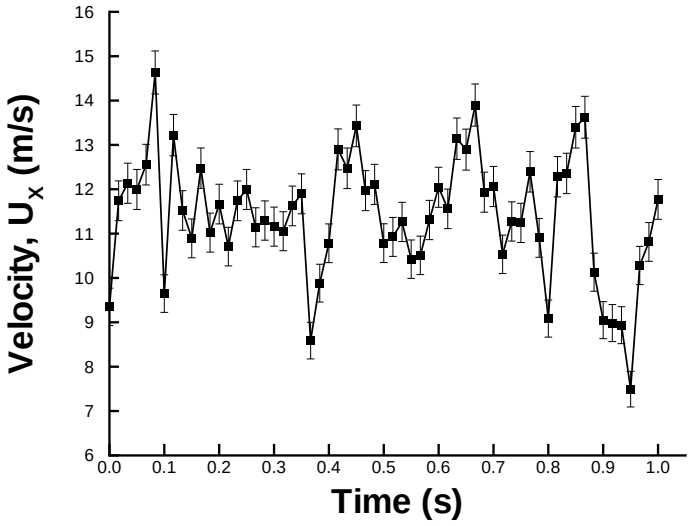

Figure 3.3: Sample velocity data at a fan setting of 60 Hz measured using the sonic anemometer, with single sample error shown, mean velocity of 11 m/s

3.2.1 Wind Velocity Characteristics

The data collected with the sonic anemometer was used to determine the correlation between the frequency settings on the fan and the wind velocity as well as to estimate the turbulence levels in the wind tunnel. A sample of the data collected, shown in figure 3.3, demonstrates the streamwise velocity fluctuation due to large scale turbulence when the fans are operating at their full speed of 60 Hz. Single sample error bars are also shown in figure 3.3 based on an error analysis of the data found in appendix B.

3.2.2 Fan Frequency to Velocity Correlation

The data given in table 3.1 also allows a correlation between the frequency setting and the velocity produced. This relationship, shown in figure 3.4, shows a strong linear relationship between the frequency and velocity, with error bars shown to demonstrate the variability in the raw anemometer output. The linear fit given in equation 3.1, with a R^2 value of 0.997, had an assumed zero velocity intercept due to the characteristics of the system.

$$U_\infty = 0.1844 \times f_{fan} \tag{3.1}$$

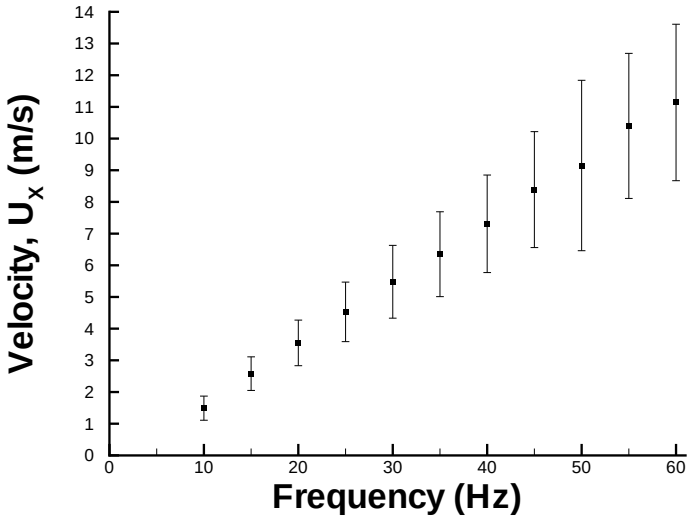

Figure 3.4: Relationship between fan frequency and streamwise velocity

3.2.3 Turbulence Intensity

This figure demonstrates the high level of fluctuation within one second of data. Based on an analysis of data collected the free stream turbulence intensity could also be calculated using the mean velocity for a given fan frequency and the standard deviation of the sample in equation 3.2.

$$I_T = \frac{\sigma_U}{\overline{U_\infty}} \tag{3.2}$$

The turbulence intensity was then calculated for a range of fan settings from 10 Hz to 60 Hz in 5 Hz increments. The results of this testing are summarized in table 3.1, with each velocity data set typically comprised of more than 60000 samples. This table shows that the turbulence intensity was on the same order of magnitude during all tests. The variance in the data, notably at 10 Hz and 50 Hz, could be due to environmental changes in testing or changes in fan operation at specific settings.

3.3 Turbine Assembly

The turbine assembly is comprised of all major components of the wind turbine test apparatus including: the tower, nacelle, blades, generator and the drivetrain. The tower consists of two poles connected at the top and bottom via plates and I-beams; a set of axial braces to provide thrust load bracing; and guy wires for torsional stiffness. The tower poles were designed to carry the static loading from

Table 3.1: Turbulence intensity over a range of fan settings

$Freq$ (Hz)	$\overline{U_X}$ (m/s)	σ_U (m/s)	I_T
10	1.49	0.19	12.73%
15	2.58	0.27	10.38%
20	3.55	0.36	10.18%
25	4.53	0.47	10.45%
30	5.48	0.58	10.60%
35	6.35	0.68	10.71%
40	7.31	0.78	10.67%
45	8.39	0.93	11.07%
50	9.15	1.37	14.93%
55	10.40	1.16	11.16%
60	11.14	1.25	11.27%

the turbine as well as the dynamic loading from aerodynamic forces on the blades and structure.

The nacelle provides the structure and support for the blades, generator and drivetrain. The nacelle was designed with current and future work in mind and was bolted together, instead of welded, to allow for relatively easy dis-assembly and modification. This nacelle and the tower support structure were designed by Michael McWilliam and this design process was extensively documented in his MASc thesis [28]. A detailed schematic of the turbine assembly can be found in figure 3.5 along with photos of the installed assembly in figures 3.6 through 3.7. A detailed description of the installation and decommissioning process can be found in Appendix C.

3.3.1 Modifications

Some modifications were made to the original design in order to accommodate a different blade arrangement than was originally incorporated into the nacelle and tower design. A solid model of the modified blade mounting system is shown in figure 3.8. Also safety concerns lead to the design and implementation of a emergency brake system. The blade diameter was also increased from the original design and thus thrust bracing was installed to compensate for loads that could exceed original design limits. A more detailed discussion of the brake system and thrust bracing can be found in the following sections.

3.3.1.1 Brake Design

An emergency brake was designed and connected to the low speed shaft on the nacelle. This brake was incorporated in order to have an alternative method of

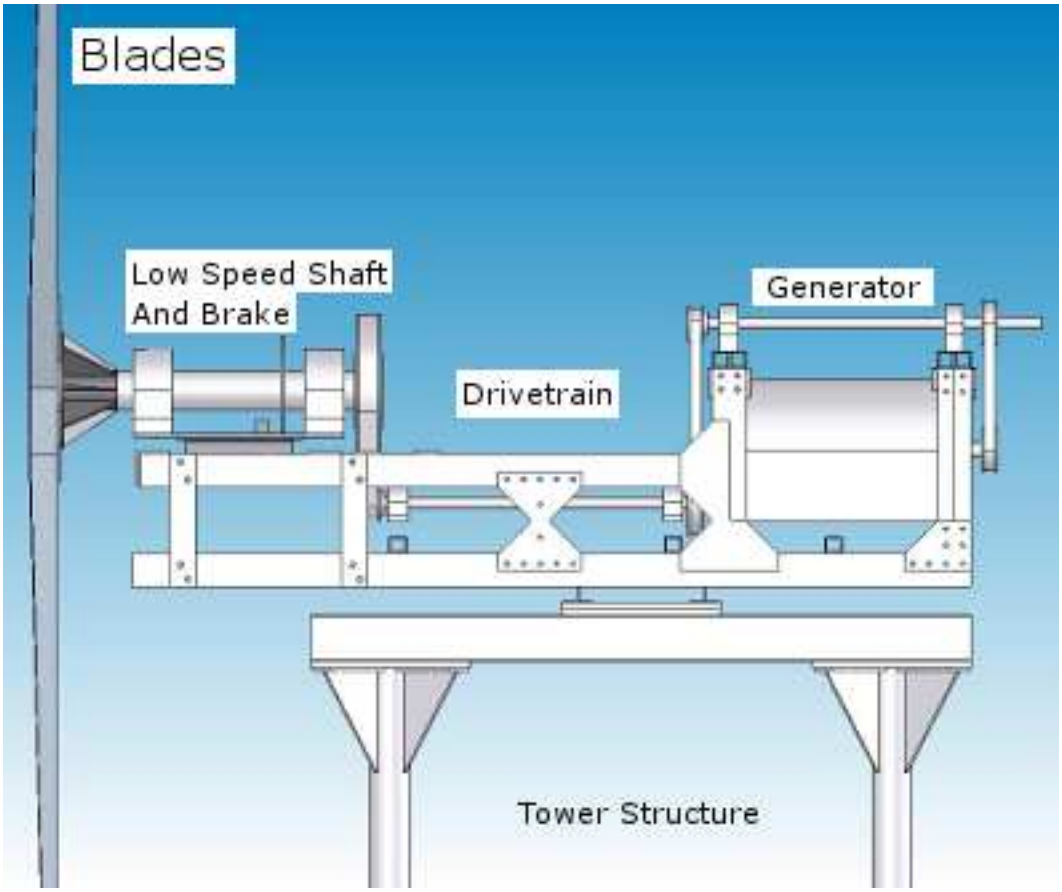

Figure 3.5: Turbine assembly CAD model: profile view [28]

Figure 3.6: Turbine assembly photo: Angled view with load bank, camera and laser system in place

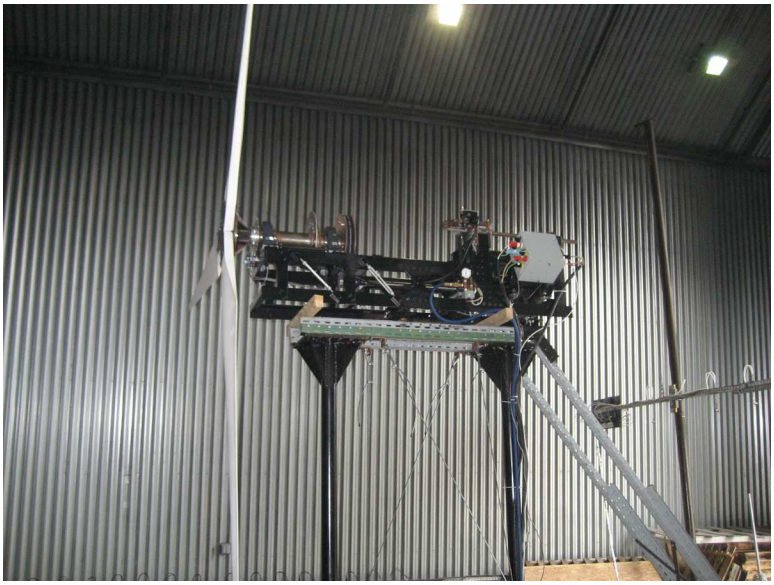

Figure 3.7: Turbine assembly photo: Profile view of nacelle

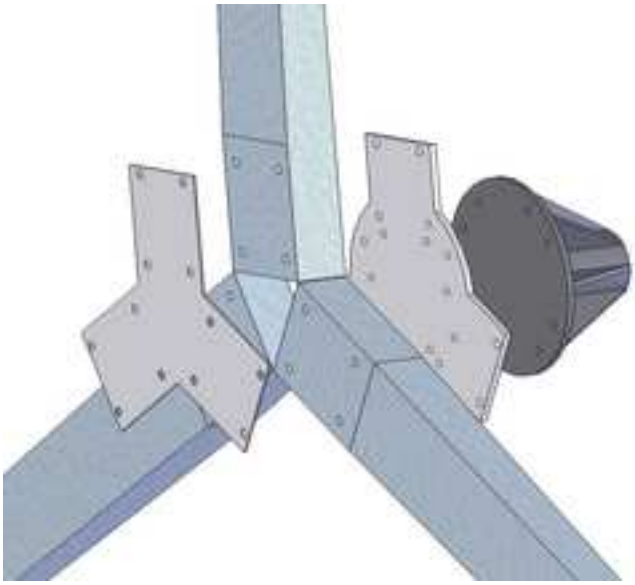

Figure 3.8: Exploded view of mounting plates

stopping the rotation of the blades if the connection between the generator and the blades was broken. This could happen if any one of the three belts in the drivetrain broke during testing or if any of the six pulleys began to slip on their shafts. Since the drivetrain is the connection between the blades and the generator, and thus the primary electrical load device, if the connection was severed during a test the blades could potentially over-speed and fail.

Calculations were made by a member of the wind turbine research group to determine the torque necessary to stop the blades and a system was developed around these required values. Due to it's compact nature and load capabilities a hydraulic brake system from a motorcycle was adapted to the test apparatus.

The initial design criterion for the actuating the brake was a system which under any failure would apply the brake. It was ultimately decided that spring force would be used to apply the force to the brake cylinder. Release of the brake was provided by an air cylinder which was used to extend two springs, thus removing braking force, from a naturally closed state. In this configuration, pressure was vented from the air cylinder system, through an air valve, in order to provide braking force and if an air line were to be accidentally disconnected the brake was also applied. This configuration was almost fail safe as the only brake failure mode would be the springs becoming disconnected from the actuator. An overall schematic of this system can be found in figure 3.9 with photos of the major components found in figures 3.10 to 3.11.

3.3.1.2 Thrust Bracing

With the increase in rotor diameter and number of blades from the original design the estimated aerodynamic thrust loading, based on the same criteria outlined in

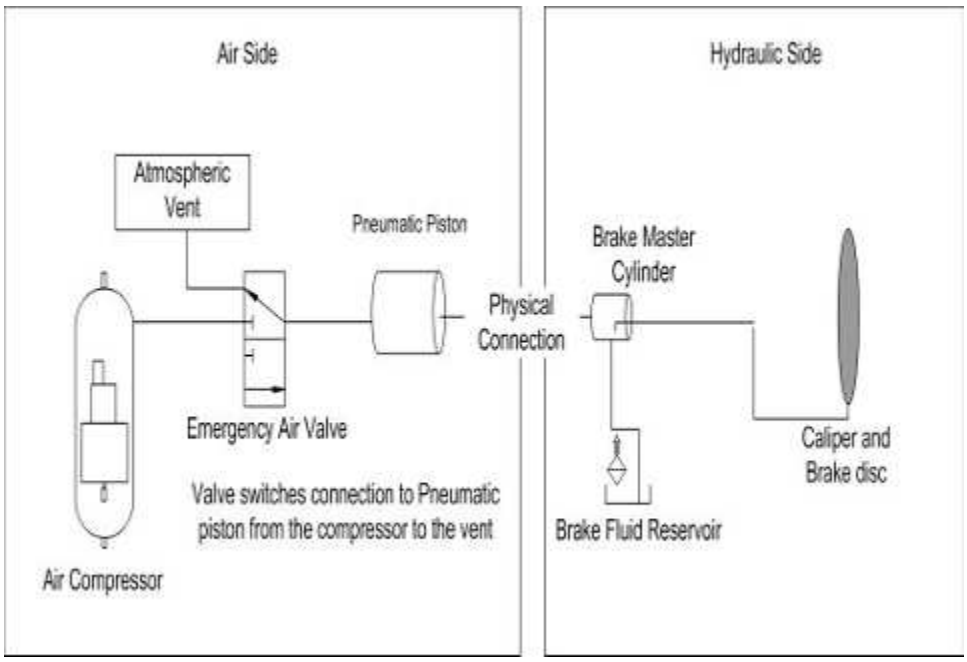

Figure 3.9: Brake system schematic

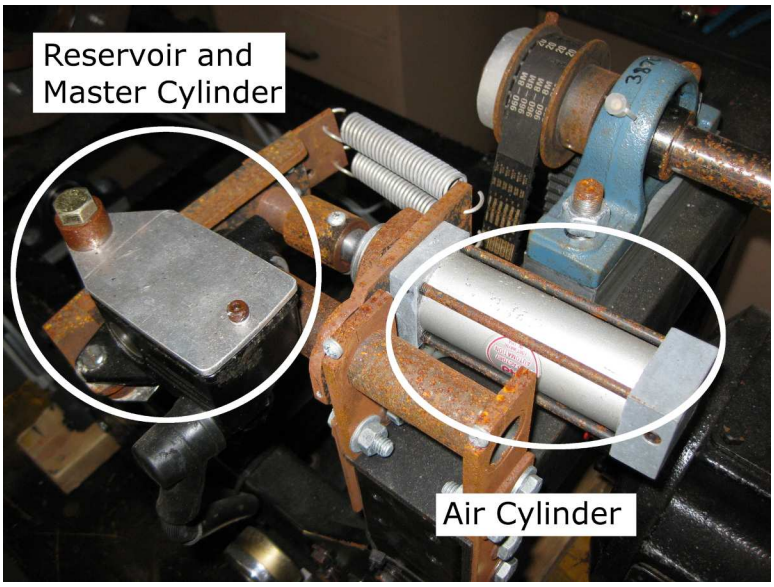

Figure 3.10: Brake system photo: Air cylinder and master brake cylinder

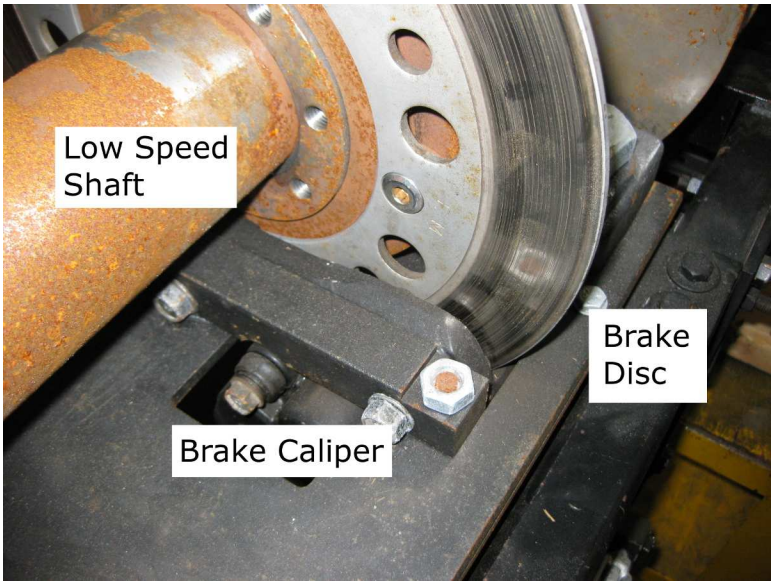

Figure 3.11: Brake system photo: Calipers and disc mounted on the low speed shaft

McWilliam [28], exceeded the original design limit. The original apparatus was designed for a maximum thrust of 1 kN with a safety factor of 2. The original design criteria was calculated for: a wind speed of 13 m/s; a coefficient of thrust, C_T found in equation 3.3, of 1.2; and air density of 1.2 kg/m^3. Using these same variables the estimated thrust loading for the new blade design was found to be 1.8 kN. In order to compensate for potentially higher loading members of the wind turbine research group designed and constructed axial bracing which extended from the back of the original rig to the footing.

$$C_T = \frac{F_N}{\frac{1}{2}\pi\rho V^2 R_T^2} \tag{3.3}$$

3.4 Turbine Blades

The blades manufactured for and used in this experiment were made from an existing blade mould and design. A local company, Composotech [30], had a blade mould in their possession which could be successfully adapted to the existing apparatus. Composotech could not positively identify the turbine for which the blades were designed; but, based on a qualitative comparison between specifications and photos, they closely resembled a blade manufactured for Southwest Windpower [31], which is a company based in Arizona. The blade outlined on the company website matched the blade length of the manufactured blades as well as the expected energy output of a two bladed design, based on a BEM analysis. Southwest Windpower could not comment on this blade specifications due to the proprietary design but through a procedure, outlined in section 3.5, the aerodynamic properties were de-

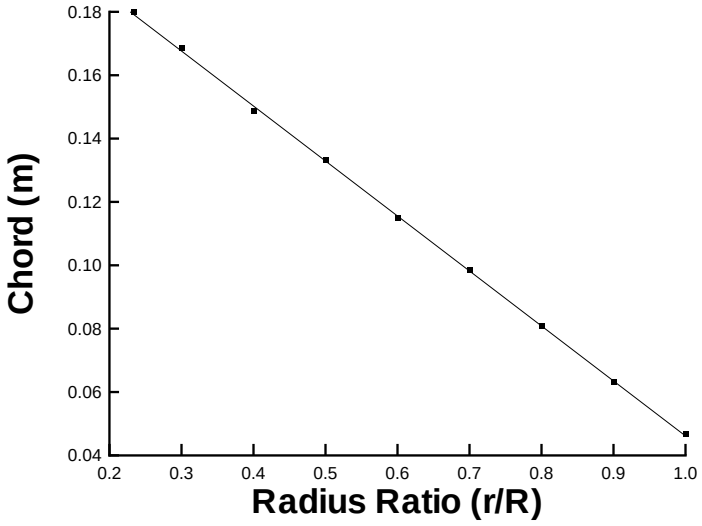

Figure 3.12: Measured chord distribution of the manufactured turbine blades

termined. A detailed description of the blade manufacturing process can be found in appendix D.

3.5 Blade Geometry

In order to effectively model the performance of the wind turbine, the blade geometry of the manufactured blades were determined. The blade parameters which were determined include the chord, twist and airfoil distribution.

3.5.1 Chord and Twist Measurements

Measurements at nine points along the blade length were made to determine the chord and twist distribution. Due to the design of the blades the aerodynamic section of the blade did not start until a radius ratio of approximately 23% and the root section was thus ignored in aerodynamic analysis. The chord distribution was measured and found to be linear which was expected for a basic blade design which considers ease of design and mould construction. The linear curve fit for the chord is shown in equation 3.4 with the distribution shown in figure 3.12.

$$C(r/R_T) = -0.174 \times (r/R_T) + 0.220[m] \tag{3.4}$$

The twist distribution was found by measuring the relative height between the trailing and leading edge when the blade was laid flat on a table. Based on a right angled triangle, with the chord as the hypotenuse, the blade set angle at

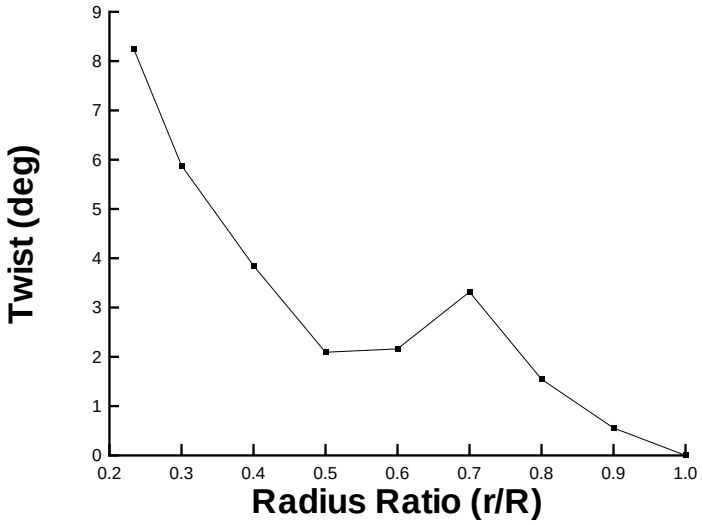

Figure 3.13: Twist distribution of the manufactured turbine blades

that point can be found and the twist found based on the tip β as a reference. The resulting distribution was found to be irregular which could be due to mould irregularities or measurement error due to challenges determining the exact location of the leading and trailing edge. Due to the irregularities a polynomial curve fit was not appropriate so analysis was completed with a look-up table which listed the blade set angle at regular radial points along the blade. The resulting twist distribution can be found in figure 3.13. This irregular distribution also resulted in irregular calculated values from the BEM model which is discussed in the BEM results, section 5.2.4.

3.5.2 Airfoil Distribution

The airfoil distribution was determined at three points along the blade: root, mid-section and tip; in order to select a suitably representative airfoil to be used in C_L and C_D calculations. In order to determine the airfoil coordinates three moulds of the blade were made using cardboard casings which were injected with expanding foam. Once this was allowed to cure the casings were removed from the blade and resulting moulds were cut at their midpoint to reveal the airfoil shape. An image of these moulds was copied into a CAD package, SolidWorks [32], and coordinates along the outside of the airfoil shape were taken. Through trial and error, NACA four digit series blades were compared to the blade shape until a reasonable approximation was found. This process ultimately will result in some error but it still allowed for a reasonable approximation to be found for each section. To illustrate the airfoil shape process images of the casings on the blade and a completed mould can be found in figures 3.14 and 3.15.

Figure 3.14: Mould casings in place along a finished blade at the root, mid-section and tip

Figure 3.15: Tip mould casing removed from blade and cut at midpoint

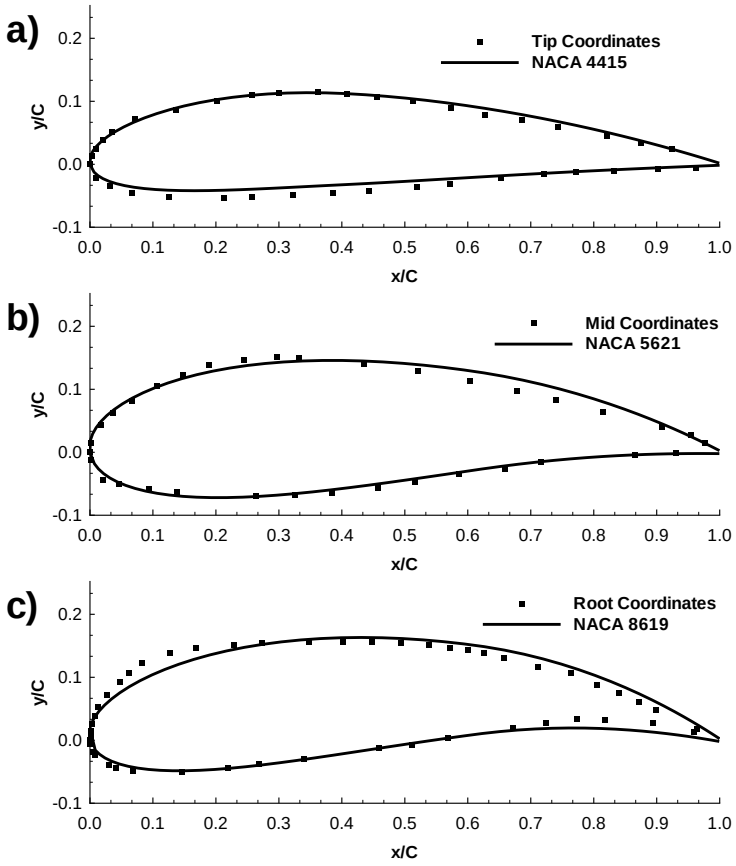

Figure 3.16: Measured blade coordinates compared with NACA profiles: a) the tip, b) middle and c) root

The resulting profiles for each blade section from tip to root are shown in figure 3.16 with the best fit NACA four digit series profiles being the 4415, 5621 and the 8619 respectively [33]. The root and the mid-section had the highest error in the comparison due to their high camber and thickness. In all profiles the upper section near the trailing edges seem to have the worst fit while the root also had a poor fit on the lower part of the trailing edge and the upper leading edge.

3.6 Airfoil Aerodynamic Properties

Due primarily to the availability of its C_L and C_D curves, and ease of implementation in a basic BEM model, a NACA 4415, which matched the tip profile, was used to represent the entire blade. While this simplification could introduce errors this was deemed acceptable in order to simplify the model. Multiple sources of two dimensional NACA 4415 lift and drag curves were found and represented a variety of Reynolds numbers, aspect ratios, surface roughness's and angle of attack (AOA) ranges.

Table 3.2: Aerodynamic property data sets used for BEM calculations with original data parameters and the method used for data extrapolation

Data set title	Original data used	$AOA\,Range$ (deg)	Re
$Abbot\,Original$ $Abbot\,C_D\,Viterna$ $Abbot\,C_D\,Flat$ $Abbot\,Viterna$ $Abbot\,Flat$	Abbot and Von Doenhoff. [1]	-14 to 20	3×10^6
$Hoffman\,Viterna\,Raw$ $Hoffman\,Flat\,Raw$ $Hoffman\,Viterna$ $Hoffman\,Flat$	Hoffman et al. [2]	-20 to 40	7.5×10^5
$Ostowari\,Raw$ $Ostowari\,Viterna$ $Ostowari\,Flat$	Ostowari et al. [34]	-10 to 108	7.5×10^5
$Xfoil\,Viterna$ $Xfoil\,Flat$	Xfoil [35]	-18 to 17	1×10^5

While other data exists, the primary sources of experimental and computational NACA 4415 lift and drag used in this analysis were given by: Abbot and Von Doenhoff [1], Hoffman et al. [2], Ostowari and Naik [34] and Xfoil [35]. Where available the lowest Reynold's number data set was selected but it should be noted that the lowest Reynold's number within the literature experimental data sets was typically on the order of 1×10^6 whereas the maximum expected Reynold's number for the experiments was on the order of 1×10^5. Additionally, while some of the selected data sets quantified surface roughness and aspect ratio affects, the data used assumed no roughness and an infinite aspect ratio.

Except in the Ostowari data set the AOA range covered was not sufficient to provide lift and drag values for the BEM solver. The absence of data over the required AOA range was corrected by extrapolating the original data using the AirfoilPrep [36] preprocessing Excel worksheet, prepared by NREL, to estimate the lift and drag through an AOA range from -180 to 180 degrees.

In total fourteen data sets were developed and tested within the BEM model: five models were based on the Abbot's data, four on Hoffman's, three on Ostowari's and two on the Xfoil analysis. The aerodynamic property data sets used for BEM calculations are each discussed in detail in the sections to follow and are summarized in table 3.2 which includes: the original source of each data set, the angle of attack range covered by the original data and the Reynold's number.

3.6.1 Lift and Drag Extrapolation

The AirfoilPrep worksheet was able to provide the tools necessary to extrapolate a given data set to encompass a full AOA range of -180 to 180 degrees. The worksheet also contains tables to correct for three dimensional flow but this was not utilized for this basic analysis. Original AOA ranges prior to extrapolation were typically between -10 and 20 degrees while typical AOA values required for this BEM analysis were between -10 and 90 degrees. AirfoilPrep relies on extrapolation methods outlined by Viterna and Janetzke [37] to predict C_L and C_D beyond a given data sets maximum AOA, defined as α_{ref}.

Aerodynamic property extrapolations, given in equations 3.5 and 3.6, were developed by Viterna and Janetzke [37] and were used to extrapolate the aerodynamic properties to an AOA of 90 degrees. These coefficients are based on a user input of the maximum C_{Dmax} which, by default, was calculated, using equation 3.7. The C_{Dmax} value was based on the aspect ratio (AR) of the blade, found using equation 3.8 to be 14.5.

$$C_L = \frac{C_{Dmax}}{2} sin\left(2\alpha\right) + A_2 \frac{cos^2\left(\alpha\right)}{sin\left(\alpha\right)} \tag{3.5}$$

$$C_D = C_{Dmax} sin^2\left(\alpha\right) + B_2 cos\left(\alpha\right) \tag{3.6}$$

where,

$$C_{Dmax} = 1.11 + 0.018AR \tag{3.7}$$

$$AR = \frac{R_T^2}{\frac{1}{2}CR_T} = \frac{2R_T}{C} \tag{3.8}$$

$$A_2 = \left[C_{Lref} - \frac{C_{Dmax}}{2} sin\left(2\alpha_{ref}\right)\right] \frac{sin\left(\alpha_{ref}\right)}{cos^2\left(\alpha_{ref}\right)} \tag{3.9}$$

$$B_2 = \frac{C_{Dref} - C_{Dmax} sin^2\left(\alpha_{ref}\right)}{cos\left(\alpha_{ref}\right)} \tag{3.10}$$

Beyond 90 degrees and below the data sets minimum AOA the lift and drag coefficients are calculated based on the original Viterna calculations but are reflected and scaled, as required, with the details of this process outlined in the AeroDyn theory and user manuals [38, 39].

Alternatively, the user has the option to calculate the C_D value, based on flat plate theory given in equation 3.11, which relates C_D to C_L using the airfoil's AOA, with the C_L still calculated based on the Viterna equation.

$$C_{Dflat} = C_L tan\left(\alpha\right) \tag{3.11}$$

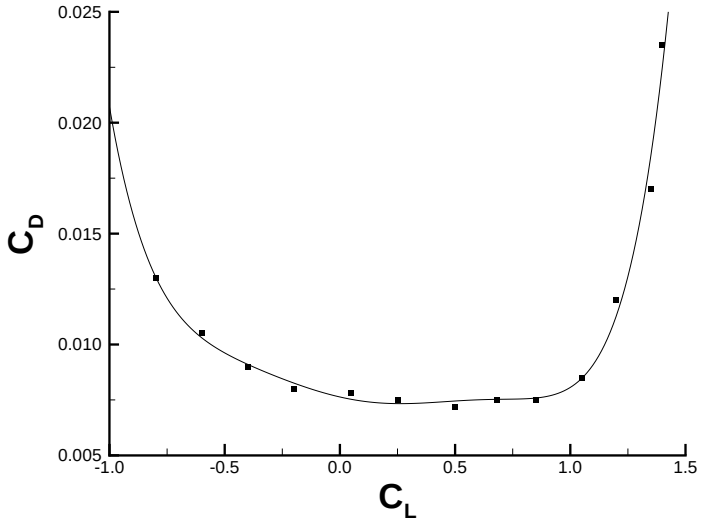

Figure 3.17: Coefficient of drag as a function of the coefficient of lift [1]

3.6.2 Lift and Drag Data sets

3.6.2.1 Abbot and Von Doenhoff [1]

Five of the fourteen functions used were based on the Abbot and Von Doenhoff [1] lift data which was limited to an AOA range of -14 to 20 degrees. This data set was unique in that the C_D values were based on the C_L instead of as a function of AOA, as shown in figure 3.17. A sixth order polynomial fit to the drag coefficient data was first found based on the coefficient of lift, shown in equation 3.12, and was used in three of the functions based on the Abbot data. This polynomial fit was also used to determine the drag as a function of AOA based on the lift coefficient at a given AOA, in order to use the AirfoilPrep worksheet. While this technique resulted in irregular C_D data at low AOAs it was still implemented for completeness.

$$C_D = 0.0077C_L^6 - 0.0063C_L^5 - 0.0054C_L^4 + 0.0024C_L^3 + 0.0045C_L^2 - 0.0024C_L + 0.0076 \tag{3.12}$$

The first function, referred to as *Abbot Original*, utilized a linear extrapolation from the final data point at 20 degrees to the theoretical zero lift at an AOA of 90 degrees and below -14 degrees the lift was assumed constant, as shown in equation 3.13; while the drag was modeled using the polynomial curve fit. This model was expected to poorly match low TSR experimental data as this is the regime which, in theory, would experience high angles of attack, which was the area at which this model was weakest.

The second and third functions, referred to as *Abbot C_D Viterna* and *Abbot C_D Flat*, used the AirfoilPrep extrapolation of the Abbot data set for the lift data while

using the polynomial curve fit for drag calculations. The final two functions, *Abbot Viterna* and *Abbot Flat*, fully utilized the AirfoilPrep worksheet to extrapolate the lift and drag data over the entire AOA range.

$$C_L(\alpha) = \begin{cases} 0.084615 \times \alpha + 0.285 & -14 < \alpha < 14 \\ -0.9 & \alpha \leq -14 \\ -0.0125 \times \alpha + 1.45 & 14 \leq \alpha \leq 20 \\ -0.01728 \times \alpha + 1.555 & \alpha > 20 \end{cases} \tag{3.13}$$

3.6.2.2 Hoffman et al. [2]

Four functions were based on the Hoffman et al. data set [2] which extended from -20 to 40 degrees for both lift and drag. While the purpose of their study was to determine the effects of surface roughness the data used in this study was for a clean airfoil at a Reynold's number of 0.75×10^6, which was the lowest Reynold's number available. All four data sets used the AirfoilPrep worksheet to extrapolate the data; however, two of the sets used the full range of available data while the other two were extrapolated from the data covering -10 to 17 degrees. Based on the outlined criteria, the first two sets, extrapolated from the full available data, were referred to as *Hoffman Viterna Raw* and *Hoffman Flat Raw* with the other two named *Hoffman Viterna* and *Hoffman Flat*.

3.6.2.3 Ostowari and Naik [34]

Three functions were based on the Ostowari data set [34] which covered a range of -10 to 108 degrees for both lift and drag. The purpose of Ostowari's study was to determine the affects of varying the aspect ratio over a range of Reynold's numbers. The data set used in this BEM study were for an infinite aspect ratio and at a Reynold's number of 0.75×10^6. Since the raw data from Ostowari covered a sufficient AOA range it was used in it's raw form, referred to as *Ostowari Raw*, for a BEM study. To correct for aspect ratio effects the AirfoilPrep worksheet was used to extrapolate data from the -10 to 17 degree data range with the output referred to as *Ostowari Viterna* and *Ostowari Flat*. Completing the extrapolation also allows a comparison of data before and after the AirfoilPrep corrections to understand it's effects.

3.6.2.4 Xfoil [35]

Two functions were based on the Xfoil [35] computational results which covered an angle of attack range from -18 to 17 degrees for lift and drag. A viscous model was used with a Reynold's number of 1×10^5 and a mach number of 0.1. The AirfoilPrep worksheet was used to extrapolate the data with the output called *Xfoil Viterna* and *Xfoil Flat*.

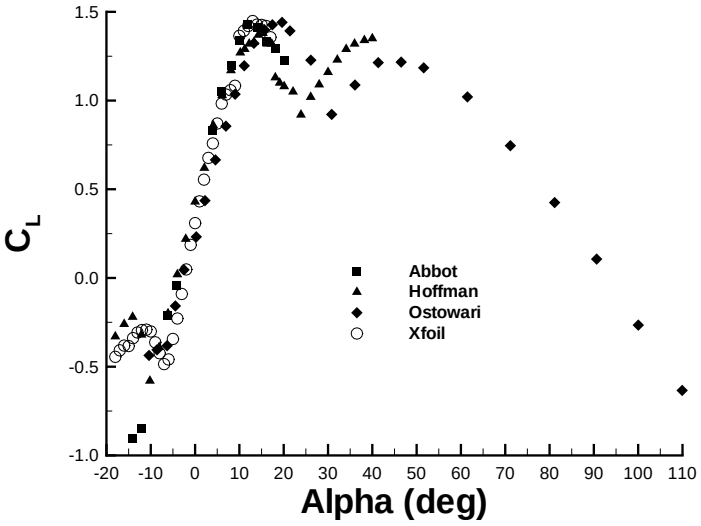

Figure 3.18: Lift coefficient as a function of α [1, 2, 34, 35]

3.6.2.5 Data Comparison

The raw data from the four sources was compared to determine the differences in the source material. In the three experimental sources the Reynolds number in the testing varied from 3×10^6 for the Abbot data to 0.75×10^6 for the Hoffman and Ostowari data. Figure 3.18 shows the lift coefficient data as a function of the angle of attack over the full range of available data in the original sources. This figure demonstrates that from -10 through to 15 degrees the lift is similar in all four data sets while the stall characteristics of the Ostowari data set differs from Abbot, Hoffman and Xfoil.

The drag characteristics of the four data sets are shown in figure 3.19. The Hoffman, Ostowari and Xfoil data sets show similarities and common trends whereas the Abbot data does not demonstrate the increase in C_D that would be expected at high and low angles of attack.

Finally a comparison can be made between the Ostowari original data and the AirfoilPrep extrapolations based on the data from -10 to 17 degrees. Figure 3.20 shows the lift data from the raw data and the *Viterna* extrapolation, note that the *Ostowari Flat* data is not shown as the lift data is identical for both extrapolation methods. The lift coefficient comparison demonstrates the extrapolation maintaining the same values as the raw data through to 17 degrees where the Viterna equations take affect. Also of note in this comparison is the raw data having a higher lift coefficient through most of the high angles of attack which has the most effect at low TSRs.

The drag coefficient comparison between the Ostowari data and the Viterna and Flat plate extrapolations is shown in figure 3.21 which demonstrates a large degree

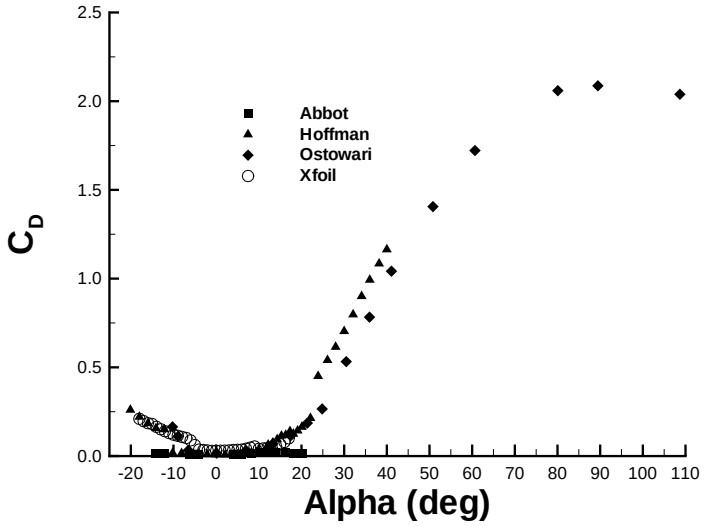

Figure 3.19: Drag coefficient as a function of α [1, 2, 34, 35]

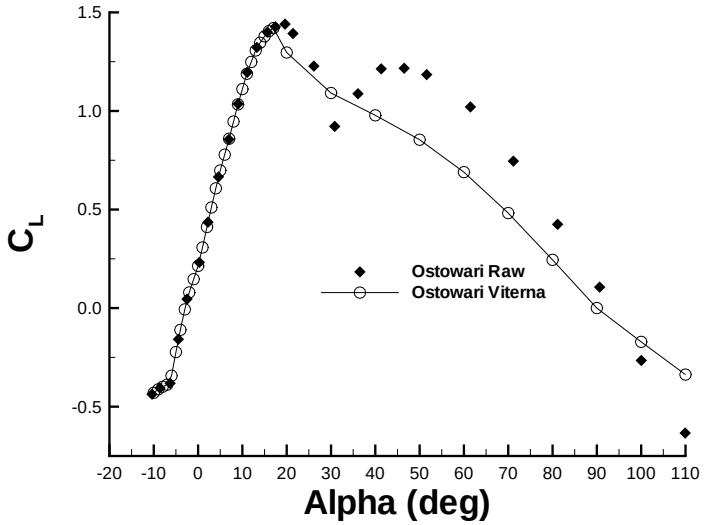

Figure 3.20: Lift coefficient comparison between raw data and the Viterna extrapolation [34]

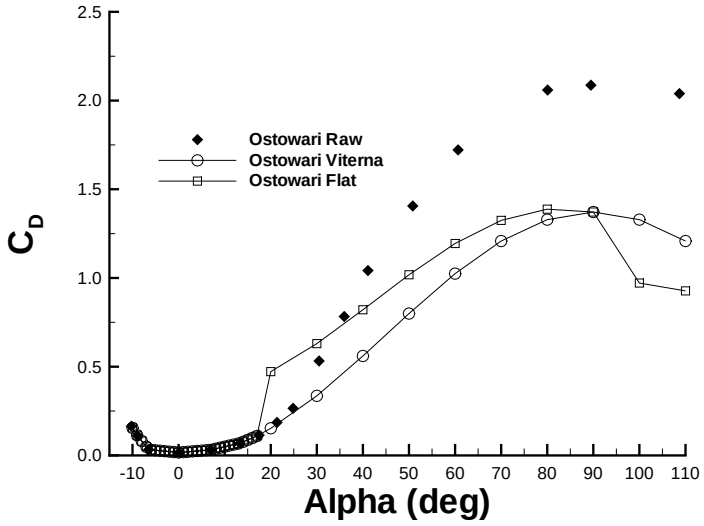

Figure 3.21: Drag coefficient comparison between raw data and the AirfoilPrep extrapolations [34]

of variability in the expected value. Again in this comparison the raw data has a higher drag coefficient at high angles of attack.

3.7 PIV Equipment

In order to complete the flow measurement portion of the experiment a PIV system was utilized. In order to perform measurements on the rotating system in the large wind facility some auxiliary components were added primarily to facilitate the timing of the image capture over a range of rotational rates. The components used and the existing PIV system are outlined in the following sections.

3.7.1 Control

The PIV process required the precise timing and control of a laser and camera system in order to produce results. A preassembled control box from Dantec Dynamic systems, P1100, was utilized to provide this control. The P1100 communicated, through a local network connection, with a computer in the control room and then relayed commands to the camera and laser to match the settings input by the user. This requires a software interface for the user's PC, Flow Manager [40], which allowed the user to specify all aspects of the experiment from equipment being used to the timing of the images to be captured.

The user first specified the laser and camera to be used in the experiment which, for this experiment, are discussed in sections 3.7.2 and 3.7.3. The firing method was

then selected as triggered firing; this setting will only fire the system when a trigger pulse from the experimental setup was received. This firing method was utilized in this experiment as the blades were rotating and this would limit the system to fire only when the blade was at a specific point in it's rotation.

3.7.2 Camera

The camera used in the PIV setup was a Kodak Megaplus ES 1.0 camera [41]. The purpose of the camera, in this experiment, was to capture the seeding particles as they traveled around the turbine blade. The PIV method required two frames to be captured with a relatively small time between the frames. This particular camera utilizes frame straddling to achieve rapid frame rates. Instead of having rapid shutter speeds, on the order of microseconds, this process controls the firing of a laser, the light source, to be near the end of one frame and the beginning of the next frame. Essentially removing the control of the frame rate from the camera's shutter and using the laser to finely adjust the inter-frame time.

For this experiment the camera was held in the stationary domain while the blade rotated through the field of view. Ultimately the camera was placed 20 cm from the tip and was imaging an area at a plane located 22.1 cm inboard from the blade tip which translates to a point at a radius ratio of approximately 90%. The overall image area was approximately 16 cm by 16 cm with the camera having a resolution of 1008 by 1018 pixels.

Additionally a wavelength notch filter was placed on the camera to filter out ambient light from the sun and ambient lighting in the wind facility. This filter will only allow the wavelengths of light at 532 nm, the laser wavelength, to reach the imaging sensor. Due to the nature of the wind facility, with large areas open to the outside atmosphere, it was crucial to remove sunlight from the images and only image the area of interest at the blade.

3.7.3 Laser

The laser in a PIV setup is the light source and must be able to output two laser pulses close together with each laser pulse lasting a short duration. As described above, section 3.7.2, the laser is effectively used as a shutter which is why the pulse duration must be short to avoid the particle motion being blurred. In order to have two laser pulses close together the lasers utilized in PIV setups often have two independent lasing cavities. In this system a New Wave Gemini dual Nd:YAG was originally used. This laser had two laser cavities each of which could produce a 130 mJ laser pulse with a pulse width between 3 and 5 ns. Ultimately this laser had a critical failure and was replaced with a lower energy laser. The laser used was a New Wave Solo II dual Nd:YAG [23] with 30 mJ energy output and a pulse width between 3 and 5 ns. This laser was used as it was made by the same manufacturer

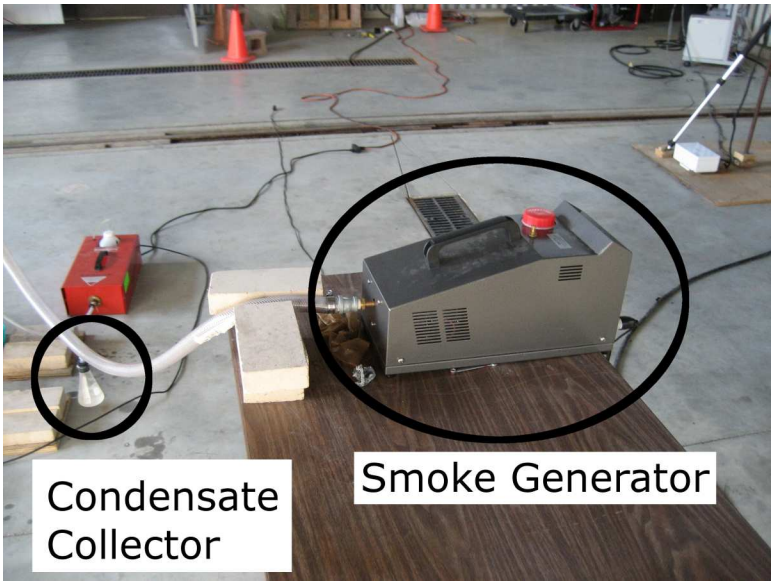

Figure 3.22: Final seeding method smoke generator and condensate collector

and shared a common trigger wiring system which allowed it to adapt to the existing system setup.

3.7.4 Seeding

A smoke generator is typically used to seed air flows with particles in order to track the flow in the area of interest. Achieving a homogeneous smoke distribution within a closed loop wind tunnel can often be a simple process as the flow, by definition, recirculates which means that injected smoke does not easily disperse. In this experiment the challenges experienced in seeding the flow were mainly attributed to: the open-loop wind facility which required constant flow seeding; high levels of turbulence; and the external flow inherent to the area being imaged.

Numerous methods for mixing the smoke with the free stream flow and containing it in the area of interest were attempted along with placement of the smoke outlet. As a reference for potential future work methods which failed to produce useful results are outlined in appendix E.

Ultimately a high volume water-based smoke generator was placed upstream with a 2.54 cm hose attached to the generator output with a beaker to collect condensation generated in the hose during use. The hose outlet was adjusted until the area of interest was, on average, being seeded. Due to turbulence a larger area than required was seeded to allow some smoke particles to be in the area of interest at all times. Examples of this final seeding setup can be found in figures 3.22 and 3.23. This final method did not achieve adequate seeding in all images so validation techniques, outlined in section 4.2.6, had to be utilized in an attempt to extract useful information from the captured images.

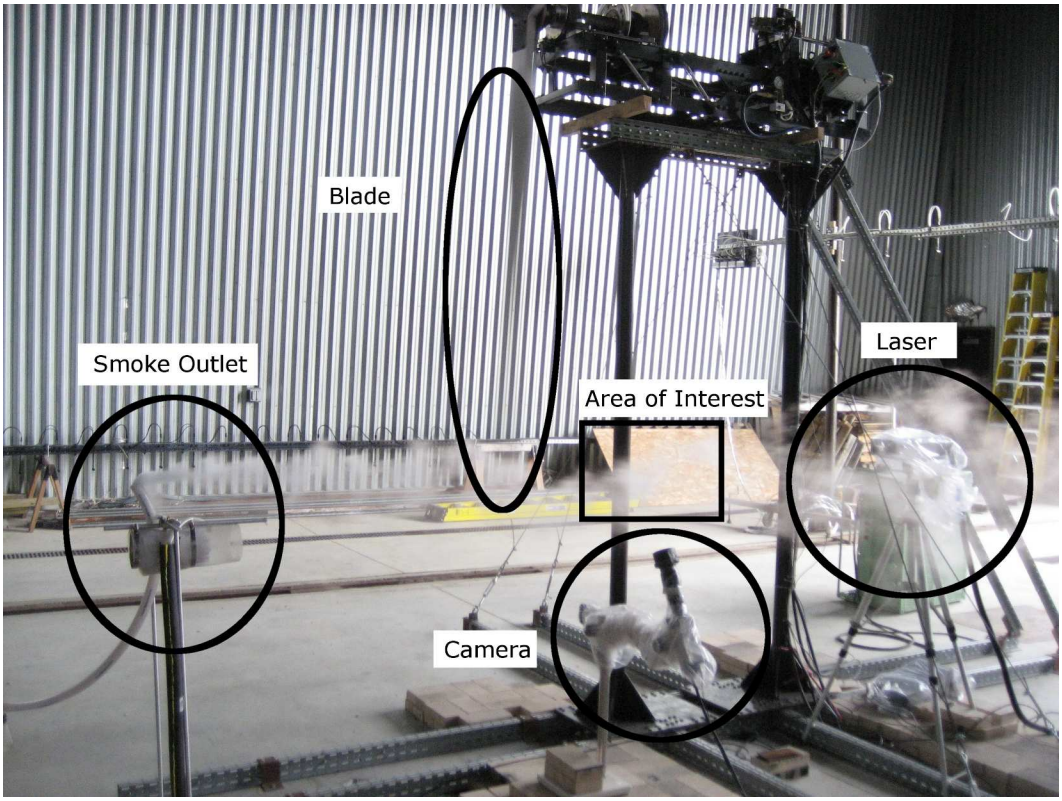

Figure 3.23: Final seeding method

3.8 Power Supply and Loading of the Motor/Generator

3.8.1 Overview

In order to both rotate the wind turbine blades and absorb the power it generated an electrical system needed to be designed. The generator used in this system was the basis for the electrical design of the system. It was selected due to it's availability within the University and it's power ratings which matched the work to be done within the scope of this project. As it was a DC generator it was also able to act as a motor without any modification or electrical switching. Due to the dual-mode nature of the generator/motor the generator will also be referred to as a motor if the net power consumption was positive. This dual-mode aspect made it ideal for preliminary testing as well as the relative ease with which the speed can be controlled. The generator was rated for 3.6 kW at 240 VDC and 15 A and required a field current up to 0.76 A as it did not contain a permanent magnet.

With the generator selected, the electrical system required to control it's speed and absorb power generated by the system needed to be built around the generator specifications. This required the design of a system to provide high voltage DC power to the generator as well as a load bank to absorb the power generated

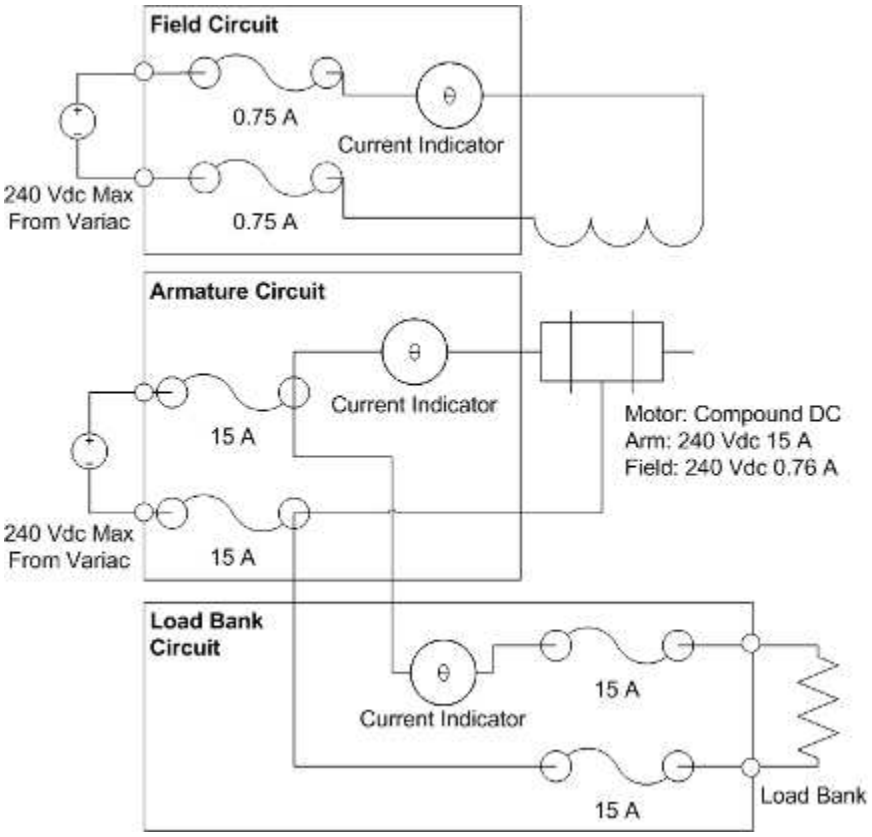

Figure 3.24: Electrical system wiring schematic

by the blades which are outlined in sections 3.8.2 and 3.8.3. A schematic of the entire electrical system is shown in figure 3.24 with each of the components shown discussed in further detail.

3.8.2 Motor Power Supply

In order to provide energy to the motor, which was attached to the drivetrain, the three phase power in the wind facility needed to be converted to a DC variable power source. The facility was equipped with three phase delta 208 VAC power with each leg rated for 30 A. As the power was AC it was rectified to DC using a silicon diode bridge prior to reaching the generator.

For the purpose of speed control an AC variac was utilized to changed the voltage being fed into the rectifier from 0% to 100% of the grid voltage. This allows the DC voltage to be adjusted which gave the user fine control over the motor speed as the speed of a DC motor is proportional to the armature voltage, as shown in equation 3.14.

$$\omega_{motor} \propto \frac{V_{arm}}{\Phi} \tag{3.14}$$

A similar system was used to power the field with grid voltage being fed into an independent variac and then into a silicon diode bridge before going to the field windings. If further speed control was required the field voltage could be lowered, referred to as field weakening, which results in the speed increasing. This increase in speed is due to the reduction of the magnetic flux produced by the field when the field voltage is decreased. This decrease in magnetic flux results in an increase in the motor speed, as given by the inverse relationship in equation 3.14. Care must be taken when the field is weakened as the armature current will increase to compensate for the loss in flux in order to maintain constant torque, as given by equation 3.15, and could exceed the motor's rated current if not monitored.

$$T_{motor} \propto I_{arm}\Phi \tag{3.15}$$

3.8.3 Generator Loading

Generator loading was achieved by using a network of resistive elements, referred to as a load bank, to dissipate the energy generated by the turbine blades as heat. If the load bank is disconnected from the generator the power produced by the blades can not be dissipated and the blades could spin out of control and potentially fail. The load bank was comprised of various heater bars, heat coils and light bulbs, which each had a fixed resistance, in order to provide a variety of loading configurations for future experiments. In this experiment the six heater bars available were used exclusively as they were rated for 500 W each giving a total rated absorption of 3000 W. A schematic of the load bank can be found below in figure 3.25 which demonstrates the numerous input points to connect the leads from the motor to the load bank. As previously mentioned input points one and two were used exclusively for this experiment as they allowed all desired ranges of wind speed and rotational rate to be tested.

3.8.4 Wiring Box

A wiring box was mounted to the motor in order to allow easy connection to the armature and field leads attached to the motor. This also allowed for fusing, to prevent damaging components due to high currents, on each of the positive and negative leads to the armature and field windings as well as the output leads going to the load bank. In this experiment the negative leads were not common with ground and as such both positive and negative leads needed to be fused to avoid a short to the grounded chassis. With reference to the overall schematic of the electrical system, shown in figure 3.24, all of the electrical components within the wiring box are contained within the solid lines.

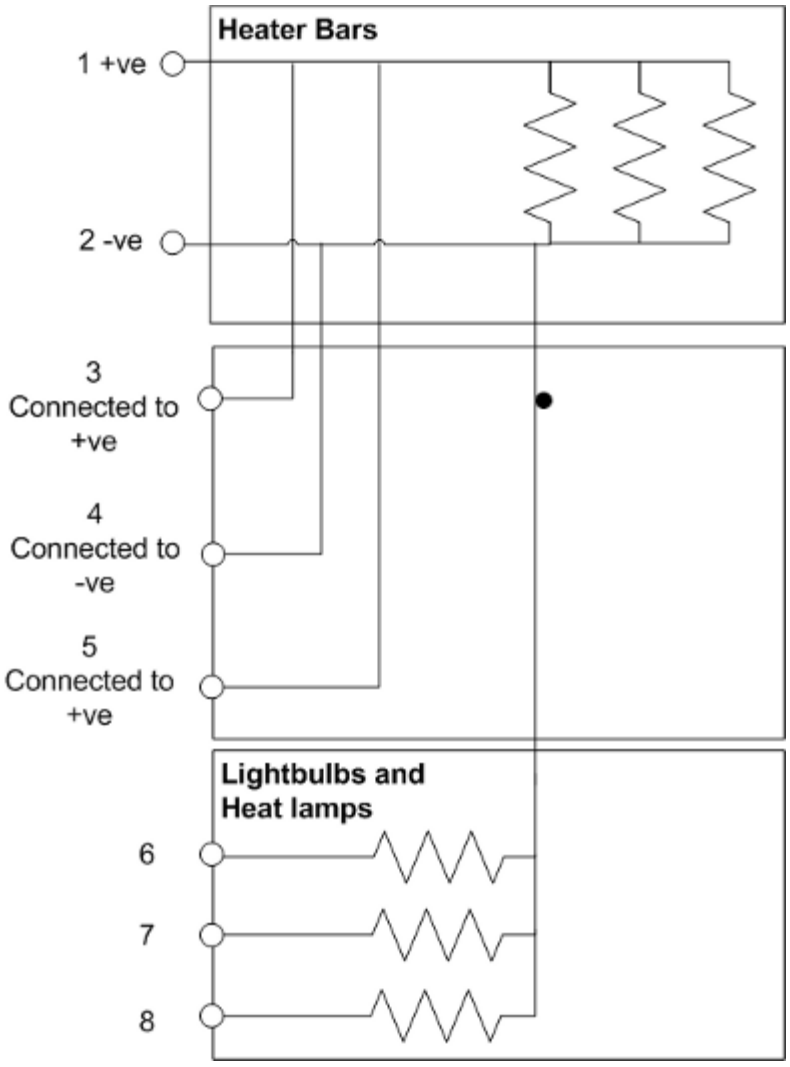

Figure 3.25: Load bank schematic

3.9 Instrumentation

Various instruments were used to quantify the variables associated with this experiment. The instrumentation, hardware and software used are outlined in this section.

3.9.1 Data Acquisition Hardware

Two instruments were used to collect data from the experimental apparatus. The first was a Keithley 2700 [42] multimeter and switch system which was located at the base of the tower within the wind facility. The other data acquisition hardware which was used was a NI (National Instruments) high speed 6251 pci card [43]. The NI card was mounted in the control room within a computer which was used to run the data acquisition software.

The Keithley 2700 was used to collect data for any sensors that may be exposed to high voltage as it is protected for over-voltage up to 1000 VDC. This ultimately meant that the Keithley 2700 was monitoring the motor input voltage and current and the load bank voltage and current. The current shunt resistor output, although only in the microvolt range, could potentially ground to a chassis which would then send line voltage to the data acquisition hardware which is why the Keithley was used for these measurements too. The main disadvantage of the Keithley 2700 was that it was unable to monitor multiple channels simultaneously and as such must physically switch channels in sequence. As the signals being monitored by this device were not changing significantly with time this was not considered a large source of error. The NI 6251 pci card was primarily used to monitor the rotational speed of the low speed shaft as this card had a digital counter hardwired it was able to monitor the rotational speed.

3.9.2 Tunnel Velocity Measurements

Velocity measurements were made using two independent sensors. The primary sensor used was a CSAT3 sonic anemometer produced by Campbell Scientific [44], shown in use within the tunnel in figure 3.26, which can monitor the velocity in three directions. This anemometer allowed for data to be collected independently of the data acquisition PC at a rate of 60 Hz. Although, due to this independence, the velocity data could not be directly linked to power data from the turbine it allowed for a more detailed picture of the turbulence present in the wind facility and did not rely on the acquisition speed of the Keithley 2700 [42].

3.9.3 Rotational Speed

The rotational speed was monitored by the NI 6251 pci card [43] using it's built-in digital counter capabilities. The sensor used was the same sensor mounted to the

Figure 3.26: Sonic anemometer placed in tunnel air flow

low speed shaft which sent the trigger pulse to the PIV system. This sensor simply outputs an alternating high or low signal, determined by the excitation voltage and ground, which can be interpreted as a pulse. As there was only one metal tab connected to the low speed shaft this sensor will output one pulse per revolution. The counter was able to monitor this pulse and output the frequency in hertz which was then converted to revolutions per minute.

3.9.4 Voltage, Current and Power

The voltage coming from the grid and into the load bank from the generator was monitored directly by the Keithley 2700 multimeter system [42]. The current measurements, again at the motor and load bank inputs, were made by two shunt resistors. The shunt resistors were made of a small strip of metal, in this case a copper alloy, with a low resistance. This shunt resistor was placed in-line on the positive lead. As the shunt has a low resistance it will have a low voltage drop which is directly proportional to current flowing through it as given by Ohm's law found in equation 3.16. It typically has a low resistance in order to decrease the power which it dissipates, which is given by modifying Ohm's law to give equation 3.17. Additionally current sensors were mounted in the control box to detect the presence of current, by a hall effect sensor, in order to quickly identify electrical problems such as a blown fuse or broken connection.

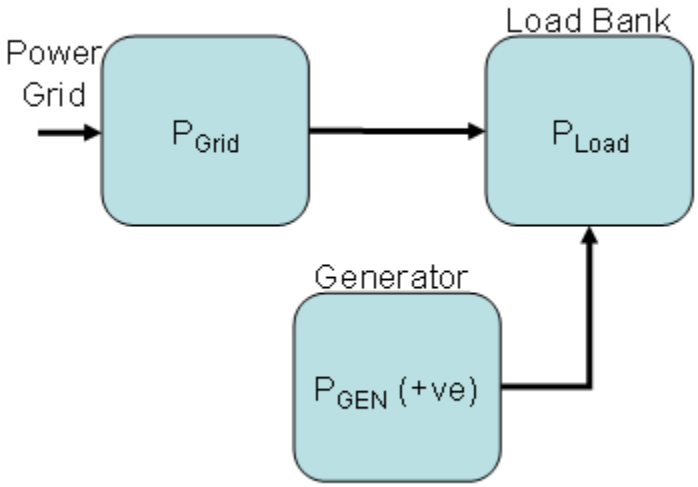

Figure 3.27: Power generation schematic

$$V = IR \tag{3.16}$$

$$P = VI = I^2R \tag{3.17}$$

Power was calculated using equation 3.17 from the two measured quantities at the grid and the load bank. As seen in electrical schematic from figure 3.24 the load bank and motor are both connected, in parallel, to the grid DC input. As such the load bank is always drawing current from the grid as it is essentially a resistor connected to a voltage source. In order to determine the amount of power that the motor was absorbing or producing the difference in power between the grid input and the load bank was determined as shown in equation 3.18. The power generated can be either positive, when generating power, or negative, when motoring. Figures 3.27 and 3.28 show the generation and motoring modes schematically.

$$\begin{aligned} P_{Load} &= P_{Grid} + P_{GEN} \\ P_{GEN} &= P_{Load} - P_{Grid} \end{aligned} \tag{3.18}$$

3.9.5 Labview [45]

Labview [45] was used to control the data acquisition hardware and to save the collected data into files to be analyzed with Excel. As the Keithley 2700 was an external system not manufactured by NI, who also produce Labview, the communication with it required more code and could not be accomplished, entirely, with built in virtual instruments. The NI 6251, however, was monitored with a built-in

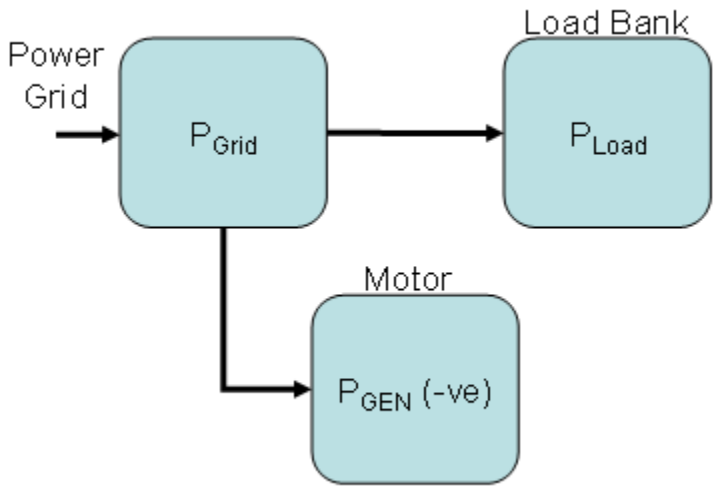

Figure 3.28: Motoring schematic

"data-acquisition assistant" which allowed for simple user inputs to determine what was to be monitored and which physical channels to connect the signal to.

In order to communicate with the Keithley 2700 it was connected to the data acquisition PC with a 15 pin serial cable which was able to carry the signal from the base of the tower to the control room. Within Labview the user specified: the physical channels that the signals were connected to on the Keithley 2700; the signal resolution required; and a title to identify each channel in the data file header.

A front end interface allowed the user to quickly see the various parameters being monitored by both sets of hardware in order to monitor the experiment on the go. The primary parameters shown were: the motor and load bank voltages and current; the calculated power at each point; and the low speed shaft rotational rate.

Chapter 4

Experimental Procedure

4.1 Performance Measurements

All performance measurements were taken using the electrical setup outlined in section 3.9.4. Both drivetrain loss and overall power production were measured as they were key measures for future work on this experimental apparatus. Drivetrain loss was important to quantify in order to estimate the power produced at the blades as opposed to the power measured at the generator. This relationship between the measured power and the estimated power produced at the blades is found in equation 4.1. Ideally the blade power would be determined using a torque and speed sensor at the point the blades connect to the drivetrain, instead of electrical measurements at the generator, but this method was not feasible with the available materials and test rig design.

$$P_{GEN} = P_{Aero} + P_{Drive} + P_{Blade} \tag{4.1}$$

4.1.1 Drivetrain Loss Estimation

The procedure to estimate the overall power losses from rotating the blades was completed after all performance measurements were completed on every testing day. This procedure was completed daily in order to compensate for mechanical differences due to part wear or environmental differences due to pressure or temperature changes, which may affect the results.

The first step in this procedure was to ensure that the large doors at both ends of the wind facility, surrounding the test section, were closed. This was done to ensure that there would be no air movement, other than self-generated, around the test apparatus. The blades were then rotated from 40 rpm to 220 rpm in 10 rpm increments being allowed to attain a steady state, based on power measurements, at each speed setting. As there was no wind energy input to the wind turbine, power must be drawn from the grid in order to rotate the blades. This procedure

measured the power loss due to aerodynamic effects and drivetrain losses, as shown in equation 5.1.

$$P_{GEN(nowind)} = P_{Aero} + P_{Drive} \tag{4.2}$$

The same test outlined above was completed with the blades removed from the apparatus. This test was done in an attempt to measure the losses due only to the drivetrain, P_{Drive}, as shown in equation 4.3. This particular test was only completed once due to the time required to remove and reinstall the blades from the apparatus; the results were therefore presented as a percentage difference from the losses found with the blades attached due to the day to day environmental changes.

$$P_{GEN(noblade)} = P_{Drive} \tag{4.3}$$

The aerodynamic losses, due to the blade rotation, could also be quantified by combining the results found with and without the blades attached. Equation 4.4, derived from equation 4.1, demonstrates that, with no power produced at the blades, aerodynamic drag losses can also be found as the difference of the power measured at the motor and the drivetrain losses. The results of this testing can be found in section 5.1.2.

$$P_{Aero} = P_{GEN(nowind)} - P_{Drive} \tag{4.4}$$

4.1.2 Power Production

The power production measurements were found over a wide range of TSRs but since the TSR was a function of both wind speed and rotational rate there are numerous combinations of each which can result in the same TSR. Ultimately the number of combinations was limited due to: the wind speed limitations of the facility; the mechanical limitations of the apparatus; and the instrumentation limits of the speed sensor. The wind speed was limited to a mean value of approximately 11 m/s, the rotational speed was limited to 220 rpm before mechanical vibrations became excessive and the speed sensor could not accurately determine speeds below 40 rpm. Wind speeds below 6.4 m/s, while tested, were largely ignored as the results contained an unacceptable level of inconsistency, likely due to the data acquisition limitations, as shown in the raw power curves from experiments at 3.5 m/s and 6.4 m/s in figure 4.1. Low C_P values at high TSRs in this figure are likely due to erroneous rotational rate data artificially increasing the TSR, in the final results many of these outliers were removed using statistical criteria.

The general procedure for power measurements was to set a common fan speed for all six fans which would result in a relatively constant wind speed across the rotor plane. As the fans were variable frequency drives, which were adjustable from 0 to 60 Hz, the wind speed was changed in 5 Hz increments over this range. At

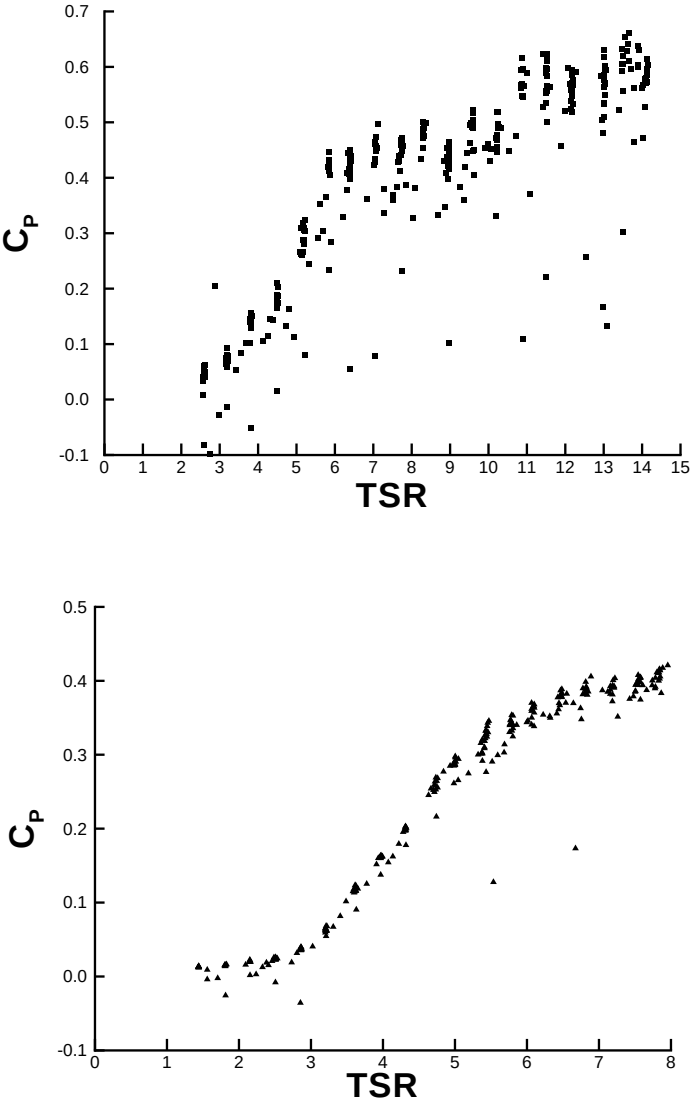

Figure 4.1: Raw power curve for data collected at U_∞ =3.5 m/s (above) and $U_\infty = 6.4$ m/s, demonstrating high levels of variability at low velocities

each wind speed setting the rotational speed was changed from 40 rpm to 220 rpm in 10 rpm increments, as in the loss estimation procedure. This method resulted in a higher density of data at lower TSR values due the rotational rate limitation of 220 rpm. This meant that as the wind speed was increased the TSR range was decreased so that a common TSR range at all wind speeds was not achievable. As an example of this: at a rotational rate of 220 rpm and at wind speeds of 5 m/s and 10 m/s the respective TSRs for this apparatus were 10 and 5. In this example in order to achieve a TSR of 10 at a wind speed of 10 m/s the rotational rate would need to be 440 rpm. This problem can only be solved by fundamentally changing the mechanical design of the apparatus and balancing of the blades in order to minimize mechanical vibrations.

4.2 Experimental PIV Procedure

Due to the experimental nature of PIV an involved process, discussed below, is required in order to achieve acceptable results. The first step of this process involved determining an area of interest in the flow which will be measured. A laser was then aligned to produce a light sheet to illuminate the area of interest. A camera was then placed perpendicular to the illuminated area of interest. The flow was then seeded with an appropriate level of smoke. A point in the blades rotation was also selected to correspond to the camera and laser positioning while also considering flow effects from the ground and surrounding structures. With the physical setup complete the timing of the image acquisition was selected through a trial and error process. A correlation of the images was then made to determine the velocity field within the area of interest and validation of the data was completed to remove erroneous data. Due to movement of the blade within the area of interest during testing, for reasons discussed in section 4.3, post-processing of the images was required to shift the PIV results to a common reference.

4.2.1 Area of Interest

The area of interest refers to the area within the experimental setup which has the flow conditions which are being investigated in a particular test. For this experiment the suction, or lift, side of one of the blades was examined at approximately 90% of the tip radius. This side of the blade was selected due to the stall effects that could be present on the suction side that are not typically present on the pressure side of a blade. This area was not ideal as there is a potential for tip effects, discussed in the BEM results in section 5.2.3, which could introduce complex flow patterns. This, however, could not be avoided due to the limitations of the camera and lens available.

The maximum dimensions of the area being imaged as well as its distance from the tip were limited by the resolution of the camera, the available lens and distance

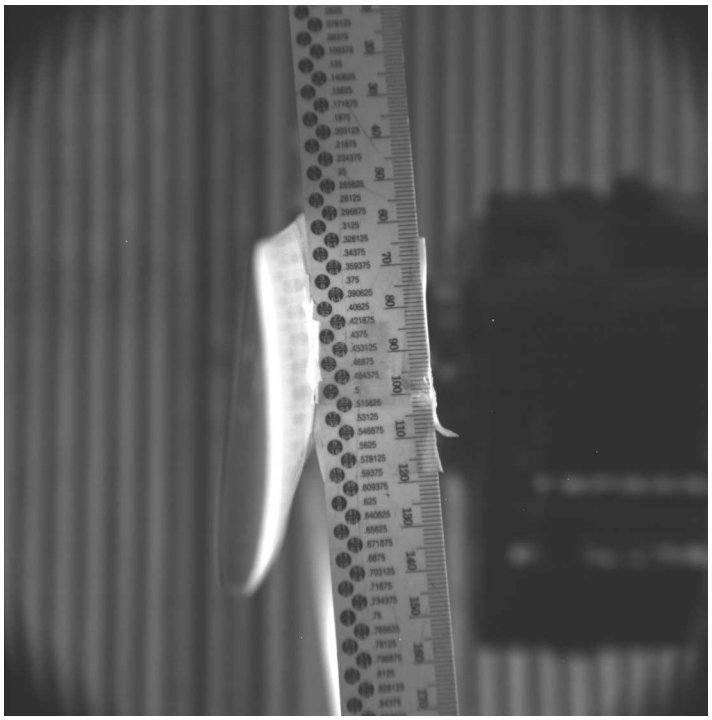

Figure 4.2: Calibration image, with a ruler in the frame, used to focus the camera and determine image scale

from the camera to the tip of the blade to avoid physical contact. The camera lens was ultimately placed approximately 10 cm from the tip of the blade which allowed an area of 16 cm square to be imaged approximately 21 cm inboard from the tip of the blade.

4.2.2 Focus and Alignment

The focus and alignment process involved both the camera and the laser. The laser sheet was illuminating the area of interest and would be the focal plane on which the camera would image. The camera was placed perpendicular to the laser sheet in order to avoid the need to apply corrections to the data in post processing which could introduce error.

Initially a ruler with crisp markings was placed on the blade at the point which was being imaged, as shown in figure 4.2. The blade was also placed, statically, at the point in its rotation where the images would be taken. The ruler served two purposes: first, the crisp markings allow the focus to be determined easily; second, the ratio of physical distance to CCD pixels, image scale, would need to be determined for velocity calculations and could be calculated using this test image.

With the camera focused on the area of interest the laser is fired at a low power to ensure that the laser sheet is projected at the correct position along the blade. Adjustments can be made to the laser sheet width using optics attached to the laser

head. The laser sheet width used was on the order of 1 to 3 mm in order to capture acceptable images. With any complex flow there could be flow in and out of the laser plane so a trial and error process to adjust the laser width must be used to increase the accuracy of the results.

4.2.3 Seeding

Seeding the incoming flow with water based smoke was required to allow particles to be visualized within the flow field. As previously discussed, in section 2.3.1, the challenge with the seeding process was to create a smoke stream with a particle density which would not over or under expose the images. Numerous iterations were completed using a variety of smoke generators and injection manifolds which are outlined in sections 3.7.4 and in appendix E. With the smoke apparatus selected, the smoke outlet position was found using a trial and error process, to optimize image quality, and was adjusted whenever the wind speed or rotational rate was changed.

With the fan and the rotational speed set the smoke was observed to ensure that it was traveling within the area of interest with adjustments in height and location made if required. Once the smoke was traveling in the area of interest test images were captured with the laser firing at approximately 90% of full power. These images were evaluated for the strength of the PIV correlations, based on the number of rejected vectors. Additionally, the raw images were subjectively evaluated for exposure levels in the regions containing smoke particles. If the correlations were strong, again based on the number of rejected vectors, then the setup was used for the remainder of the images collected for the particular test case. If the images were over-exposed either the power of the laser could be reduced or the smoke being produced could be reduced. Typically the ideal setting would require a combination of both laser power adjustments and smoke density; but laser power was inherently easier to adjust and was the preferred method for exposure correction.

4.2.4 Trigger Timing

Triggering of the PIV equipment, for this particular experiment, was required in order to capture images at a certain point within the blade rotation. This was accomplished by generating a trigger pulse using a metal tab on the low speed shaft which passed through an optical sensor. This sensor was a light detector with an LED source which would output a TTL signal if the path between the detector and source was blocked. Initially this signal was not registered by the control system possibly due to it's relatively long rise time. The other drawback was that the metal tab on the shaft needed to be physically moved in order to adjust the point in rotation that the images were captured. To provide the PIV system with an adjustable input pulse which it would recognize a signal generator was placed in-line between the sensor output and the controller input. This signal

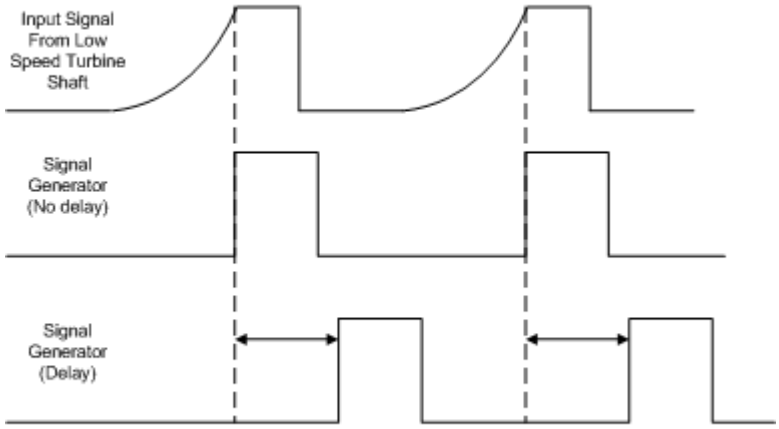

Figure 4.3: Pulse schematic

generator produced a pulse output with nanosecond rise time and also allowed for a delay to be placed between the time it received a signal from the sensor and when it output a signal to the controller. Thus by adjusting the delay in the output the rotational position when the image was captured could be finely adjusted. This process is shown in the schematic in figure 4.3.

With the triggering system, outlined above, the rotational location of the blade when the images were captured was held constant. As the rotational speed was changed the signal generator delay was adjusted to compensate for the distance the blade will travel in the time between receiving a signal and the camera and laser firing. Since there was a shadow in the frame on the pressure side, due to the laser sheet optic location, the blade was intentionally placed in the left third of the frame. Vertically the blade was centred in the frame to capture both leading and trailing edge phenomenon.

The settings on the signal generator, which affect the pulse width and pulse delay, were adjusted to position the blade in the same place within the frame at each rotational rate. The settings for various rotational speeds can be found in table 4.1 with a plot of these results found in figure 4.4 with the 111 rpm data removed as it was at a different range setting. For data with the range of 167.5 rpm and 220 rpm, when the range setting was constant at 5 msec, a linear curve fit can be used to estimate the required setting for further testing. This estimate, equation 4.5, could be used to reduce the time required to achieve the correct trigger timing.

$$multiplier = 0.0066 \times \Omega + 0.0046 \tag{4.5}$$

Table 4.1: Signal Generator settings for PIV

Speed (RPM)	Multiplier	Range (msec)
111	1.450	50.0
167.5	1.100	5.0
180	1.200	5.0
195	1.300	5.0
220	1.450	5.0

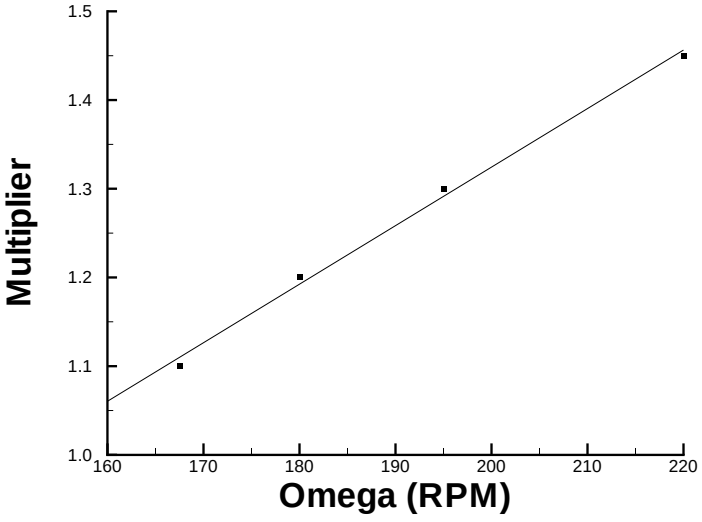

Figure 4.4: Signal Generator settings for PIV

Table 4.2: Theoretical and experimental interframe rates

$Fan\,Speed$ (Hz)	$Velocity$ (m/s)	$Max\,Theo.\,Rate$ (μs)	$Exp.\,Rate$ (μs)
35	6.4	200	75
45	8.4	152	60
60	11.1	115	40

4.2.5 Interframe Rate

The user specified the inter-frame timing which refers to the time between the two frames, or image pairs, which are captured in each burst. The exact time between frames must be known in order to convert the distance a particle cloud travels to a velocity. The total number of image pairs to be captured can also be specified by the user.

The theoretical interframe rate was calculated for all wind speed and rotational speeds which would be used in testing. Based on theory the maximum interframe rate would allow a particle to move 8 pixels, 25% of the interrogation area width, from the first to the second frame [21]. With the pixels per metre and overall camera resolution known from the final focus image taken previously the maximum interframe rate could be found using equation 4.6 from section 3.7.2. In practice the experimental interframe rate was far below the recommended maximum value and was found through trial and error until acceptable correlations were found for each test case. The resulting maximum theoretical and experimental frame rates used can be found in table 4.2.

$$t_{max} = \frac{0.00128}{U_\infty} \tag{4.6}$$

Additionally, the time which will elapse between bursts can be specified. This value can either be a minimum time or based on a set number of trigger pulses. Alternatively the user can also specify the system to capture images as fast as possible which then limits the time between bursts to the physical capabilities of the camera and laser. Although the system literature [41, 23] states that the camera and laser are capable of capturing images at 15 Hz; experimentation found that the acquisition rate, on average, was between 1 Hz and 0.5 Hz. This discrepancy is likely due to the time the system requires to transfer the image data from the camera, through the processor and into the user's computer.

4.2.6 Image Correlation

The Flow Manager software was able to take the images captured during each test and perform the cross-correlation on the image pair to produce a velocity vector

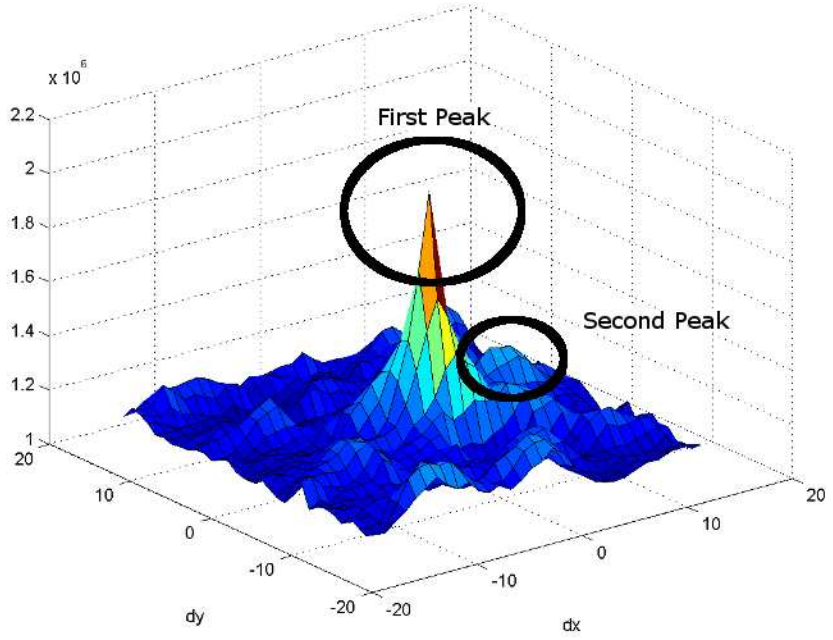

Figure 4.5: Sample correlation surface plot

map. The user then selected the interrogation area size and the overlap of these areas. For the tests completed a 32 by 32 pixel interrogation area was selected with 50% overlap. This resulted in the image being divided into 3844 interrogation areas for the cross-correlation process.

After each image pair had been processed the raw vector maps were then validated using two methods: magnitude and peak to peak ratio. These validations would remove erroneous velocity vectors which could be produced due to a lack of smoke particles or image exposure problems in certain regions within the images.

The magnitude validation parameter which removed vectors with a magnitude greater than a user selected threshold, was selected to be 30 m/s for all tests as this velocity was deemed to exceed any reasonable experimental velocity magnitude. Finally, the peak to peak ratio referred to the ratio of the heights of the first and second correlation peaks produced. This validation step removed data if the highest peak was not a user defined multiple of the height of the second peak. In all tests this value was set to the highest allowable value of 2 in order to remove all but the strongest correlations. A sample of a correlation surface plot indicating the first and second peak is shown in figure 4.5 for reference.

Although high rejection criteria did remove a substantial number of vectors from each image correlation; the goal was, over 1000 images, to produce an accurate representation of the flow when all the images were averaged. Since the averaged velocity vector did not use rejected data the sample size of each point was different and could be used as a measure of the confidence of the data in a given region.

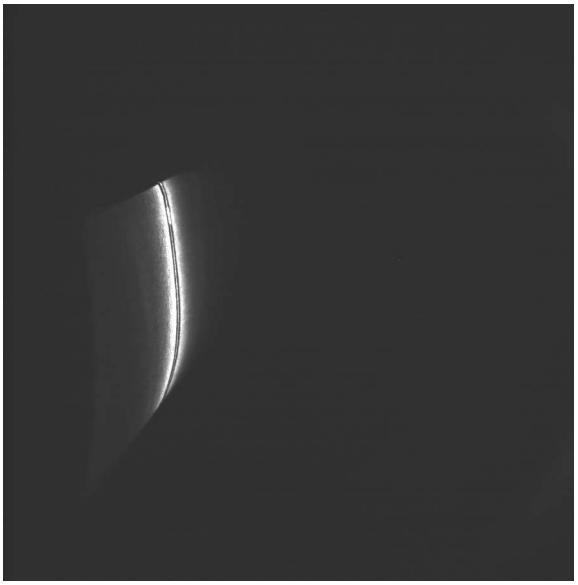

Figure 4.6: Master image used to determine the shift vector for each raw image pair

4.3 PIV Post-Processing Technique

4.3.1 Concept

Due to movement of the blade within the area of interest during testing, likely due to observed vibrations in the blades and turbine structure in addition to wind speed fluctuations, post-processing of the images needed to be completed to shift the PIV velocity data to a common reference. The first step of the post-processing was to extract the image pairs and their correlations from the Flow Manager program. Using a custom program written using Matlab [17], shown in appendix F.1, the first image of each pair was correlated to a master image, depicted in figure 4.6. This master image was of the blade in the ideal position with no smoke particles in the flow and was taken from the timing images captured during the calibration phase. The correlation of the two images would produce a "shift" vector which would indicate how many pixels the image would need to be shifted in the x and y direction in order to align with the master image, conceptually shown in figure 4.7. The orientation of the camera results in the x axis being in the free stream flow direction and the y axis tangential to the blade rotation. This shifting in the x axis position of the blade was the results of aerodynamic effects and mechanical vibrations which combined to cause the blade to "flutter" in the x direction. Shift in the y axis position was likely due to signal error from the trigger output placed on the low speed turbine shaft. This correlation process was then completed for all of the images from a specific test case.

The maximum and minimum shifts, in the x and y direction, for all collected images from a test case was then calculated. These values determined the area

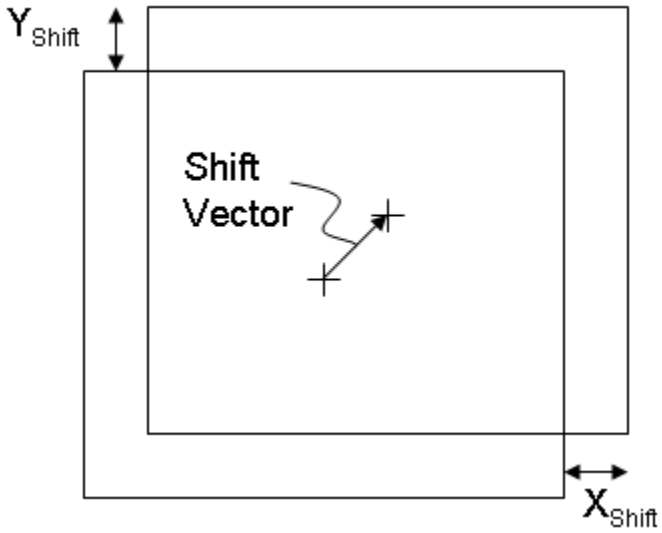

Figure 4.7: Shift vector concept

that was common in all images. This concept is shown in figure 4.8 with the cross-hatched area representing the common overlap area. The cross-hatched area would later be used to crop the PIV data for averaging. In order to limit the loss of PIV data from images that were closely aligned with the master image, during the cropping process, two criteria were implemented to removed data. The first criterion was based on Chauvenet's criterion [46] which rejected data with x or y shifts that exceeded limits based on the mean, standard deviation and sample size. The second criterion removed data with a calculated shift in the x or y direction of more than 100 pixels. Both of these methods were applied in order to increase the common area of the results. A sample of a shifted image is shown in figure 4.9, this particular image was shifted 26 pixels in the negative x direction and 50 pixels in the negative y direction.

With the shift vector for each image pair determined, the PIV data from Flow Manager could be shifted to match. However, this presented a problem as the PIV correlation vectors are stored for each interrogation area, which were each 32 pixels square, and the shift results were calculated in pixels. Due to the 50% interrogation area overlap, defined by the user, each vector represented an area 16 pixels in width. The calculated shift in pixels for each direction was therefore divided by 16 and the results was rounded to the nearest integer; this value represented the number of interrogation areas to move the vector prior to averaging. For example if the shift was calculated to be 36 pixels in the X direction and 57 in the Y direction the velocity vector would get moved 2 interrogation areas to the right and 4 areas up prior to averaging. This rounding could introduce more error but with an interrogation area every 16 pixels the maximum rounding error will be 8 pixels which represents approximately 1 mm. this was deemed acceptable in order to avoid the added complexity that interpolation would have added.

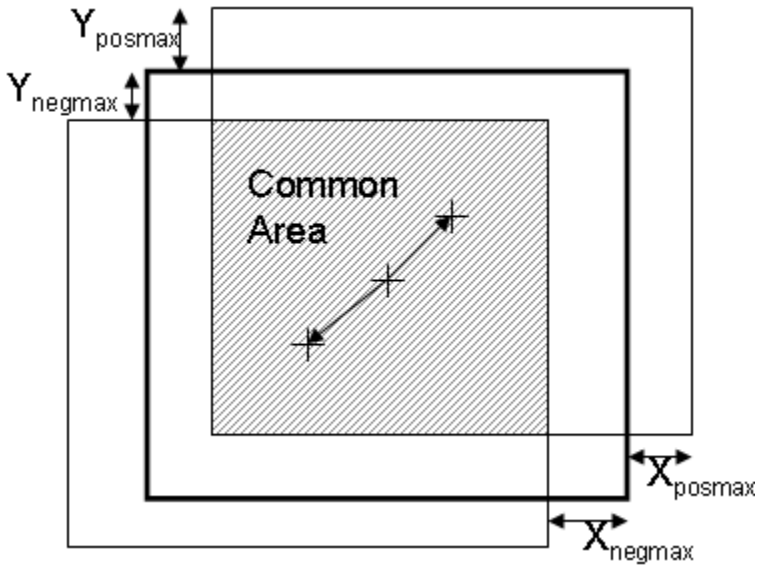

Figure 4.8: Common area found after determining the shift vector for all images within a test case

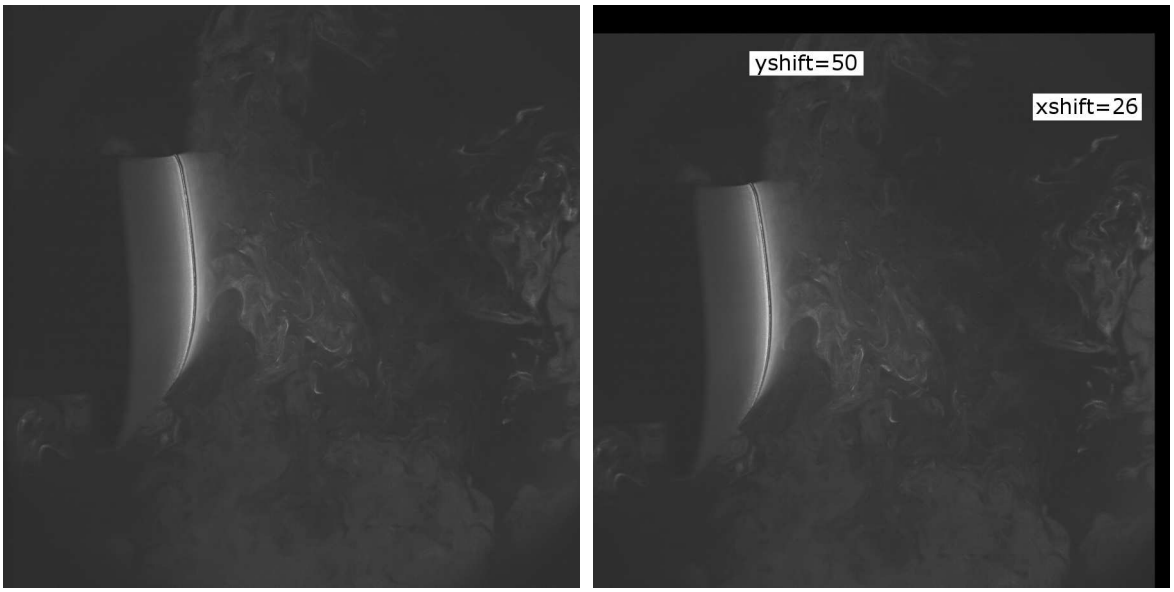

Figure 4.9: Shifted image, before (left) and after (right)

The rounded shift vector was then applied to the raw PIV data which theoretically resulted in with multiple sets of velocity data which were spatial aligned. The aligned PIV velocity vectors were then averaged to produce an overall velocity map representative of the flow over the blade in each test case. The results of this averaging can be found in section 5.3.

4.3.2 Image Shift Program Verification

Prior to the application of the image shift program on all collected images and their correlations the program was first verified against a manual determination of the required shift. The manual method required loading the master image and ten sample images into a image editing program and manually reading coordinates of a common point on the trailing edge of the blade within the image each image. The images used were from tests at the highest free stream velocity of 11.8 m/s and a rotational rate of 198 rpm which were expected to represent the most variability in the blades position due to the higher loading on the turbine.

The difference between the master image coordinates and the ten sample PIV image coordinates can be found in table 4.3 with the values determined numerically by the image shift program and also manually. This table also indicates the average number of pixels that the images in this sample data set needed to be shifted in order to match the master image. As previously discussed some shift values calculated by the image shift program that exceeded the rejection criteria were removed from consideration as they represented a shift that was deemed excessive and likely due to erroneous data. Rejected images in some data sets amounted to approximately 30% of the original data set based on this criteria while in other data sets the rejection was as low as 0.2% with the amount of rejected data independent of the flow conditions. Specifically in images 1 and 5, although the blade's position could be determined manually it could be seen that the tip of the blade was flexing enough to block most of the laser light from reaching the camera and thus a strong numerical correlation would be hard to achieve. These two images would be rejected by the program based on the erroneous calculated shift values.

Excluding the rejected values the average difference in shift values between the manual and numerical methods was found to be approximately 8.5% in the X and Y directions which in absolute terms represents 1 mm in the X direction and 0.3 mm in the Y direction. While there was a discrepancy between the manual method and the numerical approach this was deemed acceptable when also considering the shorter time required to process images and the volume of images to be processed.

4.3.3 Experimental Image Processing

The results presented in this section attempt to show the progression from raw experimental PIV images through to velocity vector maps of the flow over the blades. During testing approximately 1000 images at each operational state were

Table 4.3: Comparison of manual shift determination and Matlab [17] image shift program

Image	$Manual_X$ $(pixels)$	$Manual_Y$ $(pixels)$	$Matlab_X$ $(pixels)$	$Matlab_Y$ $(pixels)$
0	25	54	26	50
1	83	33	117	132
2	66	29	70	30
3	67	35	74	41
4	72	33	81	38
5	87	31	-444	125
6	54	30	59	32
7	58	42	64	43
8	71	34	79	39
9	65	36	69	36
Average	65	36	65	39

collected for each data set. Capturing 1000 raw images at each operational state was necessary in order to account for the data loss associated with unseeded portions of each image because evenly distributed seeding across the area of interest was not possible, as previously discussed in section 3.7.4. Figure 4.10 shows two images which represent a well seeded image and a poorly seeded image. Also of note in the raw images was the camera aperture cutting light at the four corners of the image which produced spurious data in all subsequent calculation in these regions.

The contour plot in figure 4.11 demonstrates the areas for these two images which produced accepted vectors, in blue, which would be used later in the averaging process. It is important to note that the image with particles throughout the imaging area still does not produce acceptable vectors in all areas. Finally, figure 4.12 demonstrates the final vector plots from each image, with the rejected vectors removed, that would be used later in the averaging process.

4.4 Test Case Selection

In order to select the specific test cases, combinations of wind and rotational speed, the limitations of the wind facility, turbine apparatus and PIV equipment needed to be accounted for. As there were two distinct experiments being completed, power production measurements and PIV measurements, the test cases for both were different due to the specific goals of each.

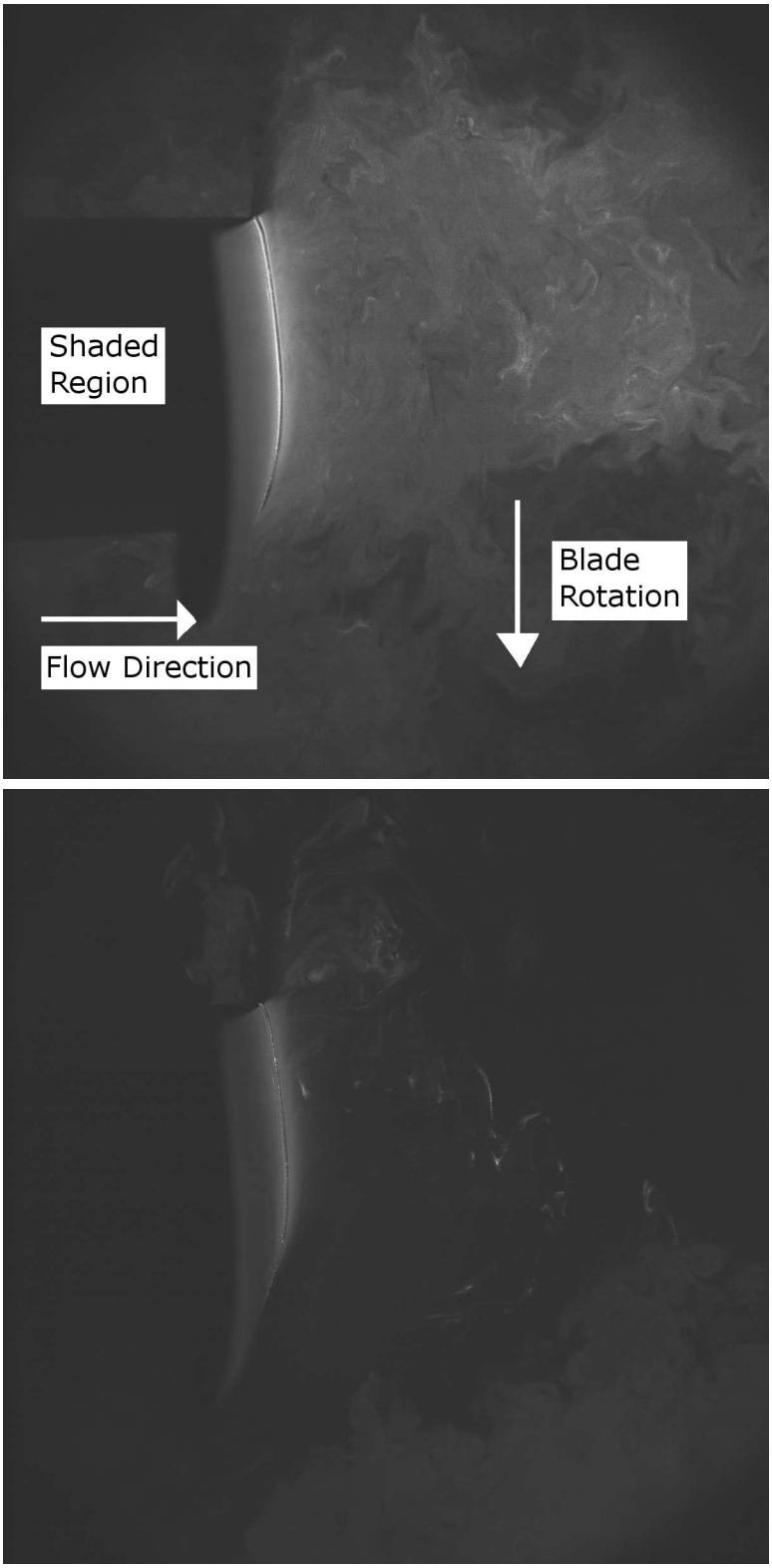

Figure 4.10: Raw images used in PIV analysis with the well seeded image shown above, TSR 3.8, $\Omega = 198$RPM, $U_\infty = 11.8$m/s

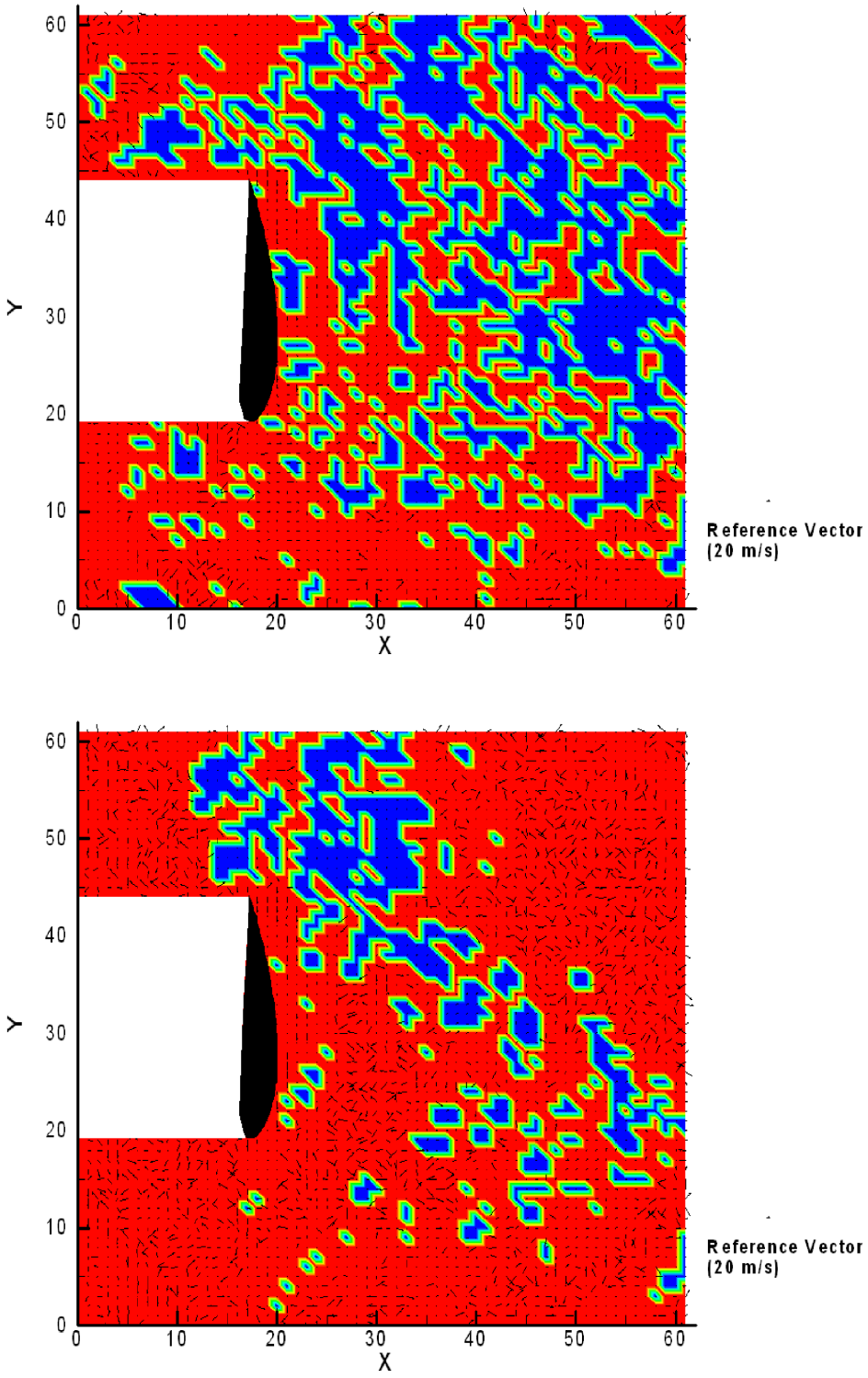

Figure 4.11: Contour plots showing accepted vectors in blue for each of the raw image correlations, TSR 3.8, $\Omega = 198$ RPM, $U_\infty = 11.8$m/s (well seeded above)

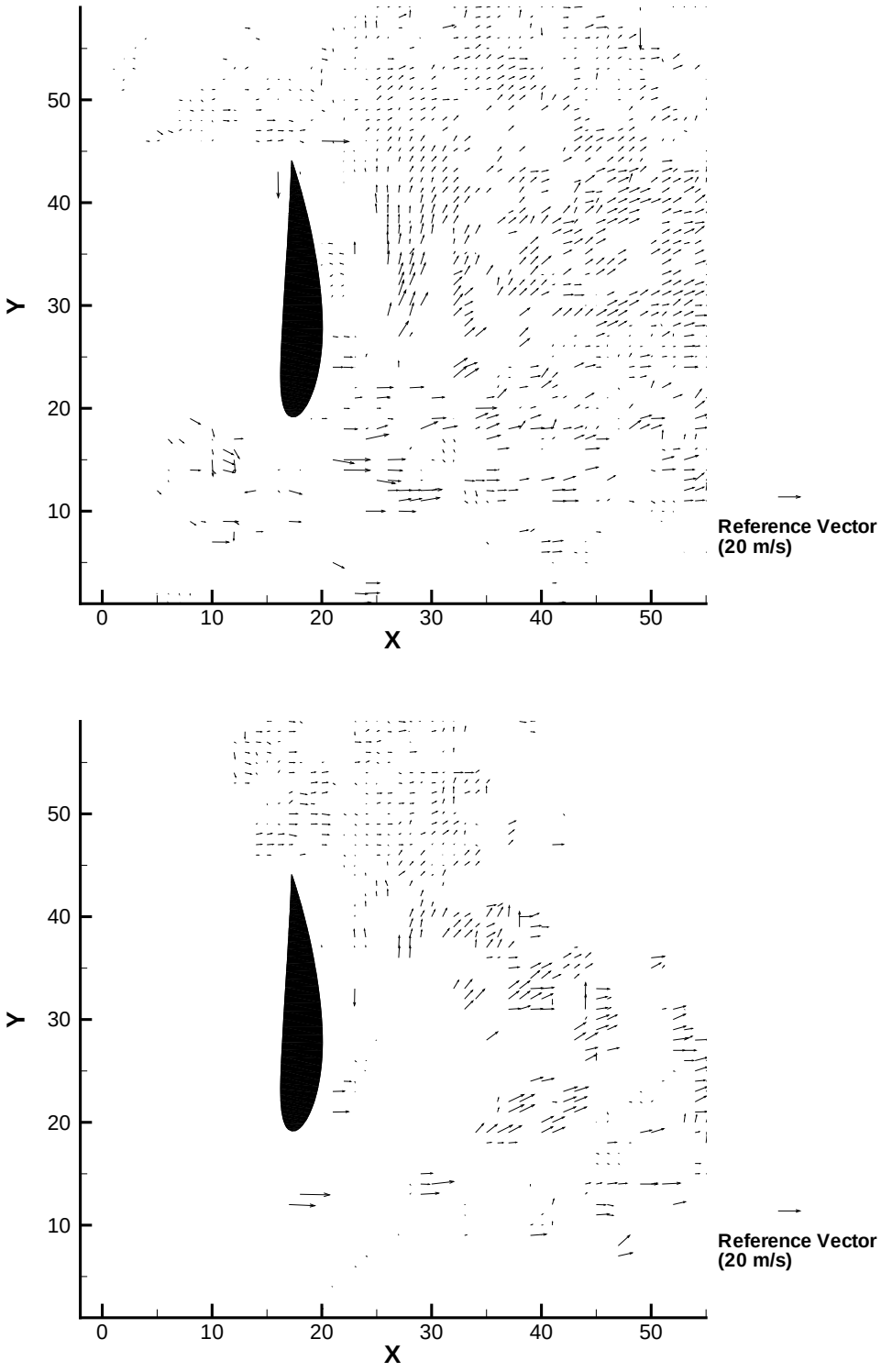

Figure 4.12: Vector plots from individual image pairs, TSR 3.8, $\Omega = 198$ RPM, $U_\infty = 11.8$m/s (well seeded above)

Table 4.4: Five test cases used in PIV experimentation

Test number	Omega (RPM)	V (m/s)	TSR
1	195.0	11.0	4
2	111.0	6.4	4
3	167.5	6.4	6
4	220.0	6.4	8
5	220.0	7.5	6

4.4.1 Performance Testing

As stated previously the wind facility, in it's current configuration, was limited to a maximum wind speed of 11 m/s. Although, based on the testing results, speeds below 6.4 m/s did not produce usable power data using the current data acquisition system, data was still collected down to 0.5 m/s or 5 Hz on the fan settings. The turbine apparatus could not be rotated beyond 220 rpm and the acquisition system could not reliably measure the speed below 40 rpm. These values limited the theoretical range of TSR to between 2.5 and 13.5 for the lowest wind speed and 0.8 and 4.5 for the highest wind speed. Ultimately six wind velocities were chosen, nominally between 6.4 m/s and 11 m/s, which would be used in the power production experiments to produce C_P vs TSR plots.

4.4.2 PIV Testing

For the PIV portion of the experiment time limitations, due to the time required to setup individual tests, and the mechanical limitations of the apparatus, limiting rotational speed, affected the number of tests which could be completed. There were two goals in the PIV portion of the testing: compare the effect of changing the TSR value on the flow characteristics; and maintaining a constant TSR while changing the wind and rotational speed combination. Five test cases were selected which represented four different rotational rates, three different wind speeds and three TSRs. These five different test cases were each completed on two separate days to attempt to demonstrate repeatability of the results. Table 4.4 demonstrates the five test cases selected and their respective rotational speed, wind speed and resultant TSR.

Chapter 5

Results

5.1 Experimental Performance

Based on power generation experiments conducted in the wind facility with the turbine apparatus over a range of wind speeds, 6.4 m/s to 11 m/s, and rotational rates, 40 RPM to 220 RPM, outlined previously, the experimental performance of the blades could be evaluated. Drivetrain and aerodynamic power losses were first quantified before blade power production could be evaluated.

5.1.1 Outliers

Data pertaining to the drivetrain loss section, 5.1.2, had outlier data points, within a data set, removed using Chauvenet's criterion as suggested by Holman [46]. Since the measured RPM was transient each data set was taken as the nominal rotational speed +/- 5 rpm; for example, at a nominal rotational speed of 130 rpm, data from 125 to 135 was considered part of the same data set. Chauvenet's criterion states that the probability of a reading, within a data set, based on a normal distribution, occurring must be greater than $1/2N_S$ where N_S is the number of readings in the data set. This criteria was used to eliminate both outlying power and rotational rate data.

The outlier analysis was not completed for all of the blade power generation data due to the shear volume of data present; however, the results from the 11 m/s flow condition were analyzed in order to determine representative error values for power generation data. The outlier analysis resulted in 4.5% of the data being removed from the data or 28 data points. A detailed error analysis for this data set is outlined in appendix B.

5.1.2 Power Losses

The drivetrain losses were estimated in two parts, as discussed previously in section 4.1.1. Initially the blades were connected to the drivetrain and rotated with no wind blowing over them. These results would therefore include some power loss due to the drag on the blades. An example of the data collected during the tests with the blades attached without wind can be found in figure 5.1, labeled $P_{GEN(nowind)}$.

The second part of the loss tests involved running the motor without the blades attached to eliminated the aerodynamic drag losses. This data was used to quantify the losses due solely to the drivetrain which includes: bearings, belts and the brake system drag. The data collected using this method is presented in figure 5.1, labeled P_{Drive}.

In order to relate the losses measured with the blades attached to the losses measured when the blades were detached, curve fits were applied to both data sets. The data collected with the blades attached was found to be represented by equation 5.1. A linear curve fit was found to fit the data collected without the blades attached and is found in equation 5.2. The fit to the data with the blades attached was not expected as aerodynamic drag theory would have suggested a third order dependency on velocity, or rotational rate, as shown in equation 5.3. However, the linear fit was expected as rotating objects, under an assumed constant torque due to friction, undergo linear power loss due to a torque and speed relationship, as found in equation 5.4.

$$P_{GEN(nowind)} = -0.0034\Omega^2 - 3.2692\Omega \tag{5.1}$$

$$P_{Drive} = -2.967\Omega \tag{5.2}$$

$$F_D = \tfrac{1}{2} C_D \rho U_\infty^2 A$$

$$P = F_D U_\infty \tag{5.3}$$

$$\therefore P_{Aerotheory} = \tfrac{1}{2} C_D \rho U_\infty^3 A$$

$$P_{Drivetheory} = T\omega \tag{5.4}$$

Based on the curve fits for the overall power loss and the drivetrain losses, equation 5.5 was developed for the aerodynamic losses. The aerodynamic loss is plotted against the overall power loss measured and the drivetrain losses in figure 5.1.

$$P_{Aero} = -0.0034\Omega^2 - 0.3022\Omega \tag{5.5}$$

As the testing without the blades attached was only completed once, a percentage change was calculated from the drivetrain loss data to the power loss measured

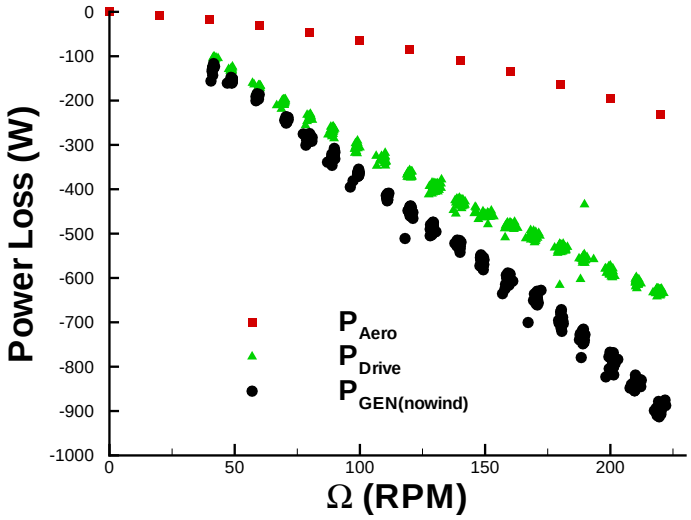

Figure 5.1: Overall power loss data

with the blades attached. This percentage change, calculated using equation 5.6, used the equations found above and was therefore related to the rotational speed. The data, based on curve fits, can be found in table 5.1 with the percentage change plotted against rotational speed found in figure 5.2. The resulting equation, derived from equation 5.6 and equation 5.7, was used to translate the data collected every testing day, with the blades attached, to an estimate of the drivetrain losses. The resulting translation can be found in equation 5.8.

$$Power\,Change = \left(\frac{P_{GEN(nowind)} - P_{Drive}}{P_{GEN(nowind)}}\right) \times 100\% \tag{5.6}$$

$$Power\,Change = 7.51 \times 10^{-4}\Omega + 0.1003 \tag{5.7}$$

$$P_{Drive} = P_{GEN(nowind)} \times \left(-7.51 \times 10^{-4}\Omega + 0.8997\right) \tag{5.8}$$

Ultimately two days were required to complete experimental testing and, as such, two different drivetrain losses translations were required. Based on equation 5.8 the data collected each day with the blades attached, under the no wind input condition, was translated to an estimate of the drivetrain loss. The estimated power that was absorbed by the drivetrain was added to the output power that was measured at the generator, during tests with wind input, in order to estimate the power that the blades were producing. For tests completed on the first day, wind speeds 0 m/s through to 9.2 m/s, the drivetrain power loss was estimated using equation 5.9. Testing completed on the second day, wind speeds 10.4 m/s and 11.1 m/s, used equation 5.10 to estimate the drivetrain power loss.

Table 5.1: Power loss data based on curve fits on the raw data

Ω(RPM)	$P_{GEN(nowind)}$ (W)	P_{Drive}(W)	Power Change (%)
0	0.0	0.0	N/A
20	-66.7	-59.3	11.1%
40	-136.2	-118.7	12.9%
60	-208.4	-178.0	14.6%
80	-283.3	-237.4	16.2%
100	-360.9	-296.7	17.8%
120	-441.3	-356.0	19.3%
140	-524.3	-415.4	20.8%
160	-610.1	-474.7	22.2%
180	-698.6	-534.1	23.6%
200	-789.8	-593.4	24.9%
220	-883.8	-652.7	26.1%

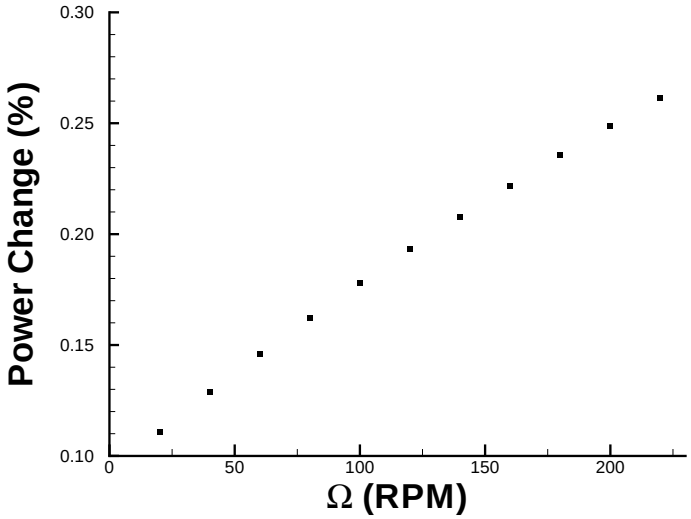

Figure 5.2: Difference between power measured with and without the blades attached as a function of the rotational speed

$$P_{Drive}(0 \leq U_x \leq 9.2) = -0.0027\Omega^2 - 2.1165\Omega \tag{5.9}$$

$$P_{Drive}(10.4 \leq U_x \leq 11.1) = -0.0027\Omega^2 - 1.8818\Omega \tag{5.10}$$

5.1.3 Power Generation

The power generated at the blades was of interest in order to compare the results given by the BEM program. Since the BEM program does not account for drivetrain losses estimating the power generated by the blades, as opposed to the values measured at the generator, was essential to make a meaningful comparison of aerodynamic data from this experiment.

A sample set of data collected during the experiment at two wind speeds, 7.3 m/s and 11.1 m/s, over a range of rotational rates is shown in figure 5.3. This figure demonstrates the increased power available at higher wind speeds and the plateau in power generation that occurs at higher rotational speeds characterized in the 7.3 m/s data set. This plateau is reached due to the coefficient of power plateau found at high tip speed ratios, which is discussed later in section 5.1.4. Due to it's lower maximum tip speed ratio the 11.1 m/s data set does not exhibit this plateau behaviour.

Blade power data for a constant rotational rate with varying wind speed demonstrates the cubic relationship between power and the incoming velocity at low free stream velocities, as shown in figure 5.4 for rotational rate of 220 rpm. The theoretical cubic relationship assumes that the coefficient of power is constant across the range of wind speed inputs and for this plot was assumed to be the peak C_P value for the experimental data which approaches 0.4. As the incoming velocity, U_∞, increases the tip speed ratio will decrease with a constant rotational rate which reduces the coefficient of power from it's peak. Due to the decrease in C_P with decreasing TSR, in the experimental data, the theoretical power output only matches until approximately 7.4 m/s. This helps to explain why many modern turbines, in addition to techniques such as variable blade pitch, operate with a variable rotational rate to maintain near peak C_P operation.

5.1.4 C_P vs TSR

The coefficient of power as a function of tip speed ratio is an important relationship to develop in order to determine the optimal rotational rate for peak power production at a given wind speed. Power measurements taken during wind facility testing were used to develop experimental results which could then be compared to the predictions by BEM theory.

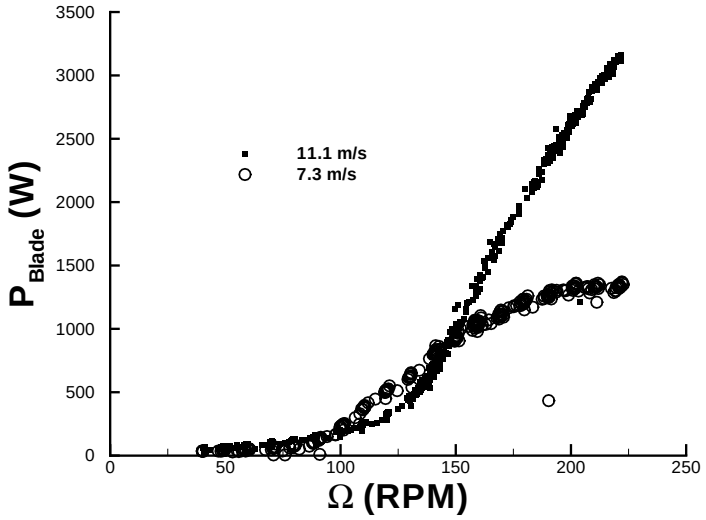

Figure 5.3: Power generated by the blades

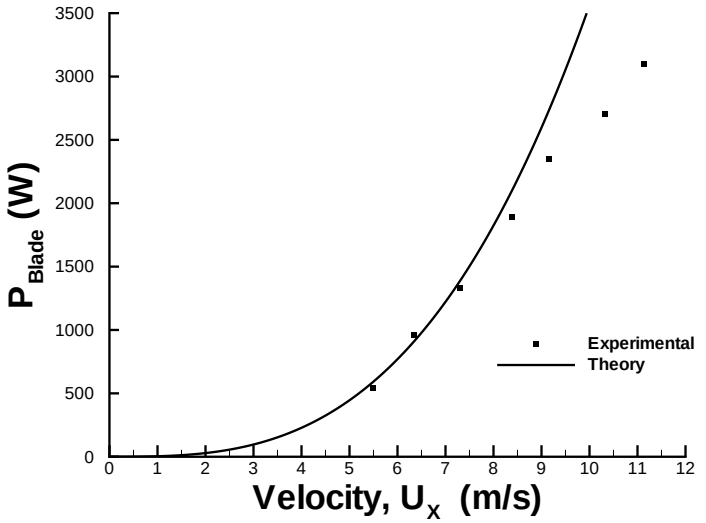

Figure 5.4: Power at the blades with varying wind speed, Ω= 220 rpm

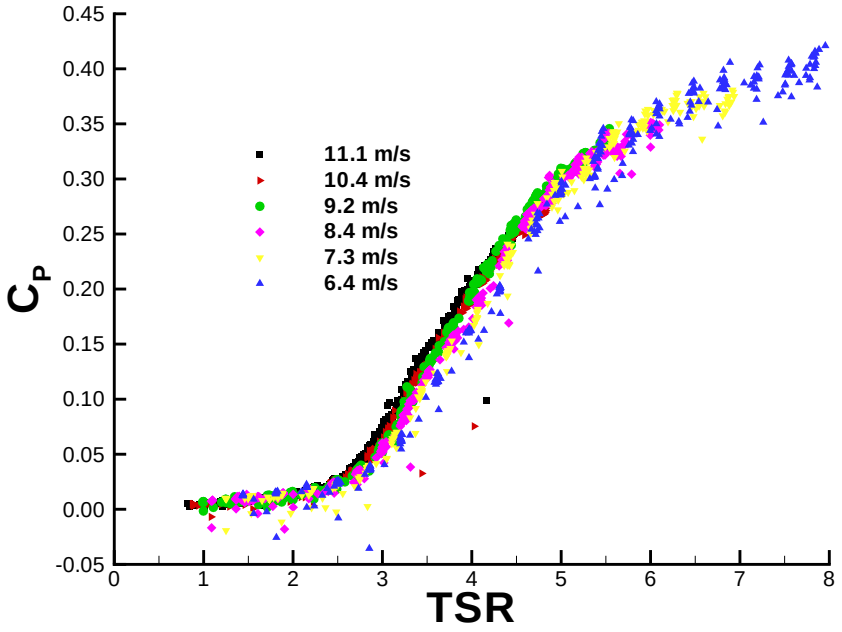

Figure 5.5: Raw experimental C_P results

5.1.4.1 Experimental data

With the power calculated previously the coefficient of power could be calculated over the range of TSRs found at each wind speed tested. The raw results, shown in figure 5.5, for the range of wind speeds between 6.4 m/s and 11.1 m/s and rotational rates between 40 rpm and 220 rpm collapse down onto one curve as expected. These raw results represent the individual data points collected during the tests, not the mean, and have only had five outliers removed, out of approximately 2400 total data points. The removed data points represented rotational rates far beyond physically possible results when compared with surrounding time series data points captured under the same conditions. Based on an error analysis of the 11 m/s and 6.4 m/s experimental data sets at a rotational rate of 220 rpm; a representative error for the coefficient of power, which included statistical variation and instrumentation bias error, was determined to be approximately 7%.

5.2 BEM Results

The results from the BEM code represent ideal conditions and can only provide theoretical values. However, BEM allows an analysis of the aerodynamic forces on the blades under a wide variety of flow conditions that might not be possible to achieve experimentally. Additionally, aerodynamic properties such as: angle of attack and axial or tangential induction factors can be theoretically determined at

Table 5.2: Effect of increasing the number of elements

Elem	Peak C_P	$Power$ (W)	Peak TSR	$T_{converge}$ (s)
10	0.3877	4590	9.4	4
50	0.3776	4470	9.2	14
100	0.3757	4450	9.2	26
110	0.3755	4450	9.2	29
150	0.3749	4440	9.2	38
200	0.3745	4440	9.2	51

different points along the blade which are also difficult to quantify experimentally. Prior to these analyses the effect of the number of elements used in the code was first completed as well as a study which determined an appropriate convergence criteria based on the axial induction factor.

5.2.1 Effect of the number of elements

The number of discrete elements, which divide the blade radially, used in the BEM analysis was determined prior to any final results being produced. The number of evenly spaced elements was increased until convergence, based on the C_P, was reached. Table 5.2 shows the effect of changing the number of elements on the C_P, tip speed ratio and the power produced. Although table 5.2 represents C_P with four significant digits this is only shown to demonstrate the small changes which were calculated with the program as this level of accuracy could not be achieved in experimental results. This analysis was completed for a three bladed configuration using the *Abbot Original* lift and drag parameters from the manufactured blades and a constant wind speed of 11.0 m/s as the input. At a value of 110 elements the C_P changed by 0.05% from the previous value at 100 elements. In all further analysis the blades were divided into 110 elements. The effects of increasing the elements is also shown in figure 5.6 with only the maximum C_P shown, as the power generated changes at the same rate as the C_P. The time required to run the BEM program was also monitored as this could have been a criterion in selecting the number of elements to be used.

5.2.2 Axial Induction Convergence Study

A study was completed to determine the percentage change in axial induction factor, between iterations, which would be used in the BEM analysis to signify convergence for each element. This minimum percentage change was altered from 10% to 0.1% and the effect on the C_P is tabulated in table 5.3. The table shows the criterion used, the overall C_P and the change in C_P from the previous criterion used. It was found that when the criterion was changed from 10% to 0.1% only a 0.25% change

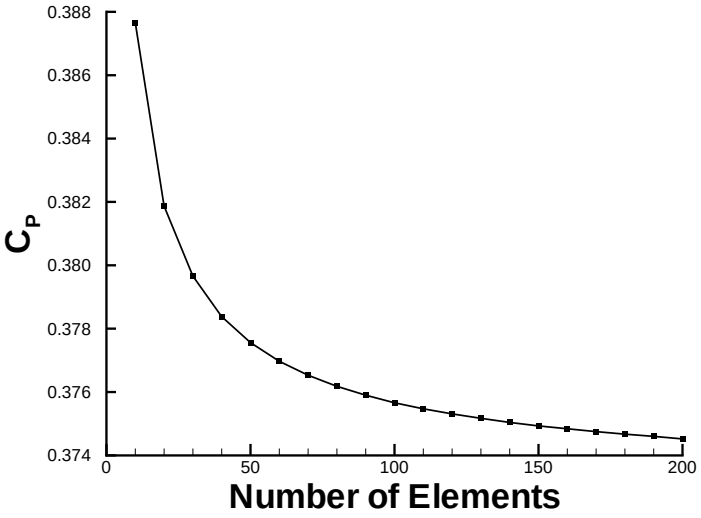

Figure 5.6: The effect of the number of elements used in the BEM analysis on the C_P

Table 5.3: Convergence study

Converge Criteria	C_P	Change C_P
10.00%	0.3745	N/A
5.00%	0.3750	0.128%
1.00%	0.3754	0.099%
0.50%	0.3755	0.024%
0.10%	0.3755	0.003%

in the C_P was found. The change between a 0.5% criterion and 0.1% criterion was found to be 0.003% and thus 0.1% was chosen as the convergence criterion which would be used in the BEM analysis. The overall change of the C_P between the convergence criterion used in this study can be found in figure 5.7.

5.2.3 Effects of Tip losses

For this analysis the number of blades was set to three to correspond with the design which was tested in the wind facility. Also, the wind speed was again set to 11.0 m/s and the number of elements set to 110 with the *Abbot Original* data set. The tip loss was calculated using the Prandtl tip loss factor calculation previously shown in section 2.2.3. This factor will increase the axial induction factor towards the tip of the blade which effectively reduces incoming air velocity and thus the power that can be extracted at the tip. The tip losses can have a significant effect on the overall power produced as the tip is the area of the blade with the most potential for power production. This is due to the larger amount of torque that

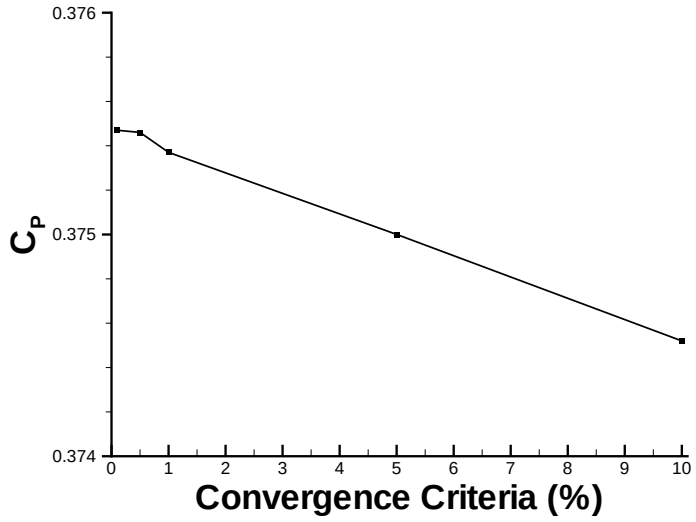

Figure 5.7: Convergence criteria effect on the C_P

can be generated at the tip because of it's larger physical moment arm and the higher relative velocities; as the power produced is directly related to the torque and rotational speed.

Due to the way that the loss factor was calculated it will result in errors at the tip as the iterative loop will try to eventually converge to a value of ϕ approaching zero degrees which will result in a division of zero in the tip loss equation. This problem was avoided by setting the loss factor at the outer tip element to the value calculated for the previous element. This still resulted in the desired sharp reduction in tip loss factor approaching the tip without errors generated by the code. An example of the loss factor as a function of the radius ratio is shown below in figure 5.8.

The effect of the tip loss factor is shown in figure 5.9 which depicts the power each element produced at a TSR of 9.2. The key point of interest is that the losses near the tip result in a lower elemental power production beginning at approximately 80% along the blade. This can be seen as a sharp drop in power produced. Additionally, the drop in the power, for both data sets, produced by the blade, starting at a radius ratio of approximately 0.6, is likely due to the irregular twist distribution used in the calculations, as shown previously in figure 3.13. This would likely result in a lower angle of attack which could reduce the overall lift produced.

5.2.4 Program Output

Due to the nature of the BEM program a large amount of data can be extracted for individual blade elements or for the turbine as a whole. The accuracy of these values is dependent on the accuracy of the input assumptions and aerodynamic

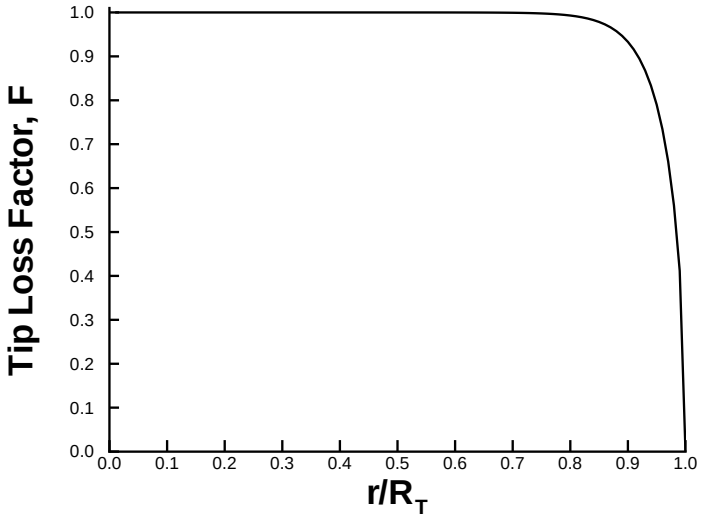

Figure 5.8: Tip loss factor along the length of the blade

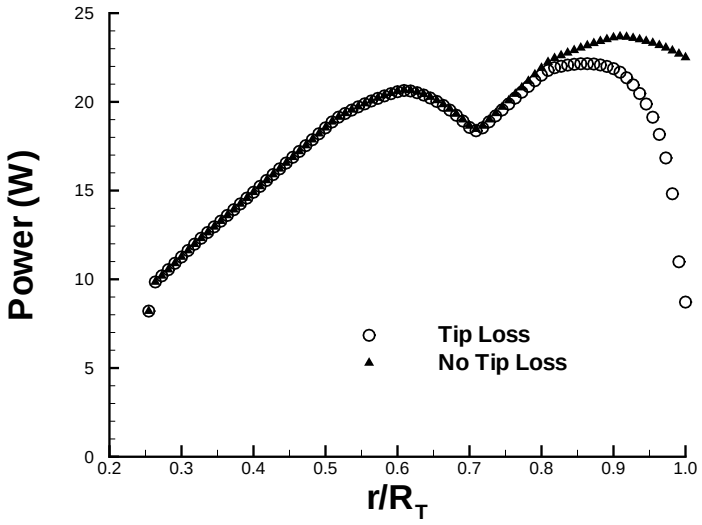

Figure 5.9: Effect of tip losses on the elemental power produced

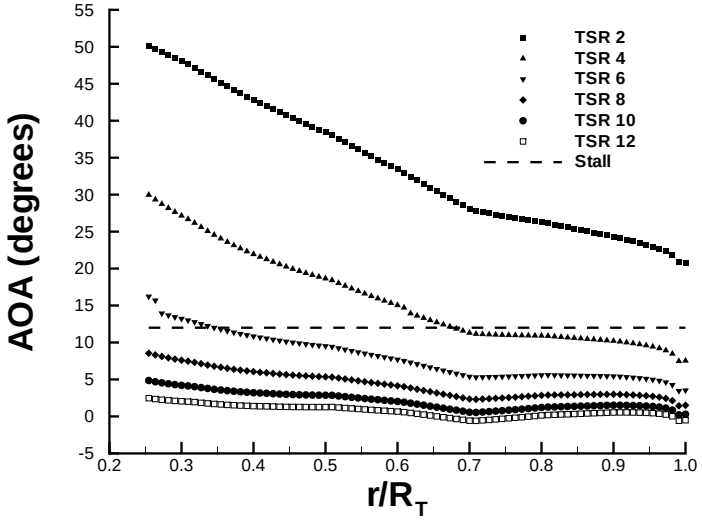

Figure 5.10: Effect of TSR on the AOA over a blade at a wind speed of 11 m/s

properties of the blades; however, they can provide insight into the trends of these various parameters over a wide range of test conditions. These test conditions can include a wide variety of parameters but for this experiment was limited to changes in wind speed and rotational rate. It is also important to note that the BEM program used a constant wind speed input for each run and therefore the rotational rate was directly related to the TSR. These changes in test conditions, at the intervals used in the program, would be difficult to achieve in the real world due to time and equipment constraints.

The results outlined in the following sections show the effect that TSR has on the angle of attack and the estimated induction factors. The trends shown in these sections matched the expected outcome when compared to trends found in a BEM test case implemented by Burton et al. [16].

5.2.4.1 Angle of Attack

Angle of attack estimates can be used to determine which areas of the blade could be experiencing stall conditions at a given TSR. Referring to the blade geometry, figure 2.5, it was expected that as the TSR was increased the AOA across the blade would decrease. This is due to the relative increase in the tangential component of the relative velocity as compared to the incoming wind speed. The results shown in figure 5.10, calculated for a 11 m/s input wind speed with tip losses with a static stall angle of 12 degrees shown for reference, confirm this trend. Although not shown it was found, as theory would suggest, that increasing the wind speed has no effect on the angle of attack at the same TSR, as the velocity triangle geometry will not change.

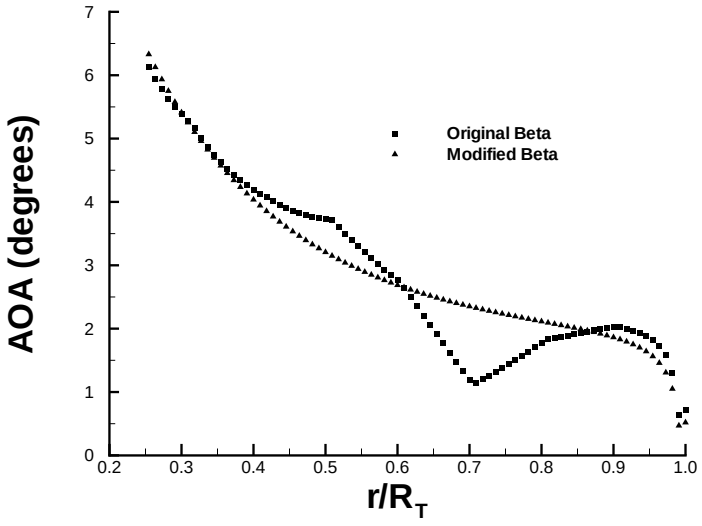

Figure 5.11: Effect of the input β distribution on the AOA output

5.2.4.2 Blade Set Angle Input Effect

When the AOA was plotted for each element at a tip speed ratio of 10 it was evident that the irregularity in the blade set angle, β, had an effect on the program AOA output. In order to ensure that this was not an error in the program a modified β input was used which smoothed out the irregularity using a polynomial curve fit. The results are plotted against each other in figure 5.11 which shows that the input β function will cause the AOA to change; however, the unmodified version was used in all other results shown.

5.2.4.3 Axial and Tangential Induction Factors

The axial induction factor is a measure of the effect that the blades presence has on the incoming air. Figure 5.12 shows the effect that the TSR can have on the axial induction factor. It is shown that the theoretical induction factor will tend to be higher as the TSR increases and due to the effects of tip loss it will approach unity at the tip. The tangential induction factor, which is a measure of the wake rotation induced by the blades, was found, in general, to decrease with an increasing TSR, as shown in figure 5.13. Both sets of values were not affected by changes in the input wind velocity. Again these results correspond to trends found by Burton et al. [16] in the output of their BEM implementation.

With the output of the BEM program now known performance measurements of the experimental wind turbine can be discussed.

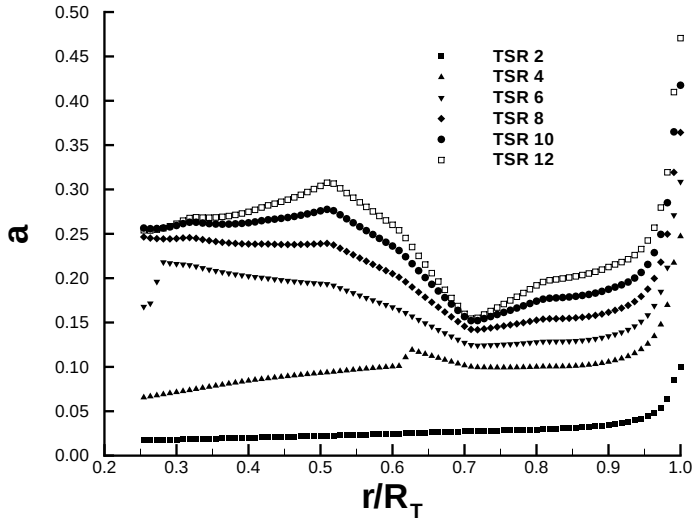

Figure 5.12: Effect of TSR on the axial induction factor, a

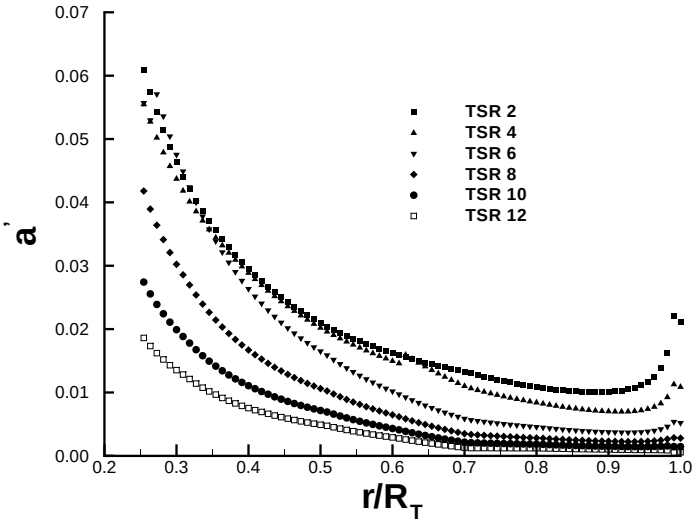

Figure 5.13: Effect of TSR on the tangential induction factor, a'

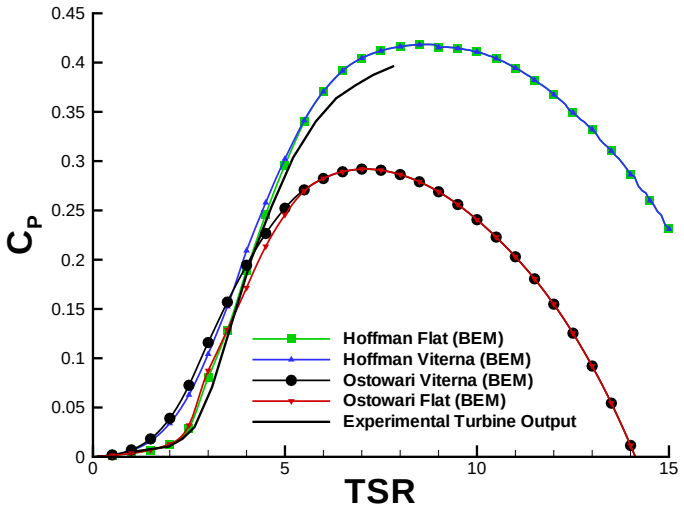

Figure 5.14: Effect of the *Flat* or *Viterna* extrapolation on the calculated C_P with the experimental results also shown

5.2.5 Experimental and BEM C_P Comparison

The primary BEM output of interest, in order to compare to experimental results, was the coefficient of power as a function of the tip speed ratio. The twelve input lift and drag input data sets, outlined in section 3.6.2, were analyzed using the BEM code with tip losses. Wind speed input was set at 11.1 m/s but any change in the input velocity would not have an affect on the coefficient of power at a given TSR. As there were fourteen data sets produced, based on the various lift and drag input files, only relevant and unique results are presented to provide clear results. A curve representative of the experimental data was included based on the results found in section 5.1.4.1.

The first trend identified was that the *Flat* results always produced lower C_P values as compared to *Viterna* data sets and closely matched the experimental results at low tip speed ratios. It was also found that beyond a TSR between 5.25 and 5.75 the C_P results, for a given input aerodynamic property data set, converged regardless of the extrapolation method used. The results begin to overlap because the calculated angle of attack is reduced as the TSR increases and will eventually reach the angle of attack range found in the original input data set. A comparison of the BEM coefficient of power output, with the experimental C_P distribution shown for reference, can be found in figure 5.14 with only the *Ostowari* and *Hoffman* BEM results shown to be representative of these findings. Of note, the *Ostowari Flat* and *Ostowari Viterna* data set resulted in a much lower C_P estimate at high TSR due to an increase in estimated AOA in the *Ostowari* BEM output which, due to the lift and drag distributions, resulted in higher drag and lower lift at higher tip speed ratios.

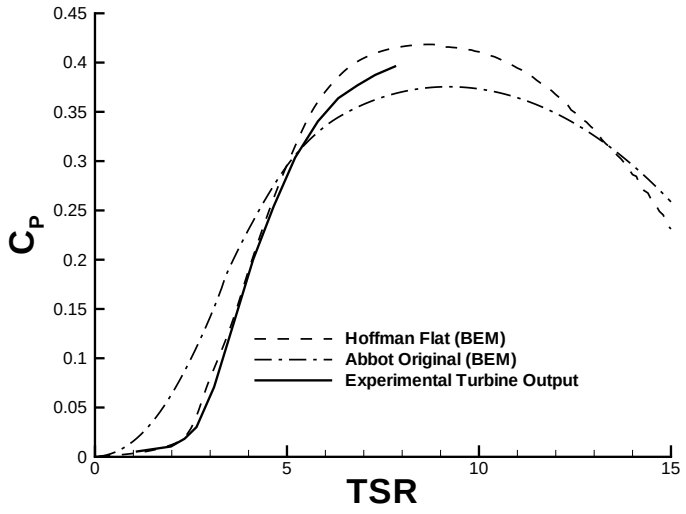

Figure 5.15: Two BEM results compared to experimental C_P results found during testing

Finally, the two sets of BEM results that closely matched the experimental results were the *Hoffman Flat* and the *Hoffman Flat Raw*. These results matched the experimental C_P closely through to a TSR of 5 before diverging and over-predicting the results. The results show that no lift and drag data set was able to accurately predict the turbine output at high TSRs which could indicate that the original, non-extrapolated, data sets were not representative of the three dimensional airfoil performance. The *Abbot Original* results which were the original basis for performance predictions, in addition to the *Hoffman Flat* results, are presented in figure 5.15 with the experimental results found above also presented for reference.

5.2.6 Summary of Experimental Power Production and BEM Modeling

Based on the data collected during testing of the wind turbine in the wind facility the power performance of the turbine was characterized. Power generation measurements were used to estimate the drivetrain losses and from this gross power production as a function of wind speed and the coefficient of power as a function of tip speed ratio. This data will hopefully provide future users of this turbine apparatus a known power response of the turbine to a variety of wind turbine and tunnel conditions which could be helpful at the experimental planning stage.

Additionally a comparison between the experimental performance findings and the BEM predictions was outlined with the results showing a wide range of outputs. If future predictions are based on BEM calculations it was found that the *Hoffman Flat* and *Abbot Original* data sets provided the best match to experimental findings

in the current wind facility.

5.3 PIV Results

With the experimental power findings outlined above a discussion of the flow around the turbine, as found using PIV, can now be made. The particle image velocimetry results taken during testing have the potential to determine the nature of the flow around the blade at various turbine operational states. In total five operational states were chosen for this portion of the experiment which represented three expected tip speed ratios, 4, 6 and 8. The three tip speed ratios would be achieved with three wind speed settings, 6.4, 7.5 and 11 m/s; and four rotational rates 111 rpm, 167 rpm, 195 rpm and 220 rpm. The goal of the PIV testing was to determine if the PIV technique could resolve the flow conditions of an external flow over a blade at different tip speed ratios as well as those present at common tip speed ratios.

As shown in the BEM results the angle of attack of a blade element and coefficient of power at a given tip speed ratio should remain constant. Experimental results given in section 5.1.4 confirm the coefficient of power theory but PIV results had the potential to determine flow characteristics such as angle of attack at a point along the blade.

After the data had been post processed, as outlined in section 4.3, averaged velocity maps in the absolute reference frame could be produced. Additionally, flow parameters such as angle of attack could then be extracted from the relative velocity vector map and streamlines could be produced to aid in the visualization of the flow at the various operational states. Finally, repeatability between test days and within data sets is discussed.

5.3.1 Averaged Flow Results

From the raw images captured during each test a vector map was produced, as discussed in section 4.3. Since each raw velocity correlation could not represent the flow within the entire imaging area it was necessary to average the accepted vectors within each interrogation area to produce a complete vector map. Due to the blade movement within the frame from one image to another the vector maps could not be directly averaged without introducing additional error. As discussed in section 4.3, each image pair was correlated against a master image to determine the relative position of the blade within the frame and shift the vector map to match. Both shifted and unshifted results are initially presented in this section to demonstrate the effect of the blades movement but in all subsequent discussions the shifted results were used.

With the amount of shift determined for each image the corresponding PIV data could be shifted to match. Figures 5.16 and 5.17 represent the unshifted and shifted

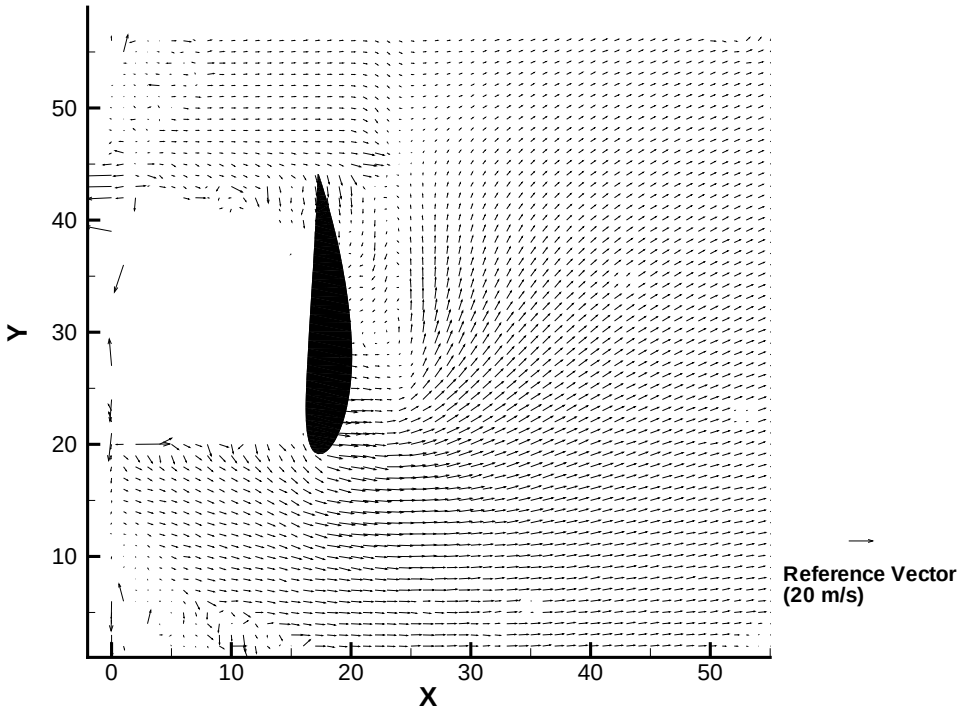

Figure 5.16: Absolute average vector map from unshifted PIV data, TSR 3.8, $\Omega = 198$ RPM, $U_\infty = 11.8$m/s

averaged PIV results overlaid with the position of the blade from the master image used in the shift calculations. It is clear from these figures that the shifted results aligned with the blades position more accurately. Also of note in these figures, and subsequent PIV results, the region upstream of the blade contained no useful data as this was the region shaded from the laser light by the blade.

5.3.2 Variance in Averaged PIV Results

The goal of shifting the images was to also decrease the variability in the data that comprised each averaged value. It was thought that by placing the blade in a common position within the image the flow conditions would also be common from one image to another. Although the variance in data was reduced in some areas the peak variance values found in some areas of the unshifted results still existed within the shifted results. This data variance indicates the variability in the wind and blade flexibility introduce large degrees of variability into the flow being examined around the blade. This variability in the unshifted and shifted data is represented by contours in figures 5.18 and 5.19 which use equation 5.11 to calculate the root sum squared of the standard deviations of the U_X and V_y velocity components.

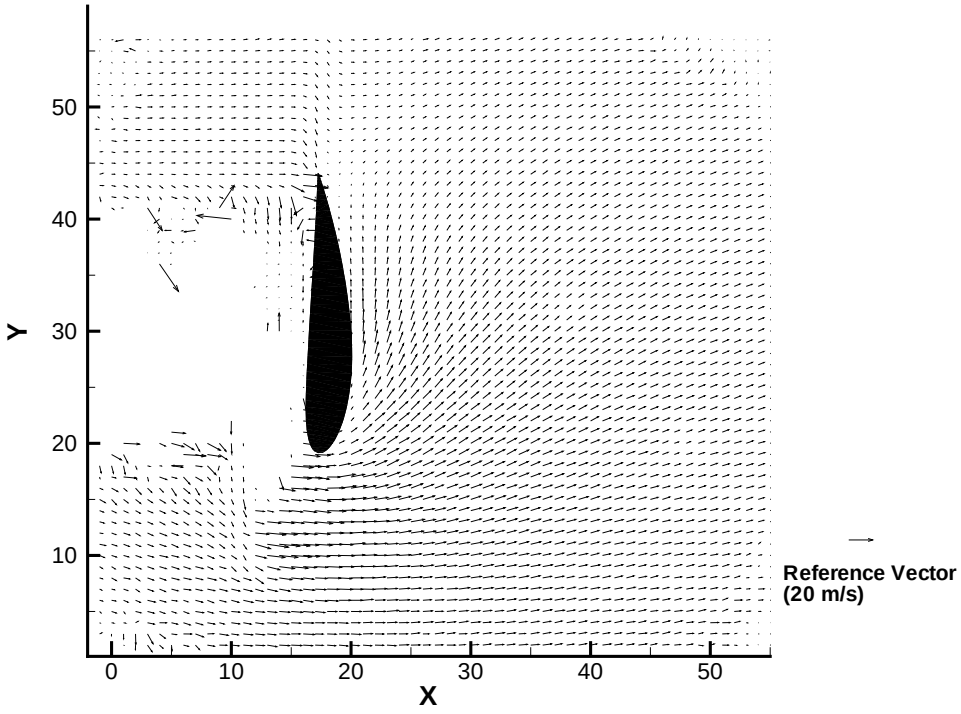

Figure 5.17: Absolute average vector map from shifted PIV data, TSR 3.8, $\Omega = 198$ RPM, $U_\infty = 11.8$m/s

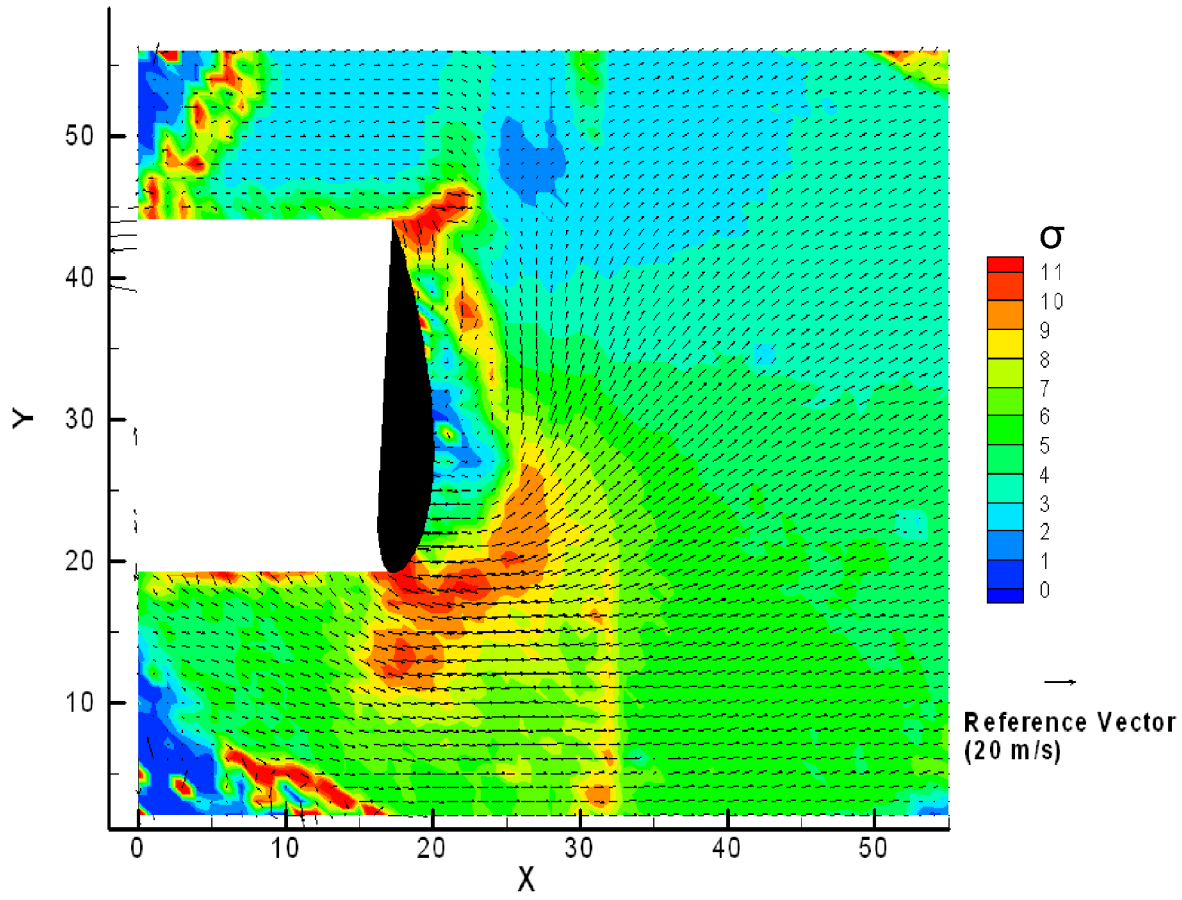

Figure 5.18: Variability of the data in the unshifted PIV data set with σ_{vel} represented by contours, TSR 3.8, $\Omega = 198$ RPM, $U_\infty = 11.8$m/s

$$\sigma_{vel} = \sqrt{(\sigma_U)^2 + (\sigma_V)^2} \tag{5.11}$$

Additional information can be gathered on the confidence of the averaged values found for each interrogation area based on the number of vectors that contributed to the results. The number of non-rejected vectors that comprise each averaged values is shown in figure 5.20. This figure indicates that areas downstream, to the right, of the blade had a higher number of accepted vectors which should mean that these vectors represent strong correlations. Areas to the left of the blade and immediate above and below are not comprised of a large number of accepted vectors which combined with the variance represented in previous plot indicates that these areas will not yield accurate results.

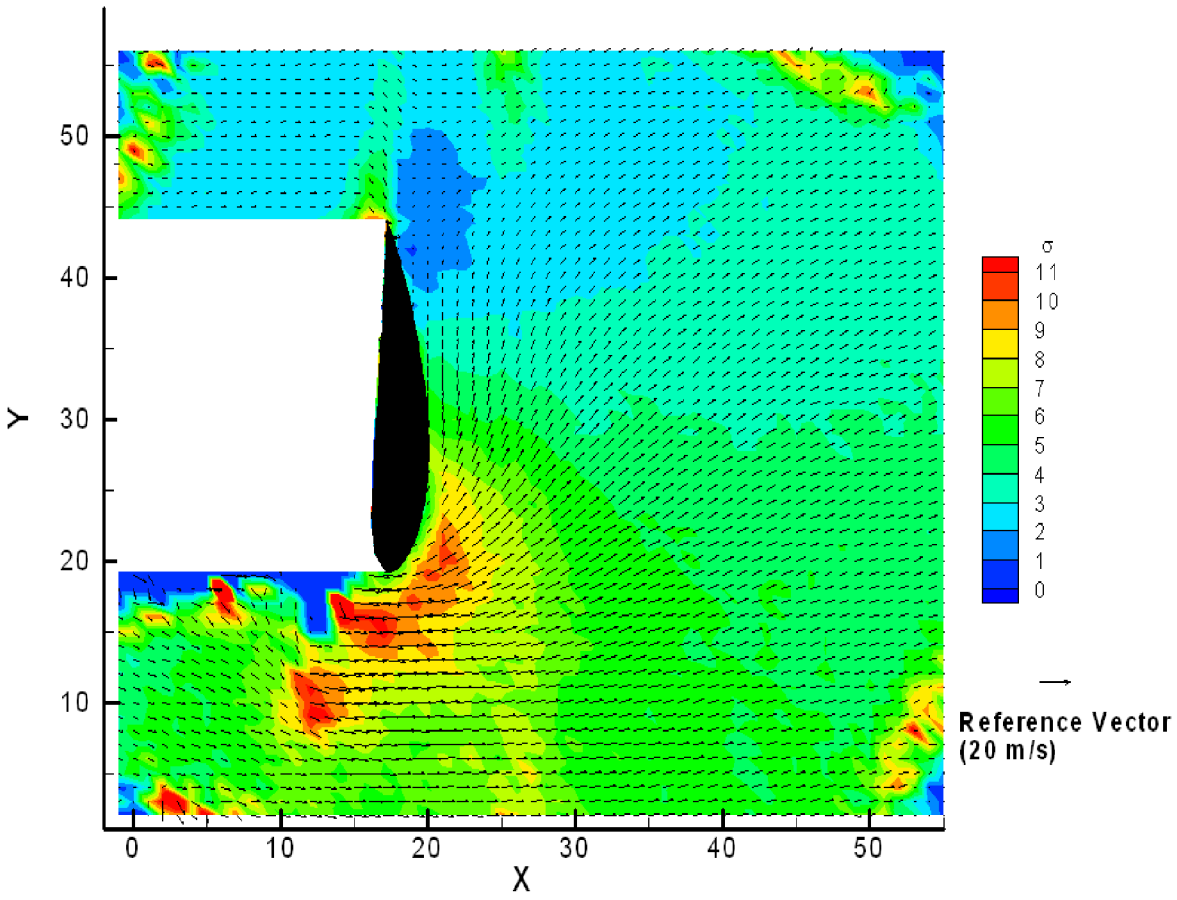

Figure 5.19: Variability of the data in the shifted PIV data set with σ_{vel} represented by contours, TSR 3.8, $\Omega = 198$ RPM, $U_\infty = 11.8$m/s

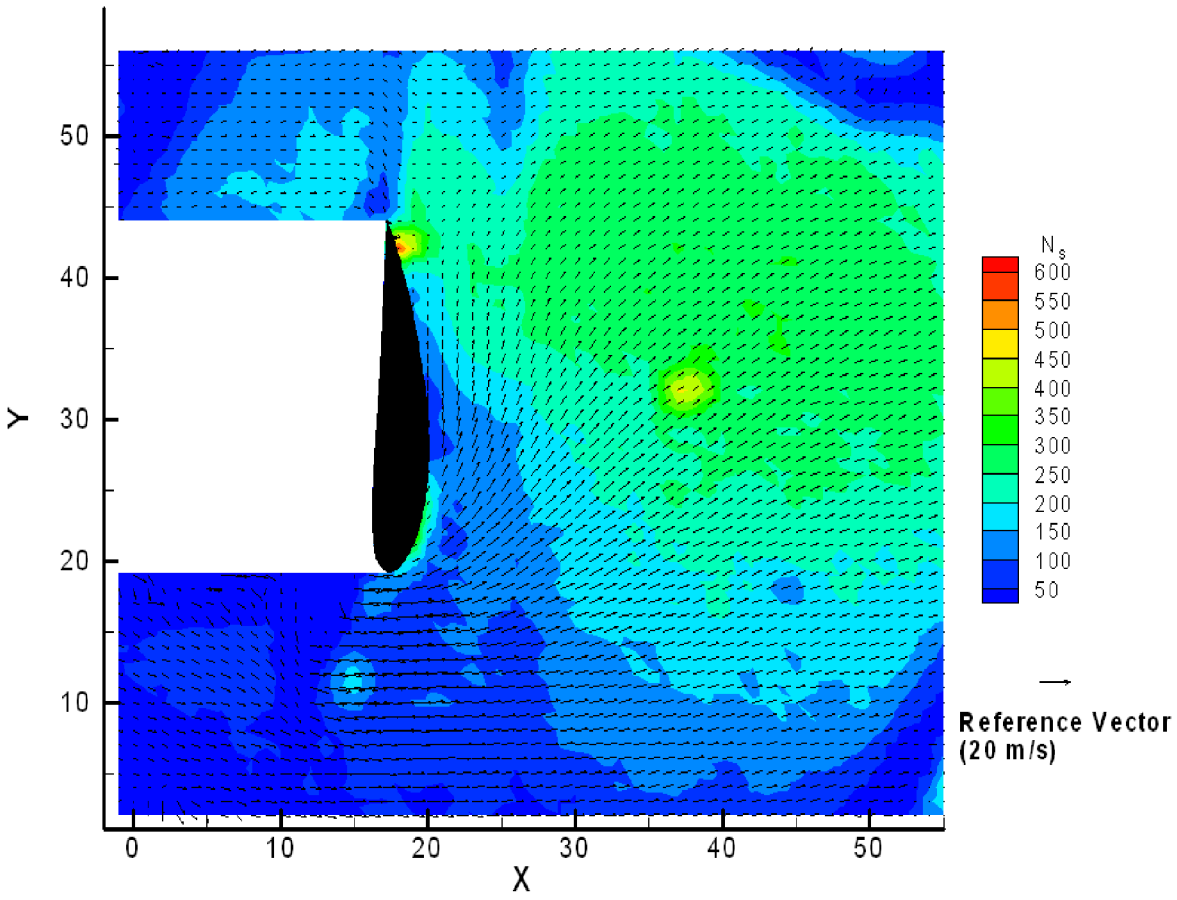

Figure 5.20: Contour plot representing the number of vectors that comprised each averaged vector, TSR 3.8, $\Omega = 198$ RPM, $U_\infty = 11.8$m/s

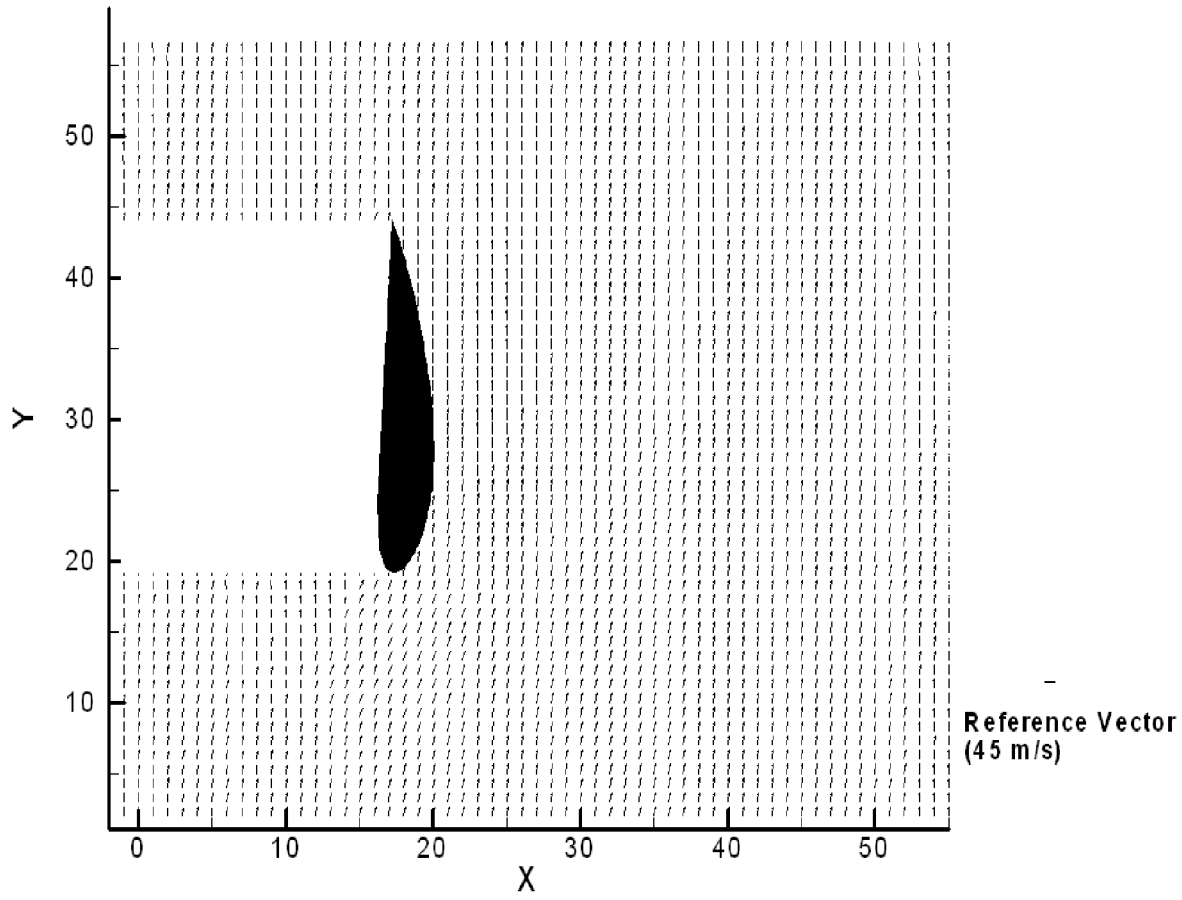

Figure 5.21: Relative reference frame from shifted PIV data, TSR 3.7, $\Omega = 195$ RPM, $U_\infty = 11$m/s

5.3.3 Relative Frame of Reference

To this point all PIV results shown have been in the absolute frame of reference as this was what the raw correlations would produce based on the stationary camera position relative to the blade. In order to translate to the relative frame of reference the blade's tangential velocity, at the radial location of the imaging area, was added to the vertical component of each velocity vector, as shown in equation 5.12. Figure 5.21 demonstrates the 11.8 m/s flow over a blade rotating at 198 rpm overlaid on the master image. Immediately below the blade the inflow angle is most evident in the angle of the velocity vectors.

$$\overrightarrow{V_{abs}} = \Omega r + \overrightarrow{W} \tag{5.12}$$

5.3.3.1 Angle of Attack

In the relative reference frame the angle of attack can also be found based on the velocity triangle geometry. The velocity triangle defines the angle between the relative velocity and the tangential direction as the inflow angle. From physical measurements the blade set angle, β, was known at the radial location as 3.6 degrees. With the inflow and blade angle known the angle of attack could be calculated. Figure 5.22 shows the flow over the blade at a tip speed ratio of 3.8, 11.8 m/s and rotational rate of 198 rpm, with the angle of attack shown by contours and streamlines added to aid in the flow visualization. Testing completed at a tip speed ratio of 3.7 under different input conditions, 6.8 m/s and 111 rpm, was completed to determine if the angle of attack would remain relatively constant as given by theory from the velocity triangle. The results of this second test at the same tip speed ratio can be found in figure 5.23 which indicates that while the angle of attack is not identical in all interrogation areas the trends are similar.

Additional testing completed at a tip speed ratio of 7.4, 6.8 m/s and 220 rpm, was expected to have an angle of attack approximately half that of those found in the TSR 3.8 testing, based on the velocity triangle. The results found at the tip speed ratio of 7.4 are shown in figure 5.24 which does indicate a reduction in angle of attack in many areas except in large angles indicated near the leading and trailing edges which were areas previously found to contain data that was suspected to be less accurate.

5.3.4 Repeatability

The repeatability of PIV results was a concern due to the high level of variability in the wind speed and to a certain degree the rotational rate of the turbine blade. In order to quantify the repeatability of PIV results two separate comparisons were made: the first between two separate tests on different days and the second comparison was made using two different sample sizes of the same velocity correlation data to comprise the averaged results. The first test would determine if environmental conditions on different days could affect the results. The second comparison would determine the affect of the sample size on the results. Again the data sets used were from a tip speed ratio of 3.8, 11.8 m/s and 198 rpm, to represent the expected worst case scenario for repeatability under high turbine loading.

The full velocity correlation data from two different test days was shifted to the master image location and averaged to produce vector maps, using techniques previously outlined. The results from the first test were comprised of 769 correlations and the second test was comprised of 1027 correlations. The resulting U and V components of the mean vector at each interrogation area were subtracted and the change in velocity was quantified as a percentage, given by equation 5.13. Results of this comparison can be found in figure 5.25 with red areas representing data which was more that 100% different between the data sets and blue values

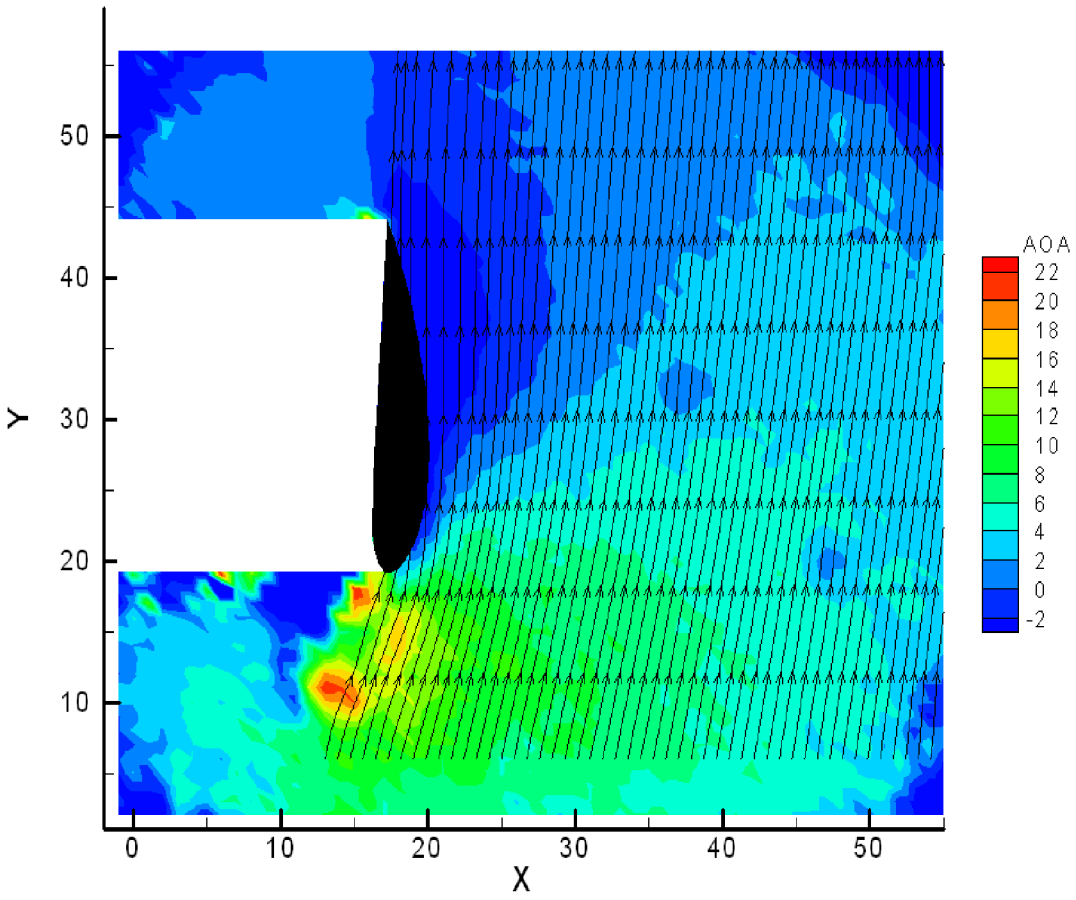

Figure 5.22: Contour plot representing AOA with streamlines representing the flow over a blade, TSR 3.8, $\Omega = 198$ RPM, $U_\infty = 11.8$m/s

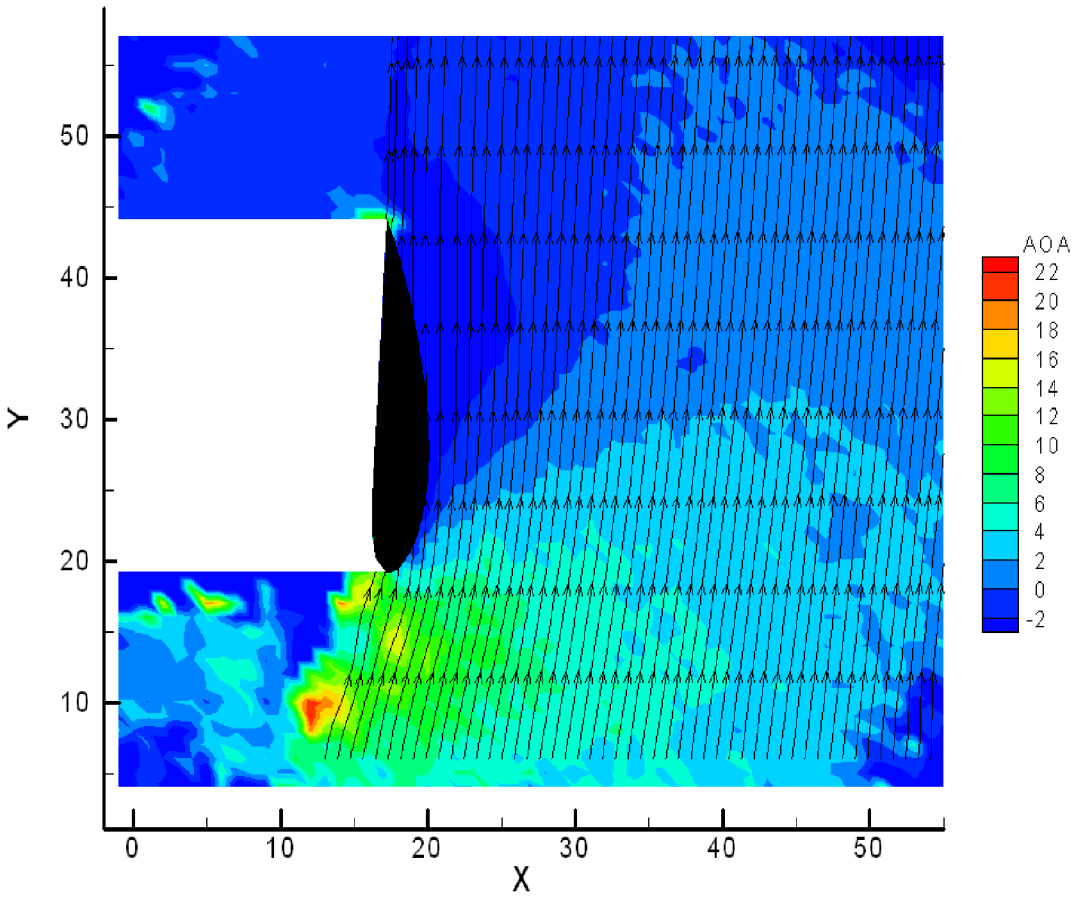

Figure 5.23: Contour plot representing AOA with streamlines representing the flow over blade, TSR 3.7, $\Omega = 111$ RPM, $U_\infty = 6.8$m/s

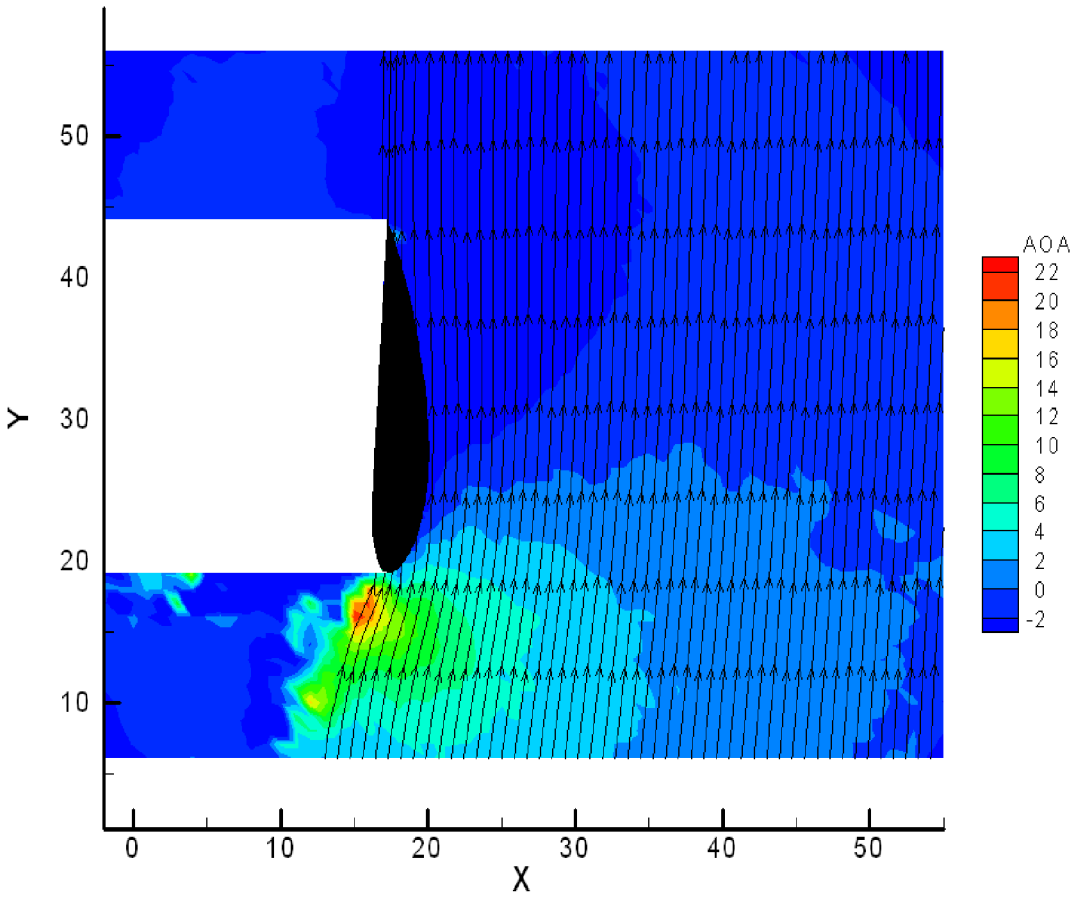

Figure 5.24: Contour plot representing AOA with streamlines representing the flow over a blade, TSR 7.4, $\Omega = 220$ RPM, $U_\infty = 6.8$m/s

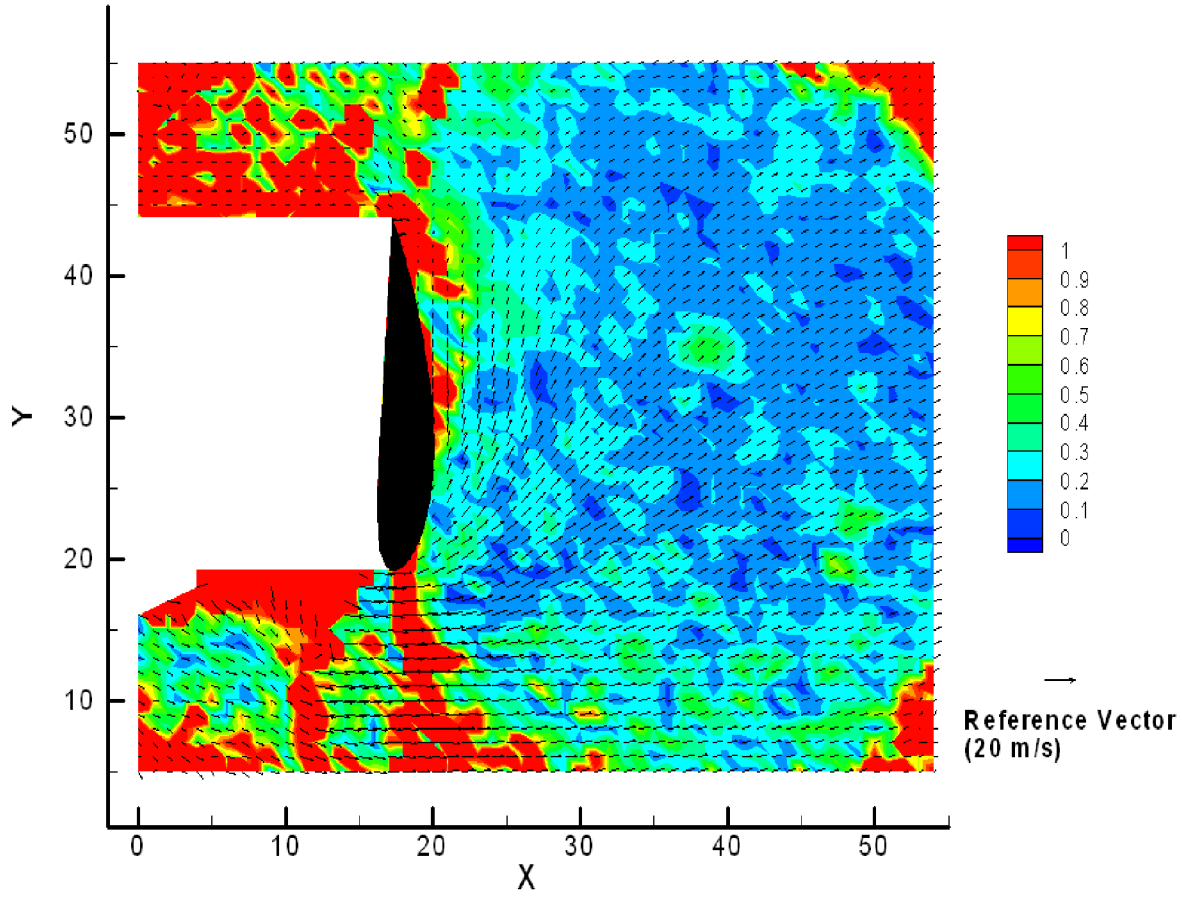

Figure 5.25: Comparison of two tests under the same conditions on separate days at a nominal TSR of 3.8, $\Omega = 198$ RPM, $U_\infty = 11.8$m/s

representing consistent results. Again the areas which represent the best repeatability are those down stream of the blade in the same areas previously indicated to contain the most accurate data. As a comparison the average free stream velocity, based on the data collected by the sonic anemometer, changed by 0.1 m/s or 1% while the rotational rate changed by 0.9% between the two days.

$$Velocity\,Change = \sqrt{\left(\frac{U_1 - U_2}{U_1}\right)^2 + \left(\frac{V_1 - V_2}{V_1}\right)^2} \tag{5.13}$$

In order to determine the repeatability of results, calculated using different sample sizes, within the same correlation data set the results from the first day of testing at a tip speed ratio of 3.8 were used. Both the full data set, comprised of 769 correlations and a random sample of 403 correlations, based on a random selection nominally expected to produce a sample size half that of the original data set. The results of this comparison, based on the change in the U and V components, is

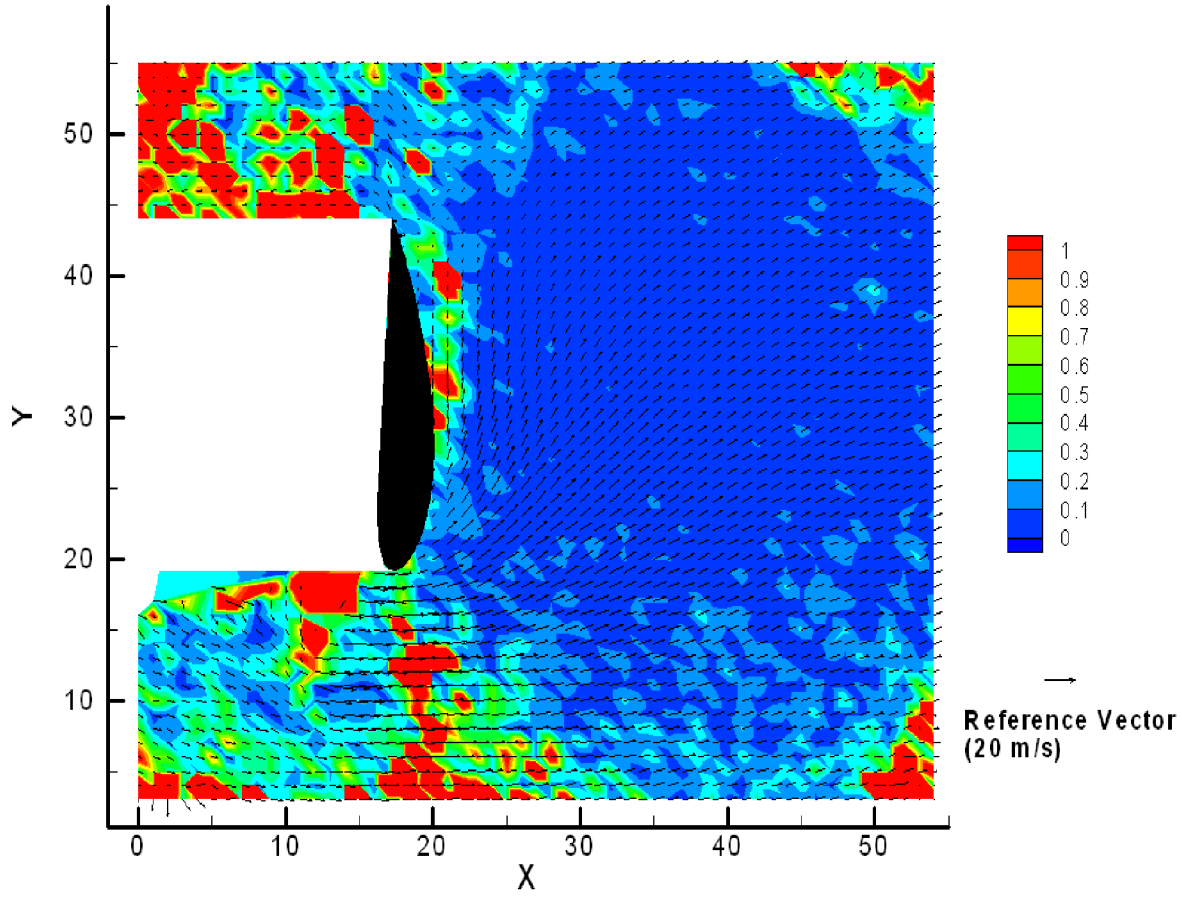

Figure 5.26: Comparison of a common data set with different sample sizes, TSR 3.8, $\Omega = 198$ RPM, $U_\infty = 11.8$ m/s

shown in figure 5.26. Although this comparison still yields areas which are not common within the data the results downstream of the blade indicate that the velocity values are somewhat independent of the sample size.

5.3.5 Summary of PIV Results

Based on the data from tests at various operating points the potential to use PIV on unbounded external flow over wind turbine blades was shown. It was possible to capture results with the blade in the imaging area and to translate the individual PIV results into a relative frame of reference. In the relative frame of reference the relative velocity over the blades and the angle of attack could be determined; however, the high degree of variance in the averaged data, especially near the leading edge, limit the conclusions which can be made using this data. Additionally, the repeatability study indicated that velocity results can change by more than 100% when captured under the same nominal conditions but on different days. Although

the variance and repeatability indicate that improvements to the PIV technique, for this application, need to be made, as a proof of concept study the results are encouraging and represent the potential for further studies.

Chapter 6

Conclusions

The initial objectives of this project were to: measure the power output of a set of turbine blades; evaluate BEM predictions against experimental data; and evaluate the PIV technique for use in an unbounded rotational flow and if possible determine the flow around a turbine blade. All of these goals were achieved and the results were presented in the previous chapter. Outlined below are the conclusions which can be drawn from the presented results. Additionally, improvements to the current apparatus and future work which could be completed are also discussed.

6.1 Wind Turbine Power Production

With basic power data from voltage and current measurements at the generator and load bank the power production of the wind turbine was evaluated. Due to the ability to vary both the incoming wind speed and the rotational rate a unique range of tip speed ratios could be evaluated. The raw power output was calculated as a function of input wind velocity, peaking at 3080 W for a wind speed of 11.1 m/s. The effect of the tip speed ratio on the power coefficient was also of interest as this indicated the peak power production range for this particular turbine. While the test apparatus was limited in it's rotational speed, and thus peak tip speed ratio, the peak coefficient of power was approaching 40%.

Although the variability in the wind facility free stream velocity was high the power production results, specifically in the non-dimensional power coefficient curve, demonstrate repeatability. This repeatability in the power measurements was likely due to the inertia of the rotating turbine damping out the high frequency variation in the input wind speed.

6.2 BEM Predictions

As the results found in section 5.2.5 show the BEM prediction results are highly variable and dependent on the input airfoil aerodynamic properties. While some

BEM results were found to match experimental results at certain points in the power curve, the variability between data sets confirmed the limited use these results can have for design purposes. However, it is a useful tool to determine trends in parameters such as angle of attack and induction when evaluating the effects of different operating conditions involving combinations of wind speed and rotational rate. If experimental time is limited this can help to determine which operating conditions should be tested to maximize the potential of the output data. For example if the objective of a test is to determine changes in the angle of attack along a blade the rate of change of angle of attack is much higher at low tip speed ratios than at higher tip speed ratios, as shown in figure 5.10, which could indicate more testing would be required at low tip speed ratios to capture this rate of change.

6.3 PIV

The experimental application of the PIV technique on the unbounded external flow over a rotating turbine blade presented unique challenges in addition to the technical challenges normally associated with the PIV technique. Despite these challenges, the PIV results presented show the potential to quantify the flow around the blade and represented a unique application of the PIV technique; however, the movement of the blade within the imaging plane, primarily in the streamwise direction, and the velocity fluctuations in the free stream were likely the cause of the limited repeatability of the results. It was shown through post-processing of the images that the PIV results could be shifted to correspond to a common master image but this did not significantly improve the variance in the data.

The PIV results could be translated into a relative frame of reference which had the potential to extract inflow angle, relative velocity and angle of attack values. Although the variance in the data did not allow a specific value to be found with any confidence the technique was considered viable. Improvements to the tunnel flow conditions and a reduction in turbine vibrations could allow PIV could be a viable technique in accurately quantifying the flow around this turbine. Although the final PIV results are only valid as a proof of concept they do represent a unique, and first known, measurement of the flow field over a rotating turbine blade.

6.4 Equipment Improvements

While the results found using the current equipment allowed power production and flow measurements to be collected; inevitably, equipment improvements will allow an increased amount of unique data sets to be collected and analyzed. Improvements to: the structure of the nacelle, blades, wind facility, instrumentation and PIV equipment could all help to increase the accuracy and repeatability of the results and allow a greater range of operating conditions to be tested.

6.4.1 Turbine and Blade Assembly

As discussed previously the current turbine apparatus and blades do not allow for rotational rates beyond 220 RPM to be achieved without an excessive level of vibration. This has been mostly attributed to the dynamic balance of the blade assembly as the vibrations tend to increase with increasing rotational rate independent of any input wind from the fan banks. As the nacelle and tower structure were originally designed for a two bladed rotor with shorter blades installed more design analysis could be completed to help identify areas where structural improvements could be made to help reduce the potential for vibrations at common blade rotational frequencies which could be encountered during future tests.

The blades themselves also experienced a noticeable amount of flexing at the tip due to the loading at high wind speeds and rotational rates. This flexing was expected but likely added to the variability of the PIV results near the tip of the blade. While nothing can be done to improve the structure of the existing blades mitigating this flexibility in future blade designs would likely improve any results whether they are power, pressure or PIV based. To this end the MEXICO project [6] used milled aluminum blades for all testing to help improve the stiffness of the blades and thus the repeatability of their tests which could be used as a model for future experimental blade structure.

Significant improvements could also be made to the rotational speed control of the blades. Currently this control is manual and relies on the operator tracking the speed of the rotor with a computer readout and adjusting the input voltage to the field and armature to achieve the desired rotational rate. Ideally this would be accomplished automatically with an electronic speed controller which would allow the operator to have greater control over the speed of the rotor. Alternatively, or in conjunction with a speed controller, greater control over the turbine loading, currently in the form of a fixed resistance load bank, could be achieved using a variable resistive load. As the load bank currently has a fixed resistance it must be able to absorb the maximum expected power output of the turbine for any given test. With a variable resistive load on the turbine the power absorbed by the load bank could be dynamically altered to provide speed control to the turbine, essentially acting as an electric braking system.

6.4.2 Wind Facility

The wind tunnel streamwise velocity characteristics, outline in section 3.2.1, indicated that there was a high level of turbulence present in the flow which was also observed during PIV testing in the smoke particle stream motion. This turbulence was seen as one of the leading contributors to the challenges encountered while attempting PIV measurements on the blades and ultimately to the limited repeatability of the PIV results. While this facility will likely not achieve very low turbulence levels often found in purpose built wind tunnels, improvements to the

facility and the layout could improve the flow conditions for wind turbine testing. These improvements could include, but are not limited to, the flow straightening section of the facility, fan outlets and moving semi-permanent objects which currently obstruct the flow path.

6.4.3 Instrumentation

While current instrumentation allows the power into and out of the generator to be measured the power produced by the blades can only be estimated from these measurements. A torque sensor placed on the low speed shaft, combined with an improved rotational rate sensor, would provide a more accurate measurement of the torque and power that the blades are producing. Additionally pressure sensors on the blades and load cells attached to each blade could help to provide more information on the individual blade loading. As blade pressure and load measurements were made during the NREL [5] and MEXICO [6] studies; future testing, with the current apparatus, which incorporated similar sensors could only improve the confidence in the results and conclusions.

6.4.4 PIV Equipment

Finally, improvements to the PIV equipment will help to gain a better understanding of the complex flow which is present around a turbine blade. Based on current results the improvements, outlined above, to the tunnel and turbine assembly should be made in order to improve the repeatability and quality of the PIV results. If these improvements are made the camera and laser used to capture the images could then be upgraded. These upgrades would primarily involve the speed at which images are captured which can ultimately lead to time-resolved PIV images. Time-resolved PIV would be able to capture any transient effects as the blade moves through the imaging plane.

Movement of the camera and laser sheet to various radial locations along the blade as well as traversing upstream and downstream of the blade would be the next logical step in PIV experimentation on this apparatus. Imaging at different points along the blade would provide insight into the flow patterns closer to the root of the blade. Additionally imaging completed upstream and downstream of the rotor plane would allow the affect of the rotors presence on the free stream to be quantified. These tests would be similar to the MEXICO project goals and results [15] and could yield PIV based measurements of parameters such as the axial and tangential induction factors.

6.5 Recommendations for Future Research Projects

In most experimental studies more work can be done and further analysis of the resulting data is likely possible. The equipment improvements outlined above list some of the limitations of the current experimental apparatus and some of the improvements which can be made to rectify those limitations. With the relevant equipment improvements in place the potential for future research projects studying power production and blade flow aerodynamics are endless. Research projects related to power production, BEM modeling and PIV are proposed below.

6.5.1 Power Production Studies

Some future studies which could yield interesting power production results for examination could include: different blade configurations, yawed rotor plane, higher wind speeds and rotational rates and thus a wider range of tip speed ratios. Custom blade configurations would allow studies which could determine the effects of: tip design, surface roughness or twist distributions on the power production. Based on the previous studies by NREL and MEXICO, as outlined in section 2.1, the power production of a wind turbine in yawed conditions is of interest to the wind turbine research community. Finally, testing conducted over a wider range of tip speed ratios will allow the peak power to be determine for the current rotor design as current limitations on wind speed and rotational rates were a limiting factor for testing. Overall the flexibility inherent in the design of the turbine structure and the electrical system should yield useful data through a wide range of applications.

6.5.2 BEM Model Studies

The inability of the basic BEM model, implemented for this study, to accurately predict the output of the wind turbine's experimental power output demonstrated a need for an improved model. For future experiments an approximation of the turbine performance and loading will be useful if different blade designs or operating conditions are studied. With the experimental power production of the current turbine configuration now known it may be possible to adjust the model input parameters such as the tip loss factor or aerodynamic lift and drag curves to improve the correlation to the experimental data. Studies could also be completed determine the effect of dividing the blades into different airfoils instead of the current implementation which assumes the blade can be represented by a single NACA profile. Additionally, implementing advanced models which attempt to account for three dimensional effects and wake flow conditions could help to improve the accuracy of the predictions, although even advanced models struggle to consistently predict turbine output, as discussed in section 2.1.1.3.

6.5.3 PIV Studies

The PIV experimentation shows promise for further study due to the unique application of the technique when used to measure the flow around the blades. If the issues related to seeding and free stream turbulence are solved studies related to the flow in and around the blade and rotor plane would yield unique results and data for the wind turbine research community. Specific areas of research could include: chordwise flow measurements captured at various radial locations; measuring span wise (radial) flow which may be present during some operation points; finally, placement of the camera in the rotating domain to allow image capture at various azimuth points and to allow time resolved PIV measurements of the blade flow.

References

[1] Abbot, Ira H. and Albert E. Von Doenhoff, *Theory of Wing Sections*. Dover Publications Inc., New York, NY, 1959. iii, xiii, 35, 37, 39, 40

[2] Hoffman, M. J., R.R. Ramsay and G.M. Gregorek, *Effects of Grit Roughness and Pitch Oscillations on the NACA 4415 Airfoil*. Tech. Rep. NREL/TP-442-7815, NREL, Golden, Colorado, July 1996. iii, xiii, 35, 38, 39, 40

[3] *IEA Wind Energy Annual Report 2007*. Tech. rep., IEA Wind, July 2008. 1

[4] *Energy Statistics Handbook: Fourth Quarter 2008*. Tech. Rep. 57-601-X2008004, Statistics Canada, May 2009. 1

[5] Hand, M. M., D. A. Simms, L. J. Fingersh, D. W. Jager, J. R. Cotrell, S. Schreck and S. M. Larwood, *Unsteady Aerodynamics Experiment Phase VI: Wind Tunnel Test Configurations and Available Data Campaigns*. Tech. Rep. NREL/TP-500-29955, NREL, December 2001. xi, 4, 5, 7, 104

[6] Schepers, J. G. and H. Snel, *Model Experiments in Controlled Conditions: Final Report*. Tech. Rep. ECN-E–07-042, ECN, June 2007. xi, xii, 4, 9, 10, 11, 12, 20, 103, 104

[7] Somers, D. M., *Design and Experimental results for the S809 Airfoil*. Tech. Rep. NREL/SR-440-6918, Airfoils Inc. for NREL, January 1997. 5

[8] Schreck, Scott, *The NREL Full-Scale Wind Tunnel Experiment: Introduction to the Special Issue*. Wind Energy, 5:77–84, 2002. xii, 6

[9] Schepers, J. G. and R.P.J.O.M. van Rooij, *Analysis of aerodynamic measurements on a model wind turbine placed in the NASA-Ames tunnel: ECN's and TUD's contribution to IEA Wind Task XX*. Tech. Rep. ECN-E–08-052, ECN, 2008. xii, 7

[10] Simms, D., S. Schreck, M. Hand and L. J. Fingersh, *NREL Unsteady Aerodynamics Experiment in the NASA-Ames Wind Tunnel: A Comparison of the Predictions to Measurements*. Tech. Rep. NREL/TP-500-29494, NREL, 2001. 8

[11] Coton, Frank N., Tongguang Wang and Roderic A McD. Galbraith, *An Examination of Key Aerodynamic Modelling Issues Raised by the NREL Blind Comparison*. Wind Energy, 5:199–212, 2002. 8

[12] Breton, Simon-Philippe, Frank N. Coton and Geir Moe, *A Study on Rotational Effects and Different Stall Delay Models Using a Prescribed Wake Vortex Scheme and NREL Phase VI Experiment Data*. Wind Energy, 11:459–482, 2008. 8

[13] Laino, David J., A. Craig Hansen and Jeff E. Minnema, *Validation of the AeroDyn Subroutines Using NREL Unsteady Aerodynamics Experiment Data*. Wind Energy, 5:227–244, 2002. 8

[14] Schreck, Scott J., Niels N. Sorensen and Michael C. Robinson, *Aerodynamic Structures and Processes in Rotationally Augmented Flow Fields*. Wind Energy, 10:159–178, 2007. 9

[15] Snel, H., J.G. Schepers and B. Montgomerie, *The MEXICO project (Model Experiments in Controlled Conditions): The database and first results of data processing and interpretation*. Journal of Physics: Conference Series The Science of Making Torque from Wind, 75:1–11, 2007. xii, 9, 11, 12, 20, 104

[16] Burton, Tony, David Sharpe, Nick Jenkins and Ervin Bossanyi, *Wind Energy Handbook*. John Wiley and Sons Canada Ltd., 2006. xv, 13, 15, 82, 83, 111, 112

[17] The Mathworks Inc., *Matlab*. xi, 14, 62, 66, 113

[18] Martinez, Jaime, Luca Bernabini, Oliver Probst and Ciro Rodriguez, *An Improved BEM Model for the Power Curve Prediction of Stall-regulated Wind Turbines*. Wind Energy, 8:385–402, 2005. 16

[19] Glauert, H., *'Airplane Propellers', Aerodynamic Theory: A General Review of Progress*, vol. IV. (ed. William Frederick Durand), Dover Publications Inc., New York, 1963. 16

[20] Shen, Wen Zhong, Robert Mikkelsen and Jens Norkaer Sorensen, *Tip Loss corrections for Wind Turbine Computations*. Wind Energy, 8:457–475, 2005. 16

[21] Dantec Dynamics Inc., *FlowMap Particle Image Velocimetry Instrumentation: Installation and User's Guide*, 1999. 18, 60

[22] Melling, A, *Tracer particles and seeding for particle image velocimetry*. Measurement Science Technology, 8:1406–1416, 1997. 18

[23] New Wave Research, *Solo PIV Nd:YAG Laser System Operator's Manual*, April 2006. 19, 42, 60

[24] *Particle Image Velocimetry (PIV) Principles.* Dantec Dynamic Inc., May 2009, http://www.dantecdynamics.com/. xii, 19

[25] Altaf, Ammar Mohammadnour, *Experimental Investigation of the Flow Behaviour Inside a Centrifugal Impeller Channel at Design and Off-Design Flow Rates.* Master's thesis, University of Waterloo, 2007. 19

[26] Sante, Alberto Di, Raf Theunissen and Rene A. Van den Braembussche, *A new facility for time-resolved PIV measurements in rotating channels.* Experimental Fluids, 44:179–188, 2008. 19

[27] Ferreira, Carlos Simao, Gijs van Kuik, Gerard van Sussel and Fulvio Scarano, *Visualization by PIV of dynamic stall on a vertical axis wind turbine.* Experimental Fluids, 46:97–108, 2009. 20

[28] McWilliam, Michael K., *Development of a Wind Turbine Test Apparatus for Horizontal Axis Wind Turbine Rotor Testing.* Master's thesis, University of Waterloo, Waterloo, ON, 2008. xii, 21, 25, 26, 30

[29] Johnson, David, *Wind Energy Laboratory.* University of Waterloo, Department of Mechanical and Mechatronics Engineering, September 2006, http://www.mme.uwaterloo.ca/~da3johns/johnfacility.html. 21

[30] Wraith, Chris, *Personal Correspondence.* Composotech Structures Inc., 2007-2008, http://www.composotech.com. 30, 124, 126, 127

[31] *Whisper 500.* Southwest Windpower Inc, February 2007, http://www.windpower.com/products/whisper_500.htm. 30

[32] SolidWorks Corporation, *SolidWorks*, 2006. 32

[33] Trapp, Jens and Robert Zores, *NACA 4 Digit series*, April 2008, http://www.pagendarm.de/trapp/programming/java/profiles/NACA4.html. 34

[34] Ostowari, C. and D. Naik, *Post Stall Studies of Untwisted Varying Aspect Ratio Blades with an NACA 4415 Airfoil Section - Part I.* Wind Engineering, 8(3):176–194, 1984. xiii, 35, 38, 39, 40, 41

[35] Drela, Mark and Harold Youngren, *Xfoil 6.96*, 2006, http://web.mit.edu/drela/Public/web/xfoil/. xiii, 35, 38, 39, 40

[36] Hansen, Craig, *NWTC Design Codes: AirfoilPrep*, January 2007, http://wind.nrel.gov/designcodes/preprocessors/airfoilprep/. 35

[37] Viterna, L.A. and D.C. Janetzke, *Theoretical and Experimental Power from Large Horizontal-Axis Wind Turbines.* Tech. Rep. NASA TM-82944, NASA, September 1982. 36

[38] Moriarty, Patrick J. and A. Craig Hansen, *AeroDyn Theory Manual*. Tech. Rep. NREL/EL-500-36881, National Renewable Energy Laboratory, Colorado, December 2005. 36

[39] Laino, David J. and A. Craig Hansen, *User's Guide to the Wind Turbine Aerodynamics Computer software: AeroDyn*. Windward Engineering, Salt Lake City, Utah, 12.50 ed., December 2002. 36

[40] Dantec Dynamics Inc., *FlowManager*, 1999. 41, 137

[41] National Instruments Corp, *Kodak Megaplus ES 1.0 Camera Manual*. 372259a-01 ed., November 1998. 42, 60

[42] Keithley Instruments Inc., *Model 2700 Multimeter/Switch System User's Manual*, 2001. xi, 48, 49, 118

[43] National Instruments Corp., *NI 6251 Specifications*. 371291h-01 ed., 2007. 48, 119

[44] Campbell Scientific Canada Corp, *3-D Sonic Anemometer User Manual*, 2004. 48

[45] National Instruments Corp., *Labview*. vii, 50

[46] Holman, J.P., *Experimental Methods for Engineers*. McGraw Hill, Toronto, 1966. 63, 71

[47] Moffat, Robert J., *Describing the Uncertainties in Experimental Results*. Experimental Thermal and Fluid Science, 1:3–17, 1988. 116

[48] Seglenieks, Frank, *Waterloo Weather Station*. University of Waterloo, Department of Civil and Environmental Engineering, 2008, `http://weather.uwaterloo.ca`. 120

[49] *CoREZYN COR61-AA-340 Resin*. Interplastic Corporation: Thermoset Resins Division, `http://www.interplastic.com/corezyn_TR.html`. 126

[50] *Hydrophilic Amorphous Fumed SIlica: HC0043040*. Wacker Chemie AG, `http://www.wacker.com`. 126

[51] *Econostitch 5445 Data Sheet*. Tech. rep., Airtech Advanced Materials Group, Huntington Beach, CA, November 2008, `www.peelply.com`. 130

Appendix A

BEM

A.1 Betz Limit Derivation

The BEM theory, as the name implies, was based on a momentum analysis of a rotor which is modeled as a momentum sink. This rotor will decrease the streamwise velocity along a streamtube and have a sharp pressure drop across the rotor plane, as shown in figure A.1 from Burton et al. [16]. A streamwise momentum analysis will yield equation A.3 based on the terms outlined in figure A.1 and the definition of the axial induction factor found in equation A.1.[16]

$$a = \frac{U_\infty - U_d}{U_\infty} \tag{A.1}$$

$$\sum F_x = \left(P_d^+ - P_d^-\right) A_d = \left(U_\infty - U_W\right) \rho A_d U_d \tag{A.2}$$

$$\sum F_x = \left(P_d^+ - P_d^-\right) A_d = \left(U_\infty - U_W\right) \rho A_d U_\infty \left(1 - a\right) \tag{A.3}$$

The Bernoulli equation was then used to determine a relationship, found in equation A.6, between the pressure difference across the rotor plane and the air velocity upstream and downstream of the turbine.

$$\frac{1}{2}\rho U_\infty^2 + P_\infty = \frac{1}{2}\rho U_d^2 + P_d^+ \tag{A.4}$$

$$\frac{1}{2}\rho U_W^2 + P_{\infty=}\frac{1}{2}\rho U_d^2 + P_d^- \tag{A.5}$$

$$P_d^+ - P_d^- = \frac{1}{2}\rho\left(U_\infty^2 - U_W^2\right) \tag{A.6}$$

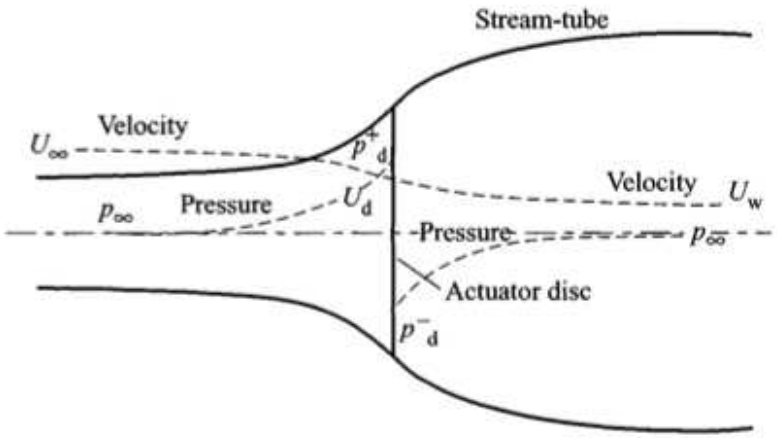

Figure A.1: Rotor model used in the BEM analysis [16]

By substituting the pressure terms from equation A.6, into the momentum equation a relationship between the downstream velocity, U_W, and the free stream velocity can be found as found in equation A.9.

$$\frac{1}{2}\rho\left(U_\infty^2 - U_W^2\right)A_d = \left(U_\infty - U_W\right)\rho A_d U_\infty\left(1-a\right) \tag{A.7}$$

$$\frac{1}{2}\left(U_\infty + U_W\right) = U_\infty\left(1-a\right) \tag{A.8}$$

$$U_W = U_\infty\left(1-2a\right) \tag{A.9}$$

Returning to equation A.3 the force in the streamwise direction can be found in order to determine the power absorbed by the rotor. The downstream velocity, from equation A.9 was substituted into the momentum equation and reduced to get equation A.11.

$$F_x = \rho A_d U_\infty\left(1-a\right)\left[U_\infty - U_\infty\left(1-2a\right)\right] \tag{A.10}$$

$$F_x = 2 * \rho A_d U_\infty^2 a\left(1-a\right) \tag{A.11}$$

The power that is absorbed by the rotor is then found using the streamwise force, F_x, and the velocity at the rotor, U_d, and is shown in equation A.13.

$$P = F_x U_d \tag{A.12}$$

$$P = 2\rho A_d U_\infty^3 a\left(1-a\right)^2 \tag{A.13}$$

The coefficient of power can then be found, as defined by equation A.14, using the power derived above. The coefficient of power based on this momentum analysis, is shown in equation A.16, was found to only be a function of the axial induction factor.

$$C_P = \frac{P}{\frac{1}{2}\rho A_d U_\infty^3} \tag{A.14}$$

$$C_P = \frac{2\rho A_d U_\infty^3 a\left(1-a\right)^2}{\frac{1}{2}\rho A_d U_\infty^3} \tag{A.15}$$

$$C_P = 4a\left(1-a\right)^2 \tag{A.16}$$

The maximum coefficient of power was then determined by differentiating equation A.16 with respect to the axial induction factor. The maximum power coefficient was found to be 59.3% at an induction factor of 1/3 and is referred to as the Betz limit.

A.2 BEM Matlab Code

Outlined below is the code used to implement the BEM theory in Matlab [17].

```
clear;
close all;
tic
%Airfoil parameters found from actual blade
R_t=2.1735; %metres
N=3; % number of blades
excl=0.246719; %amount to exclude, hub area
u_inf=11.13; %free stream velocity (m/s)
rho=1.2; %density (kg/m^3)

%use 'chord(r_rat)' function to get chord at r/R value
%use 'setangle(r_rat,excl)' function to get beta at r/R value
%use 'force(alpha)' to get cl and cd at angle of attack in degrees

%choose number of elements to divide blade
elem=110;

m=1; %initialize tip speed iteration counter

for k=0.1:0.1:15
    lamda_t=k;

    %initialize arrays
    phi=zeros(1);
    beta_val=zeros(1);
    alpha=zeros(1);
    sigma=zeros(1);
    cl=zeros(1);
    cd=zeros(1);
    a=zeros(1);
    a_prime=zeros(1);
    factor=zeros(1);
    F=zeros(1);

    %initialize total values
    T=0;
    Th=0;
    P=0;

    %find initial values based on optimum rotor
    for i=1:elem
        r_rat=i/elem;
        lamda(1,i)=lamda_t*r_rat; %element speed ratio
        a(1,i)=1/3;
        a_prime(1,i)=0;
```

```
        phi(1,i)=atan(2/3/lamda(1,i)); %inflow angle,radians
        beta_val(1,i)=deg2rad(setangle(r_rat,excl));
        alpha(1,i)=phi(1,i)-beta_val(1,i); %angle of attack, radians
        sigma(1,i)=N*chord(r_rat)/2/pi/R_t/r_rat;
        [cl(1,i),cd(1,i)]=force(rad2deg(alpha(1,i)));
        F(1,i)=1;
    end

    %iterate to get final a and a_prime and thus phi
    for i=1:elem %element on blade
        j=2; %iteration counter using first guess from above as j=1
        converg=-1; %initialize convergence calculation
        r_rat=i/elem; %radius ratio

        F_val=F(1,i);

        while converg==-1
            C_n=cl(j-1,i)*cos(phi(j-1,i))+cd(j-1,i)*sin(phi(j-1,i));
            C_t=cl(j-1,i)*sin(phi(j-1,i))-cd(j-1,i)*cos(phi(j-1,i));

            a(j,i)=1/(4/sigma(1,i)/C_n*F_val*(sin(phi(j-1,i)))^2+1);
            a_prime(j,i)=1/(4*F_val/sigma(1,i)/C_t*sin(phi(j-1,i))*cos(phi(j-1,i))-1);

            phi(j,i)=atan((1-a(j,i))/lamda(1,i)/(1+a_prime(j,i)));
            alpha(j,i)=rad2deg(phi(j,i)-beta_val(1,i));
            [cl(j,i),cd(j,i)]=force(alpha(j,i));


            if i==elem
                %at tip F value set to previous element to avoid
                %divide zero error
                F_val=F(1,i-1);
            else
                factor_val=N/2*(1-r_rat)*sqrt(1+lamda_t^2); %Prandtl
                F_val=2/pi*acos(exp(-1*factor_val));
            end

            %convergence based on 'a' value
            if a(j-1,i)<0.0001
                %avoids divide zero error in percentage calculation
                per=0;
            else
                per=(a(j,i)-a(j-1,i))/a(j-1,i)*100;
            end

            if j>100 %to avoid excessive runtime from non-convergence
                converg=1;
                con_point(1,i)=j;
            else
                if per>0.1 | per<-0.1
                    converg=-1;
                else
                    converg=1;
                    con_point(1,i)=j;
                end
            end

            j=j+1; %increment iteration counter

            F(1,i)=F_val;

        end
    end

    %loop used calculate force for elements for a given TSR
    for i=1:elem
        r_rat=i/elem;
        width=1/elem; %width of element,ratio of R_t

        if r_rat>excl
            if (r_rat-excl)<width %smallest element
                width=r_rat-excl;
            end

            val=r_rat-width/2; %radius ratio at half way point of element

            c=chord(val); %chord at halfway point

            row_p=con_point(1,i-1);
            row=con_point(1,i);

            %calculate mid-point values for a, phi, cl and cd
            a_val=(1-(r_rat-val)/(1/elem))*(a(row,i)-a(row_p,i-1))+a(row_p,i-1);
            phi_val=(1-(r_rat-val)/(1/elem))*(phi(row,i)-phi(row_p,i-1))+phi(row_p,i-1);
            cl_val=(1-(r_rat-val)/(1/elem))*(cl(row,i)-cl(row_p,i-1))+cl(row_p,i-1);
            cd_val=(1-(r_rat-val)/(1/elem))*(cd(row,i)-cd(row_p,i-1))+cd(row_p,i-1);

            v_rel(m,i)=u_inf*(1-a_val)/sin(phi_val); %relative velocity

            re(m,i)=v_rel(m,i)*c*rho/1.8e-5; %reynold's number

            lift(m,i)=cl_val*0.5*rho*(v_rel(m,i))^2*c*width*R_t; %element lift
```

```
            drag(m,i)=cd_val*0.5*rho*(v_rel(m,i))^2*c*width*R_t; %element drag

            F_tan(m,i)=lift(m,i)*sin(phi_val)-drag(m,i)*cos(phi_val); %element tangential force

            F_n(m,i)=lift(m,i)*cos(phi_val)+drag(m,i)*sin(phi_val); %element normal force

            dT(m,i)=F_tan(m,i)*val*R_t; %element torque

            dP(m,i)=dT(m,i)*lamda_t*u_inf/R_t; %element power

            %total torque, power and thrust from one blade
            T=T+dT(m,i); % torque
            P=P+dP(m,i);% power
            Th=Th+F_n(m,i); % thrust

            %build data arrays for export
            phi_data(m,i)=phi_val;
            alpha_val(m,i)=alpha(row,i);
            a_val_data(m,i)=a_val;
            a_prime_data(m,i)=a_prime(row,i);
        end
    end

    %values at a given tip speed ratio multiplied by number of blades
    torque(1,m)=k;
    torque(2,m)=T*N;

    power(1,m)=k;
    power(2,m)=P*N;

    cpower(1,m)=k;
    cpower(2,m)=power(2,m)*2/rho/pi/R_t^2/u_inf^3;

    thrust(1,m)=k;
    thrust(2,m)=Th*N;

    m=m+1; %increase tsr counter
end

%matlab output for quick assessment of relevant data
[maxcp,index]=max(cpower(2,:));
N
u_inf
elem
maxcp_tsr=cpower(1,index)
maxcp
max_power=power(2,index)
max_torque=torque(2,index)
max_thrust=thrust(2,index)


%figure,plot(torque(1,:),torque(2,:)),xlabel('TSR'),ylabel('Torque (Nm)');
%figure,plot(power(1,:),power(2,:)),xlabel('TSR'),ylabel('Power (W)');
figure,plot(cpower(1,:),cpower(2,:)),xlabel('TSR'),ylabel('Cp');
%figure,plot(thrust(1,:),thrust(2,:)),xlabel('TSR'),ylabel('Thrust (N)');

%data file output
filecp=cpower';
filep=power';
fileT=torque';
fileTh=thrust';

topline=[maxcp_tsr,maxcp,max_power,max_torque,max_thrust]
fileov=[topline;filecp(:,1),filecp(:,2),filep(:,2),fileT(:,2),fileTh(:,2)];

filen=['data\bem_',int2str(N),'_',int2str(elem),'_',int2str(u_inf),'_loss.txt'];
dlmwrite(filen,fileov,'\t')
t=toc
```

Appendix B

Error Analysis

In all the error analysis presented in this section both bias and precision components of error are found. The bias component of error accounts for instrumentation errors which are usually specified by the manufacturer of a given device. The bias error is unique for each instrument and in some cases if the magnitude of the output affects the error each data point can have a specific bias error. Precision error on the other hand is calculated based on the statistical variance in the data and accounts for fluctuations in the instrument output but is constant for a sample population. The general calculation for the precision error used for this experiment is given below in equation B.1 with the standard deviation, t-value and the sample size required to determine this component of error. The t-value used in all error calculations for this experiment was based on the two-tailed Student's t distribution and assumes a 95% confidence interval. The total error for a given measurement is a combination of the bias and precision error and is found using equation B.2.

The methodology and equations used in this analysis are based on worked outlined by Moffat [47].

$$\Delta_{Prec} = \frac{t_S \sigma_S}{\sqrt{N_S}} \tag{B.1}$$

$$\Delta = \sqrt{\Delta_{Bias} + \Delta_{Prec}} \tag{B.2}$$

B.1 Velocity Error

The error in the velocity measurements can be broken into two components: the error of single point measurements and the error of the mean velocity. The bias error for both single measurement and the mean is calculated the same way as shown in equation B.3. The precision error can be calculated in two different ways with the single point measurement error accounting for the number of samples, as in equation B.4, and the mean velocity precision error found using equation B.5.

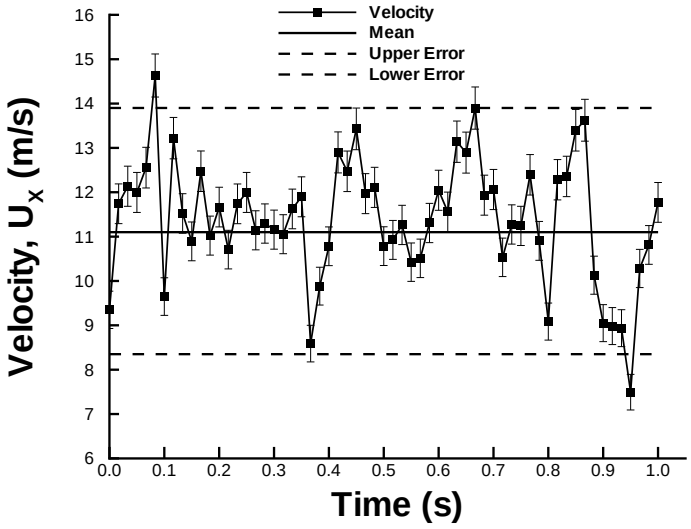

Figure B.1: Free stream velocity with both single measurement and mean error shown for comparison

$$\Delta U_{Bias} = 0.4 + 0.02 * reading \tag{B.3}$$

$$\Delta U_{Prec} = \frac{t_S \sigma_U}{\sqrt{N_S}} [single\, sample] \tag{B.4}$$

$$\Delta U_{Prec} = t_S \sigma_U \tag{B.5}$$

To represent the difference in the results of the two error calculations figure B.1 shows both single point measurement error and the upper and lower error bounds which represent the mean error. The upper and lower mean error bars should capture 95% of the data points around the mean based the assumed 95% confidence used when calculating the t-value. In other words, based on the selected confidence interval, 5% of the data should statistically lie outside of the upper and lower error bounds and for this particular data set only 3% of the data falls outside of the error bounds.

B.2 Error in power calculations

An error analysis of the power generated by the blades was conducted based on error associated with the data acquisition equipment. As the precision error equation is the same for all calculations only the development of the bias error component will be given in the error analysis below. The error propagation method was used in

Table B.1: Accuracy error in the Keithley 2700 multimeter [42]

$Range$ (V)	$Resolution$ (μV)	$Error_{Read}$ (ppm)	$Error_{Range}$ (ppm)	$Coef_{Read}$ $(ppm/^oC)$	$Coef_{Range}$ $(ppm/^oC)$
0.1	0.1	30	35	1	5
1.0	1.0	30	7	1	1
10.0	10.0	30	5	1	1
100.0	100.0	45	9	5	1
1000.0	1000.0	50	9	5	1

order to perform the analysis based on multiple parameters. The first step was to determine the error in the power calculated at the load bank and the generator input. Both of these powers were based on voltage and current measured at their respective points in the electrical system. The bias error calculation for power was derived using equations B.6 and .B.7.

$$\Delta P = \sqrt{\left[\left(\Delta V \frac{\partial P}{\partial V}\right)^2 + \left(\Delta I \frac{\partial P}{\partial I}\right)^2\right]} \tag{B.6}$$

$$\Delta P = \sqrt{(I * \Delta V)^2 + (V * \Delta I)^2} \tag{B.7}$$

These equations required the error in the current and error in the voltage to be found. All of the voltages applicable to the power measurement were made using the Keithley 2700 multimeter with a 7706 card installed. Based on the published error from the manual [42] a table, B.1, was prepared outlining the accuracy error at various range settings for a device which has been calibrated more than a year ago. The temperature coefficients applied to data collected at temperatures less than 18^oC and are multiplied by the difference in the ambient temperature and 18^oC. Additionally, the linearity error was published as 2 ppm of the reading and 1 ppm of the range setting.

With the error in the voltage known as a function of the range and reading given by the Keithley 2700 the current error could then be found. Since the current was actually a voltage measurement made across a shunt resistor it's error was also related to the Keithley voltage error as derived in equation B.8 to B.10. The gain found in equation B.8 was specific to each of the two shunt resistors, 1000 for the load bank and 600 for the generator shunt, but no error documentation could be found for the resistors. Therefore the error associated with the gain was assumed to be zero.

$$I_S = GV_S \tag{B.8}$$

$$\Delta I = \sqrt{\left(\Delta G \frac{\delta I}{\delta G}\right)^2 + \left(\Delta V \frac{\delta I}{\delta V}\right)^2} \tag{B.9}$$

$$\Delta I = G \Delta V \tag{B.10}$$

The error in the power generation value could then be found as the sum of the errors from the load bank power and the generator input power as these two values were subtracted when first finding the generation power. The drivetrain power loss was found to be a function of the rotational speed, as given by equation B.11 and B.12, and therefore the drivetrain error was based on error in rotational speed and found using equations B.11 and B.12. The error in the rotational speed measurements, required to determine the power loss error, was solely due to the clock accuracy in the digital counter which was specified as 50 ppm of the reading.[43]

$$\Delta P_{Drive} = \sqrt{\left(\Delta \Omega \frac{\delta P_{Drive}}{\delta \Omega}\right)^2} \tag{B.11}$$

$$\Delta P_{Drive} = \sqrt{\left(\Delta \Omega \left(-0.0054 * \Omega - 2.1165\right)\right)^2} \tag{B.12}$$

The estimated power at the blades was derived from difference between the power measured during testing and the drivetrain power loss estimate so the overall error was found by summing the two error values, found in equation B.13.

$$\Delta P_{Blade} = \Delta P_{GEN} + \Delta P_{Drive} \tag{B.13}$$

Since the bias error was specific to each reading there was no set value to apply to all data points. But the error range for the blade power was typically on the order of 1 to 2% after outlier points are removed which can skew the precision error estimate.

B.3 Error in coefficient of power calculations

The error propagation calculations for the coefficient of power were derived from equation 2.11 and are outlined in equations B.14 to B.15.

$$\Delta C_P = \sqrt{\left(\Delta P_{Blade} \frac{\delta C_P}{\delta P_{Blade}}\right)^2 + \left(\Delta \rho \frac{\delta C_P}{\delta \rho}\right)^2 + \left(\Delta U \frac{\delta C_P}{\delta U}\right)^2 + \left(\Delta R_T \frac{\delta C_P}{\delta R_T}\right)^2} \tag{B.14}$$

$$\Delta C_P = \frac{2P_{Blade}}{\pi\rho U^3 R^2}\sqrt{\left(\frac{\Delta P_{Blade}}{P_{Blade}}\right)^2 + \left(\frac{\Delta\rho}{\rho}\right)^2 + \left(\frac{3\Delta U}{U}\right)^2 + \left(\frac{2\Delta R}{R}\right)^2} \tag{B.15}$$

The error in the blade power estimates is detailed above. While the error in the density calculation was determined using the equations B.16 through to B.17. The pressure data used in the density calculations were from the University of Waterloo weather station based on the average of the data collected during the testing hours.[48] This pressure data has a stated error of +/- 20 Pa. The temperature data was collected by a thermocouple found in the CSAT3 anemometer and was collected at the same frequency as the velocity data and has an error of +/- 0.4 ^oC.

$$\rho = \frac{P}{RT} \tag{B.16}$$

$$\Delta\rho = \sqrt{\left(\Delta P\frac{1}{RT}\right)^2 + \left(\Delta T\frac{P}{RT^2}\right)^2} \tag{B.17}$$

The error in the velocity data collected using the CSAT3 sonic anemometer was given in the device specifications as +/- 0.04 m/s with a gain error of +/- 2% of the reading. The blade radius error was taken as half the smallest increment on the tape measure used and was therefore +/- 0.5 mm.

The resulting error in the coefficient of power was specific to each data point but was representative error values were typically around 7% of the calculated value.

Appendix C

Installation and Decommissioning of the Wind Turbine

The installation of the nacelle and tower was a multi-stage process with decommissioning being completed in the reverse order. The tower was initially assembled in a horizontal position with both sets of axial legs and one set of lateral legs bolted onto the base of the tower poles. The tower was then raised so that the tower poles were in a vertical position and the final set of lateral legs were bolted to the structure. The tower base was then moved to the final position in the wind facility and bolted to the ground using concrete mounts. The axial thrust bracing was then installed to stiffen the structure. Torque bracing must be installed after the nacelle is mounted to the towers as the guy wires interfered with the material lift used to raise the nacelle.

In order to install the nacelle onto the tower a mechanical material lift was utilized as the final height of the mounting point was approximately 3 m from ground level and the nacelle weighed approximately 230 kg. After the lift was completed the nacelle was fixed to the tower by eight bolts on matching mounting plates. The manually operated material lift raising the nacelle to the mounting point is shown in figures C.1 and C.2.

The three turbine blades were then mounted to the low speed shaft on the nacelle. All three blades were mounted to the adapter plate, which interfaces with the plate welded to the low speed shaft, while on level ground. Then using the material lift all three blades are lifted into position on the low speed shaft. This method was used as it was difficult to achieve the correct blade alignment when mounting the blades individually while at the 3.5 m shaft height. Overall the installation process, when completed efficiently and with an adequate number of people, can be completed in approximately two to three hours.

Figure C.1: Raising of the nacelle to the mounting point on top of the tower (Side view)

Figure C.2: Raising of the nacelle to the mounting point on top of the tower (Front view)

Appendix D

Turbine Blade Fabrication

The turbine blade fabrication process was completed using the technique outlined in the following sections.

D.1 Mould and Material Preparation

The mould, shown in figure D.1, was a two piece structure with three locating pins for joining the two sides. The two mould halves were not identical as one was much deeper at the root section and will be referred to as the "bottom half" with the shallow side being the "top half". Before each blade was manufactured the two sided mould was prepared for the moulding process by ensuring the mould was free of debris and applying a high temperature mould release wax to the inner surfaces.

Based on the lamination schedule, produced by Composotech [30], various types of fibreglass were cut and prepared for all three blades. Each blade required seven different layers of fibreglass with three different materials used. For each blade mould half the following material was cut: a skin layer, three structural layers, three spar support layers and one spar cover layer. An overview of the blade and the positions used in the placement of the layers is shown in figure D.2.

The skin layer, while providing some structure, is primarily to form the aerodynamic shape of the blade. It was comprised of 300 g/m^2 chopped strand mat (csm) fibreglass 30.5 cm wide and 226 cm long. The three structural layers were made using a 600 g/m^2 triax material which has strands in the chordwise direction and at +/- 45 degrees to the chord. This layer provides shear and torsional strength to the blades. All three structural layers of triax were 20.3 cm wide prior to trimming and had varying lengths which went to positions one, three and five, from figure D.2. The spar support layers are made of a UD (uni-directional) strand material with fibres running span-wise along the blade. These layers provide strength against the bending moment from thrust loading. The three layers of UD were cut to be 6.4 cm wide and went to positions two, four and six. Finally the spar cover layer was made from triax 20.3 cm wide prior to trimming and went to position one.

Figure D.1: Two piece mould prior to material lay-up, bottom half is on the right

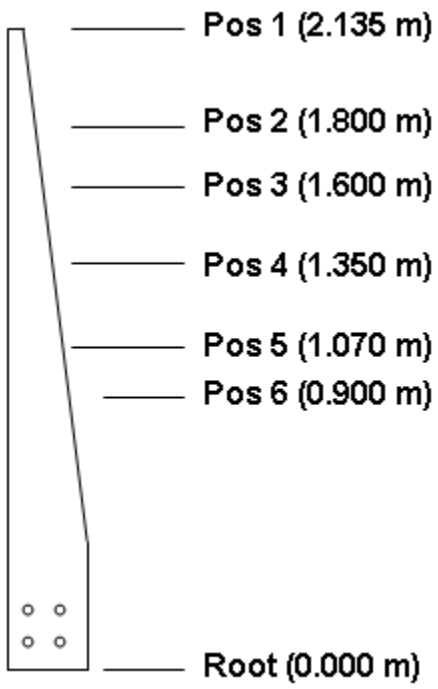

Figure D.2: Lamination schedule drawing with key positions labeled

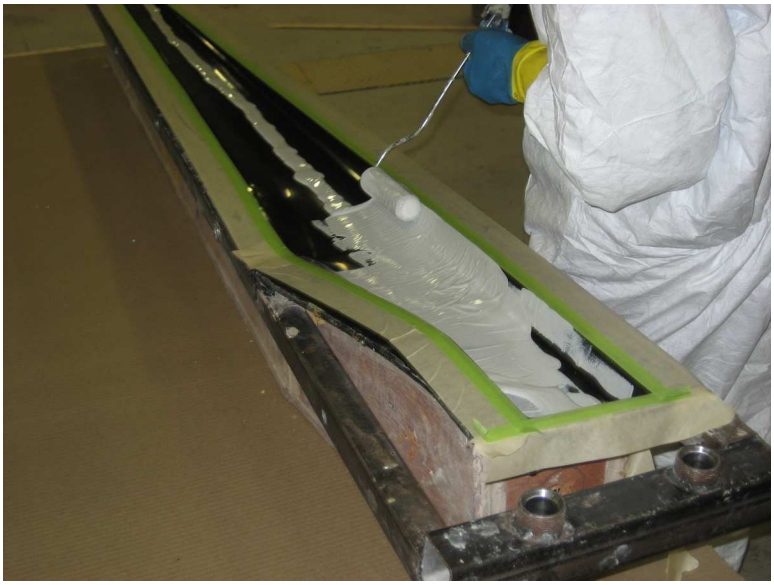

Figure D.3: Gel coat being applied to the lower mould

D.2 Process

With all of the fibreglass cut the following process was completed to prepare the mould surface and to apply the fibreglass layers.

The first step was to apply a gel coat to the waxed moulds, shown in figure D.3, using a small roller and hand brush. This application was done in the mould instead of spraying after the moulding process to ensure a smooth outer surface. This gel coat was allowed to cure for one hour before lamination of the fibreglass.

With the gel coat partially cured a resin, comprised of polyester orthophthalic resin [49] mixed with a catalyst, 2% by mass, was brushed onto the mould ensuring that all areas of the mould were wet. The composition of the resin and the ratio of the catalyst added was specified in the lamination schedule as provided by Composotech [30] and will change depending on the desired strength of the blades and materials used. In order to fill areas of the mould with a tight radius, as indicated in figure D.4, a putty was prepared and applied to those areas. This putty consisted of the resin-catalyst mixture with 32 mm milled fibreglass and fumed silica [50], a product which can increase the viscosity of the mixture. The putty was used to avoid introducing voids into the finished blade structure in areas where the fibreglass material could not match the curvature of the mould.

The general process for applying fibreglass layers was the same throughout the blade making process with any specific instructions in the lamination schedule outlined in section D.3. First the appropriate layer was positioned above the mould and laid in place and gently patted down by hand. Each layer was applied dry to the existing layer as the existing layer was typically still wet. With the mat in place a measured amount of the resin was applied to the layers using a brush until the

Figure D.4: Areas of the mould which required putty to fill small radius areas

mat was saturated. The level of saturation in the fibreglass will affect the colour it has and an experienced worker can apply the correct amount of resin based on this colour. Visible bubbles in the fibreglass were then removed using a metal roller which allows the resin to be evenly distributed along the blade. If required a small brush with resin on it or a flexible putty blade can be used to remove any remaining bubbles. Some bubbles under the fibreglass layers at the edges of the mould were not required to be removed as they were outside of the finished blade area as shown in figure D.5. Care was taken throughout this process to monitor how much resin was being used to avoid a "resin rich" or "fibre rich" blade. If too much resin is used the blade can become brittle whereas too little resin could make the blade weak and in the extreme will result in delamination. The desired fibreglass to resin ratio, by mass, for this blade was 50/50 by Composotech design [30].

D.3 Fibreglass Lamination Schedule

The lamination schedule prepared by Compostech is outlined below with details of each layer's application and the techniques used during the process. A cutaway of the final structure can be found in figure D.6, with the solid line representing the skin layer, the dashes representing triax, dots with a line representing UD and the hatched area representing the foam core.

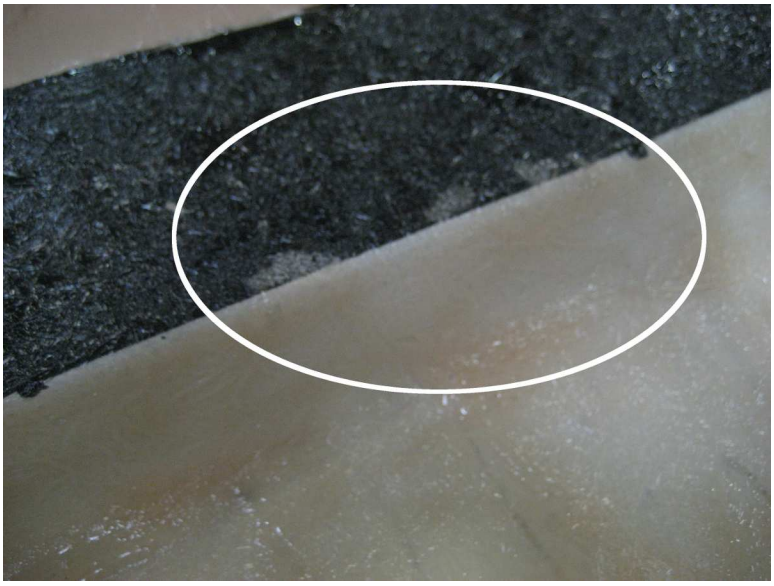

Figure D.5: Bubbles under the skin layer at the edge of the blade mould cavity

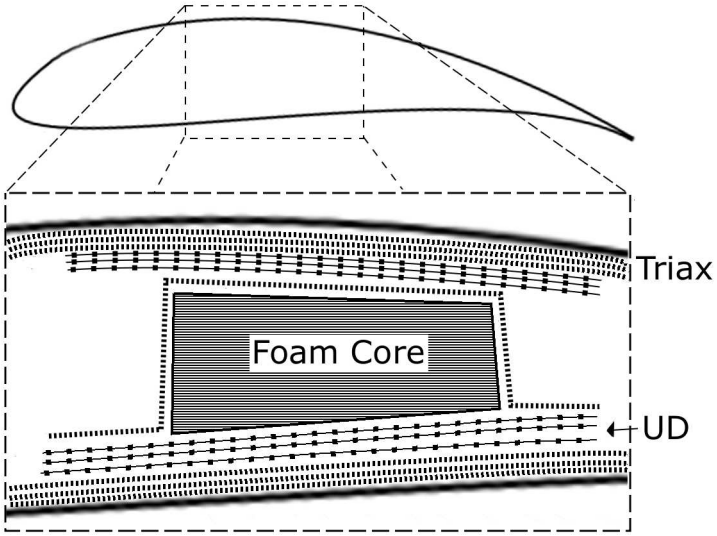

Figure D.6: Cutaway view of the blade structure

Figure D.7: Skin layer cuts made to avoid wrinkles in bottom half of the mould

D.4 Skin Layer

The 300 csm skin layer was the first layer of fibreglass applied to the mould and as such the mould was coating in resin prior to it's application. Excess material was cut from around the edge of the mould plates which left an area on each side of the blade cavity covered. Cuts are made to the skin layer on the bottom half perpendicular to the mould edge to avoid wrinkles in the surface, shown in figure D.7. The skin layer was allowed to cure for one hour prior to further application of fibreglass.

D.4.1 Second Lamination - triax

The second layer of fibreglass was a triax layer applied directly to the skin layer using the longest of the triax mats. It was applied with one of the edges of the mat aligned with the leading edge of the blade cavity in the mould. The trailing edge of the mat was then trimmed to be 1 cm from the mould edge at the tip, as shown in figure D.8, and approximately 2 cm at the root. This is done to achieve a sharp trailing edge at the end of the process. Alternatively, the trailing edge can be sanded down to achieve the desired thickness.

D.4.2 Third and Fourth Lamination - triax

Both the third and fourth laminations were applied while the previous layer was still wet with each layer becoming progressively shorter with excess resin removed or redistributed. The moulds with the fibreglass layers to this point can be seen

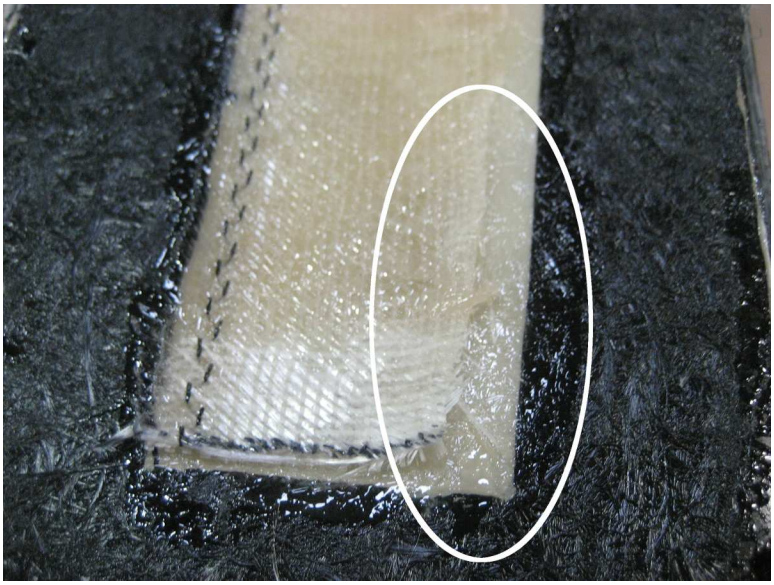

Figure D.8: Triax trimmed to be 1 cm from the mould edge at the tip

in figure D.9. The end of each triax layer can be seen in this figure as a dark line chordwise along the blade.

D.4.3 Fifth to Seventh Lamination - UD

The fifth to seventh laminations were comprised of the UD fibreglass and became progressively shorter. The layers were applied flush with the end of the root cavity which, for the longest mat, placed it approximately 30 cm from the tip. This was because there was physically no room for additional material thickness in the tip of the blade. The UD was placed along the centreline of the mould cavity with care to ensure that the relative placement on the top and bottom halves were the same. As before all layers were applied with the previous layer still wet. Figure D.10 shows the UD layer being applied to the moulds.

D.4.4 Texture mat

Prior to the installation of the spar a textured mat, called peel ply [51], was applied to the entire blade surface while the layers were still wet. This mat, made of nylon, imparts a three dimensional texture to the surface as it cured which allowed the subsequent spar layer to bond with greater strength. It was applied in strips along the trailing edge of the mould from tip to root and then back along the leading edge from root to tip until the entire surface was covered. Resin was then applied to the top to flatten it to the previous layers, as shown in figure D.11. Once this resin was dried sufficiently, after approximately one hour, the mat was removed giving the surface the desired texture.

Figure D.9: Mould with the fourth lamination applied

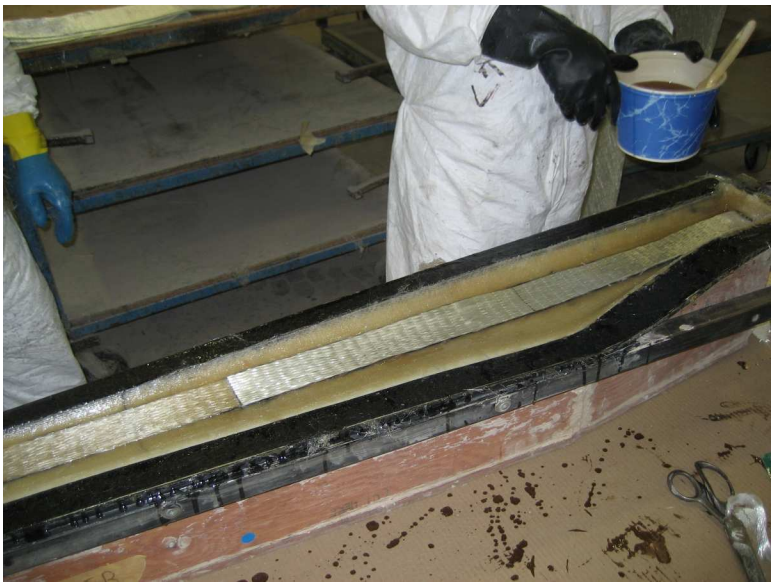

Figure D.10: UD layer application

Figure D.11: Textured mat application

D.5 Spar

The final component of the blades to be made was the spar. This spar provided a core to the blade and helped to connect the top and the bottom halves. Structurally the spar was similar to the web of an I-beam with the final three layers of UD on each blade acting as the flanges. The spar consisted of a foam core with triax 600 g/m^2 fibreglass laid on top. The first step to making the core section was to measure the depth of the mould halves at regular intervals from root to tip. The depths were added together to determine the required thickness of foam to contact the two halves when they were mated with 4 mm subtracted from this value to compensate for the thickness of the final triax layer applied to the foam core. Each blades core was hand cut based on depth measurements of the mould halves which resulted in a wedge shaped foam block. The spar block was then placed in the bottom of the mould and the final triax layer was wrapped over it with a similar technique as previous layers. Excess triax material was trimmed from the sides of the spar while maintaining a minimum of 25 mm on each side of the foam block.

D.6 Mating Moulds

The first step of the mating process is to determine the gaps in between the mould halves. The spar was first positioned in the bottom mould dry. With the spar in place plasticine balls were placed along the top of the spar and around the perimeter of the trailing and leading edges. The two mould halves were then compressed together and then released. The thickness of the plasticine after being compressed will then represent the gap between the two moulds. Ideally this gap is 2 mm which

allows for sufficient putty to remain in the joint to bond the halves.

The perimeter of the mould, spar and spar contact areas on the top and bottom of the mould were then coated in resin to prime the surfaces. Putty was applied along the outside of the blade cavity and along the spar contact areas. The spar was then positioned in the bottom mould half and the two halves were joined and compressed. They were held together for approximately twelve hours and then separated. At this point any excess fibreglass, resin or irregularities were removed and repaired.

Appendix E

PIV Smoke Injection Methods

In order to aid future PIV work which may be completed using this facility an attempt to catalogue some of the failed smoke injection methods for PIV are outlined in this section.

A failed attempt is depicted in figure E.1. The failed method shown placed the smoke generator in the flow straightening section of the tunnel. This particular method was unsuccessful because the smoke generator was too far upstream from the turbine which resulted the smoke stream becoming too diffuse giving a low seeding particle density. In figure E.1 the smoke is shown to cover at least half of the blade at the rotor plane.

The second method shown in figure E.2 placed the smoke generator approximately 2 m upstream of the rotor plane with the smoke traveling through a 1 cm plastic tube into a straightening manifold. This method also resulting in the smoke being too diffuse while also having an excessive amount of condensate buildup which blocked the flow of smoke within the tube.

Figure E.1: Failed smoke method with smoke generator placed on the conditioning grid

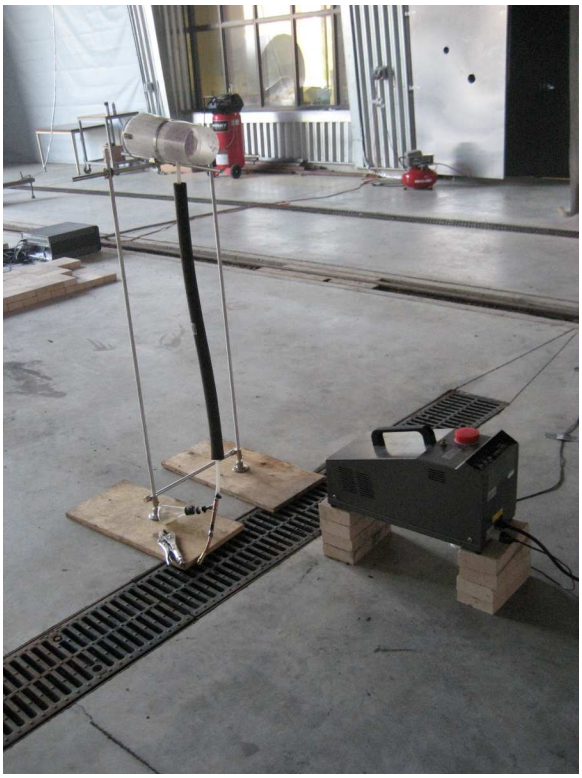

Figure E.2: Failed smoke method using a manifold with flow straightening tubes to aid in mixing and smoke stream quality

Appendix F

Post Processing Code

The post processing code used for the PIV analysis was comprised of two main components: image shift determination, PIV data shift and shifted image output.

F.1 Image Shift Determination

The following code is used to determine the number of pixels that each image was shifted from a master image. These x and y shift values were then used to shift the PIV results calculated from the Flow Manager software [40].

```
function output=shift(start,num,filen)
shift_data=zeros(1);

j=start; %first image
thres=100; %outlier threshold

imA='master_A.tif';
for i=1:num
    imB0='e:\Test_1_export\';
    if j<10
        imB1='second_1_.1qqao5n5.00000';
    elseif j>=10 & j<100
        imB1='second_1_.1qqao5n5.0000';
    elseif j>=100 & j<1000
        imB1='second_1_.1qqao5n5.000';
    else
        imB1='second_1_.1qqao5n5.00';
    end

    imB2=int2str(j);
    imB3='.tif';
    imB=[imB0,imB1,imB2,imB3];

    A=imread(imA);
    B=imread(imB);

    R = real(ifft2(fft2(B).* conj(fft2(A))));
    F=fftshift(R);

    [maxval_F1,I_F1] = max(F);
    [maxval_F2,I_F2] = max(maxval_F1);

    Xpos=I_F2;
    Ypos=I_F1(1,I_F2);

    %Shifting plot axes to correspond to correlation plot
    [X,Y]=meshgrid(-504:503,-509:508);

    xshift=X(1,Xpos);
    yshift=Y(Ypos,1)*-1;

    xint=round(xshift/16);
    yint=round(yshift/16);
```

```
        shift_data(i,1)=j;
        shift_data(i,2)=xshift;
        shift_data(i,3)=yshift;
        shift_data(i,4)=xint;
        shift_data(i,5)=yint;
        j=j+1

        filen1=['raw_',filen];
        %dlmwrite(filen1,shift_data)
end

%removing outliers Chauvenet's criterion
mu_x=mean(shift_data(:,2));
sigma_x=std(shift_data(:,2));
mu_y=mean(shift_data(:,3));
sigma_y=std(shift_data(:,2));
value=norminv(1-1/4/num);

k=1; %good data index
for i=1:num
        xshift=shift_data(i,2);
        yshift=shift_data(i,3);

        x_crit=abs(xshift-mu_x)/sigma_x;
        y_crit=abs(yshift-mu_y)/sigma_y;

        if x_crit>value | y_crit>value | abs(xshift)>thres | abs(yshift)>thres
                shift_data(i,6)=1;
        else
                good_data(k,:)=shift_data(i,1:5);
                shift_data(i,6)=0;
                k=k+1;
        end
end

dlmwrite(filen1,shift_data)

filen2=['shift_',filen];
dlmwrite(filen2,good_data)

output=good_data;
```

F.2 PIV results Shift

The following code uses the x and y shift values determined using the image shift determination code to shift the PIV results.

```
function piv_output=piv_shift(shift_data)

[r,c]=size(shift_data);

for i=1:r
        xshift=shift_data(i,2);
        yshift=shift_data(i,3);
        xint=shift_data(i,4);
        yint=shift_data(i,5);

        right_x=-1*min(shift_data(:,4));
        left_x=61-max(shift_data(:,4));
        low_y=-1*min(shift_data(:,5));
        high_y=61-max(shift_data(:,5));

        j=shift_data(i,1);  %set to image number start

        in0='e:\Test_1_export\Correlation\';
        if j<10
                in1='second_1_.1qqkqy79.00000';
        elseif j>=10 & j<100
                in1='second_1_.1qqkqy79.0000';
        elseif j>=100 & j<1000
                in1='second_1_.1qqkqy79.000';
        else
                in1='second_1_.1qqkqy79.00';
        end

        in2=int2str(j);
        in3='.txt';
        in=[in0,in1,in2,in3];

        cor_data=dlmread(in,'\t',5,0);

        [row_data,col_data]=size(cor_data);
```

```
    k=1;

    for m=1:row_data
        x_num=cor_data(m,1)-xint;
        y_num=cor_data(m,2)-yint;

        if x_num>=right_x & x_num<=left_x & y_num>=low_y & y_num<=high_y
            new_cor_data(k,1)=x_num;
            new_cor_data(k,2)=y_num;
            new_cor_data(k,3)=cor_data(m,10);
            new_cor_data(k,4)=cor_data(m,11);
            new_cor_data(k,5)=cor_data(m,3)-xshift;
            new_cor_data(k,6)=cor_data(m,4)-yshift;
            new_cor_data(k,7)=cor_data(m,12);

            k=k+1;
        end
    end

    out1='cor_shift\second_1_';
    out=[out1,in2,in3];

    %dlmwrite(out,new_cor_data,'\t');

    piv_output(:,:,i)=new_cor_data;

    j=j+1;
    i
end
```

F.3 Image Shifting

For program verification and for the presentation of results a program was also written to crop and shift the images based on the x and y shift results.

```
shift_data=dlmread('shift_0_9.txt');

[r,c]=size(shift_data);

for i=1:r
    j=shift_data(i,1);

    imB0='test1\';
    if j<10
        imB1='second_1_.1qqao5n5.00000';
    elseif j>=10 & j<100
        imB1='second_1_.1qqao5n5.0000';
    elseif j>=100 & j<1000
        imB1='second_1_.1qqao5n5.000';
    else
        imB1='second_1_.1qqao5n5.00';
    end

    imB2=int2str(j);
    imB3='.tif';
    imB=[imB0,imB1,imB2,imB3];

    A=imread(imB);
    %figure; imshow(A);

    xshift=shift_data(i,2);
    yshift=shift_data(i,3);

    for k=1:1018
        for m=1:1008
            if (k-yshift)>0 & (m+xshift)>0 & (k-yshift)<=1018 & (m+xshift)<=1008
                new_A(k,m)=A(k-yshift,m+xshift);
            else
                new_A(k,m)=0;
            end
        end
    end
    %figure; imshow(new_A);

    filen=['imshift\shifted_',int2str(j),'.tif']
    imwrite(new_A,filen)
end
```